Determination of nanomechanical properties of surfaces by atomic force microscopy using higher harmonics

Federico Gramazio

Universitat Autònoma de Barcelona

POSTGRADUATE SCHOOL
PHYSICS DEPARTMENT

Ph. D. THESIS

Determination of nanomechanical properties of surfaces by atomic force microscopy using higher harmonics

Thesis submitted by
Federico Gramazio

to apply for the Degree of DOCTOR at the
Universitat Autonòma of Barcelona
in the PHYSICS PROGRAM

Thesis Advisor: **Dr. Jordi Fraxedas**
Thesis co-Advisor: **Prof. Francesc Pérez - Murano**
Thesis Tutor: **Prof. Javier Rodríguez - Viejo**

prepared at Institut Català de Nanociència i Nanotecnología (ICN2)

defended on:
March 2018

ICN2
EXCELENCIA
SEVERO
OCHOA
Institut Català
de Nanociència
i Nanotecnologia

UAB
Universitat Autònoma
de Barcelona

Bellaterra, 15 December de 2017

Dr. Jordi Fraxedas, CSIC research scientist, member of the group of **Force probe microscopy & Surface nanoengineering** in the **Institut Català de Nanociència i Nanotecnologia (ICN2)** and Prof. Francesc Pérez Murano, CSIC research professor, member of the group of **NEMS and Nanofabrication group** en el **Instituto de Microelectrónica de Barcelona (IMB-CNM CSIC)**, as thesis directors and Prof. Javier Rodríguez - Viejo, Full professor at the **Universitat Autònoma de Barcelona**, as thesis tutor.

CERITFY:

That Federico Gramazio, Master in physics, has done under their direction the work entitled ***"Determination of nanomechanical properties of surfaces by atomic force microscopy using higher harmonics"***. This work has been developed within the doctoral program of Physics and constitutes his doctoral thesis memory, to opt for the degree of Doctor by the Universitat Autònoma de Barcelona.

Dr. Jordi Fraxedas Prof. Francesc Pèrez Murano

Prof. Javier Rodríguez Viejo

Abstract

This doctoral thesis entitled "Determination of nano-mechanical properties of surfaces by atomic force microscopy using higher harmonics" addresses the problems related to the determination of mechanical properties of materials at the nanoscale. As present, technology challenges are more and more related to miniaturized devices and it exists a strong interest in the development of accurate, non destructive methods to characterize the mechanical response of material with nano-metric accuracy.

Surface science and material science in general have received great impulse thanks to the introduction of novels standard characterization techniques based on scanning probe microscopy. Among those, in the last years, dynamic AFM methods based on multi-frequency and multi-harmonics approach have raised a great interest even if there is not yet a deep comprehension of the information brought by this kind of signals.

The aim of the thesis is indeed to give an insight to this new family of characterization techniques and present new perspectives regarding the use of higher harmonics in standard AFM imaging.

Firstly, a short overview of the main theoretical aspects of probe-surface interactions is presented along a description of the main models of relevant contact mechanics, in order to contextualize and understand the effects that can influence this kind of study and its experimental and simulation results.

The following part is dedicated to an exhaustive outlook of the state of the art of experimental methods used to determine mechanical properties at micro/nano scale, including indentation based methods and AFM based methods. This overview has the aim of giving a general idea of what the panorama offers about the nano-mechanical characterization, what are the actual strengths and limits.

The core of the thesis consists of the presentation of the experimental methods and achievements regarding the development of a novel AFM characterization method, based on the monitoring of higher harmonics amplitude during amplitude modulation scan.

It has been possible to study systematically the influence of common working parameters on the intensity of resonant higher harmonics, combining theoretical simulation with experimental studies. This part is especially addressed by the article: "Functional dependence of resonant harmonics on nano-mechanical

parameters in dynamic mode atomic force microscopy".

In the latter part of the thesis the attention has been placed, taking advantage of the previous part, on the determination of the best conditions for the maximization of the 6^{th} higher harmonic amplitude and on the development of a method based that could be employed in order to quantify the elastic response (i.e. Young's modulus) of a wide range of materials. The article "Quantification of nanomechanical properties of surfaces by higher harmonic monitoring in amplitude modulated AFM imaging" report the details of this method.

Resumen

Esta tesis doctoral titulada "Determinación de las propiedades nanomecánicas de las superficies mediante microscopía de fuerza atómica utilizando armónicos superiores" trata de los problemas relacionados con la determinación de las propiedades mecánicas de los materiales a escala nanométrica. Hoy en día, los desafíos tecnológicos están cada vez más relacionados con dispositivos miniaturizados y existe un gran interés en el desarrollo de métodos precisos y no destructivos para caracterizar la respuesta mecánica del material con precisión nano-métrica.

La ciencia de la superficie y la ciencia de los materiales han recibido en general un gran impulso gracias a la introducción de técnicas de caracterización estandár y originales basadas en microscopía con sonda de barrido. Entre ellas, en los últimos años, los métodos dinámicos de AFM basados en el enfoque multi-frequencia y multi-armónicos han despertado un gran interés, incluso si todavía no se tiene una comprensión profunda de la información generada por este tipo de señales.

El objetivo de la tesis es dar una idea de esta nueva familia de técnicas de caracterización y presentar nuevas perspectivas con respecto al uso de armónicos superiores en imágenes de AFM estándar.

En primer lugar, se presenta una breve descripción de los principales aspectos teóricos de las interacciones sonda-superficie a lo largo de una descripción de los principales modelos de mecánica de contacto relevante, para contextualizar y comprender los efectos que pueden influir en este tipo de estudio y sus resultados experimentales y de simulación .

La siguiente parte está dedicada a una perspectiva exhaustiva del estado del arte de los métodos experimentales utilizados para determinar las propiedades mecánicas a escala micro/nano, incluidos los métodos basados en indentaciones y los métodos basados en AFM. Esta visión general tiene el objetivo de dar una idea de lo que ofrece el panorama sobre la caracterizacíon nanomecánica, cuáles son las fortalezas y los límites reales.

El núcleo de la tesis consiste en la presentación de los métodos experimentales y los logros con respecto al desarrollo de un nuevo método de caracterización de AFM, basado en la monitorización de la amplitud de armónicos superiores durante la exploración de modulación de amplitud.

Ha sido posible estudiar sistemáticamente la influencia de los parámetros de trabajo comunes en la intensidad de los armónicos superiores resonantes, combinando la simulación teórica con los estudios experimentales. Esta parte se aborda especialmente en el artículo: "Dependencia funcional de armónicos resonantes en parámetros nano-mecánicos en el modo dinámico de microscopía de fuerza atómica".

En la última parte de la tesis se ha puesto la atención, aprovechando la parte previa, en la determinación de las mejores condiciones para la maximización de la amplitud armónica de 6^{th} y en el desarrollo de un método basado en que podría emplearse para cuantificar la respuesta elástica (es decir, el módulo de Young) de una amplia gama de materiales. El artículo "Cuantificación de las propiedades nanomecánicas de las superficies mediante una monitorización armónica más alta en imágenes de AFM moduladas en amplitud" informa sobre los detalles de este método.

Contents

Introduction 1

1 Probe-Surface interactions 5

1.1 Surface forces 5

1.1.1 Van der Waals forces 7

1.1.2 Electrostatic forces 13

1.1.3 Capillary forces 14

1.1.4 Solvation forces 16

1.1.5 Adhesion 18

1.2 Contact mechanics and mechanical models 19

1.2.1 Hertz model 22

1.2.2 DMT model 23

1.2.3 JKR model 25

1.2.4 Maugis' model 26

1.2.5 Viscoelasticity 28

2 Experimental methods for mechanical characterization 31

2.1 Non AFM methods 32

2.1.1 Indentation method 32

2.1.2 Nanoindenter-based modulus mapping 33

2.2 AFM methods 36

2.2.1 Quasi-static measurements of mechanical properties by AFM 39

2.2.2 Dynamic measurements of mechanical properties by AFM . . 41

2.2.3 Calibration methods 48

3 Experimental and Simulation Methods 55

3.1 Experimental Section 55

3.2 Computer Simulations: Virtual Environment for Dynamic AFM . . . 57

4 Functional dependence of resonant harmonics on nano-mechanical parameters in dynamic mode atomic force microscopy 63

4.1 Abstract 63

4.2 Introduction 64

4.3 Results and Discussion 65
    4.3.1 Simulations 65
    4.3.2 Experiments 69
4.4 Conclusion 74
    4.4.1 Simulations and Experimental Details 74
4.5 Acknowledgements 75
4.6 Supporting Information 75

5 Quantification of nanomechanical properties of surfaces by higher harmonic monitoring in amplitude modulated AFM imaging 79
5.1 Abstract 79
5.2 Introduction 80
5.3 Materials and Methods 81
    5.3.1 Simulations 81
    5.3.2 Experimental 81
    5.3.3 Self-assembled Block Copolymers samples 82
5.4 Results and Discussion 83
    5.4.1 PS - LDPE 85
    5.4.2 PS-b-PMMA 86
    5.4.3 PS-b-PMMA with modified PMMA by SIS 87
5.5 Conclusions 88
5.6 Acknowledgements 89

6 Conclusions 91

Bibliography 113

Appendix A Continuous monitoring of tip radius during AFM imaging 117

Appendix B List of publications 125

Introduction

The determination of mechanical properties at the nano-scale is an intensive topic of study in several fields of nano-physics, from surface and material science to biology. It plays also a critical role in the overall performance of nano and micro systems of applicative importance such as polymer blends and coatings, regard their wear and corrosion protection, but also in biological functions such as tissue growth or bacterial adhesion. Quantitative measurements of soft materials systems such as these, can be challenging due to the delicate nature of the sample, its complex topography and heterogeneous distribution of mechanical properties.

Most of the common technique employed for mechanical characterization, such as tensile testing, bending tests of dynamical mechanical analysis are more sensitive to bulk mechanical properties than to the surface ones, can be destructive for the samples and performing a high resolution surface map at nano-scale could be not straightforward. Moreover many kind of soft and bio-samples need characterizations in controlled environment and/or in liquid. Among the several characterization techniques, atomic force microscopy (AFM) is one that allow excellent force sensitivity, imaging and nanomechanical characterization of materials with moduli in the range of kPa and GPa, in a non destructive or minimally destructive locally way. It permits to map mechanical properties with nano-scale resolution, also in situ and controlled environment. In the last years, the necessity to improve the sensitivity to the mechanical properties and join it to other AFM-based techniques of characterization, led to the emergence of the multi-frequency techniques. Among the multi-frequency AFM techniques, there is one called Harmonic atomic force microscopy and based on the amplitude modulation one (AM-AFM) in repulsive mode. When the tip interacts with the sample surface, harmonic signal components are induced to the cantilever motion due to the non-linear character of the interaction. These components and the force acting on the cantilever can be expressed in terms of Fourier series. Although the higher harmonic amplitudes are well below 1nm, such amplitudes can be monitored with a reasonable signal-to-noise ration when they are amplified by a flexural eigenmode. For this reason, in this Thesis we chose to detect the 6^{th} higher harmonic oscillation amplitude because its close proximity with the 2^{nd} flexural eigenmode.

In a first time, we chose to observe and take advantage of the dependency of the 6^{th} higher harmonic amplitude to the tip radius of the cantilever in order to study a possible continuous monitoring of tip radius method during an AM-AFM imaging scan in repulsive mode. In fact, the irreversible deterioration of cantilever tip and of the surfaces under characterization during AFM operation is a concern as old as AFM itself. Several strategies have been undertaken since its discovery, in order to monitor the physical condition of the tip. The AM-AFM operation mode was implemented with the aim to strongly reduce tip wear through intermittent contact, eliminating shear stresses due to sliding. However, such reduction is not complete because of the high frequency oscillations involved, within the few hundreds of kHz. Thus, tip wear can still be a drawback even in the less invasive AM-AFM mode. This is an important issue not only for the routinely characterization of surfaces but also for tip-based manufacturing technologies and metrology involving AM-AFM operation since wear must be avoided to provide viable processes.

Despite the theoretical effort made in the last year to describe and understand the potential use of higher harmonics, it missed a description of their functional dependence on relevant parameters such as cantilever force constant (k_c), tip radius (R), free oscillation amplitudes (A_0), and sample Young modulus (E). For that, the second part of this study was characterize the dependence of 6^{th} higher harmonic oscillation amplitude on the experimental parameters cited above. This has been done comparing experimental values obtained by imaging, varying every time one of the experimental parameters, with the results obtained by simulations performed with the Virtual Environment for Dynamic AFM (VEDA) software. This second part of the project allowed to find the best conditions (drive amplitude of the cantilever, working amplitude set point, sample's Young modulus) in order to enhance the 6^{th} higher harmonic oscillation amplitude and be enough sensitive to the variation of Young modulus value and pass from a qualitative description to a quantification of this mechanical property of the surface. This work of quantification was performed on block copolymers sample (BCP) composed by polymers with different values of Young modulus and difference between the different phases getting smaller and smaller in order to understand also what is the minimum sensitivity achievable with this kind of technique. In order to obtain the quantification, the experimental results were compared with a set of simulation performed with the experimental parameters of the scan and of the cantilever employed. BCPs samples have been chosen because their Young's modulus values are in the range where the changes in value are more appreciable. Moreover, BCPs samples are becoming more and more employed in many applicative fields: for example, such as in micro and nano-electronics as new patterning mask, medical engineering as scaffolding tissue or heart valves, smart sensors and e-textile technologies or also energy storage. In the specific, polymeric thin films, such as ours samples, are becoming one of the more employed components in the already mentioned fields. For such applications, the characterization of their nano-mechanical properties is really important because these properties may show dramatic changes between bulk and thin film state.

The research reported in this thesis concerns the overall objectives of the study, consisting in the three steps introduced above, reporting the publications obtained from each phase and examining in deeper the part that in the articles were not extendedly exposed due to space limitations. The outline of the thesis is divided in six chapters where the main theoretical notions and experimental methods about the characterization of the mechanical properties are introduced, followed by the description of this specific work of thesis.

The Chapter 1 aims to give a general overview about the tip-sample kind of interactions and introduce the four main mechanical models, giving more attention to the Derjaguin, Muller, Toporov (DMT) model because the one used in the simulations and also adopted for other techniques with which the results were compared.

The Chapter 2 introduces the main techniques employed in the mechanical properties characterization, giving more importance to the ones based on the atomic force microscopy and distinguishing them between static and dynamic techniques. In this kind of study, the calibration of the cantilever and other parts of the AFM is critical. Therefore, the main calibration methods for the cantilever parameters will be presented too.

In Chapter 3, the experimental methods and set-up are explained along with the employed simulation software and the main mechanisms and models on which it is based. A specific attention was paid to the several parameters and their value used for our studies.

In Chapter 4, the results about the study of a continuous tip monitoring method during AFM imaging are presented. This method is based on the use of higher harmonics, which are generated in the repulsive regime as a result of the non-linear interactions between the cantilever tip and the surface under study.

In Chapter 5, a combined theoretical and experimental study of the dependence of resonant higher harmonics of rectangular cantilevers of an AFM as a function of relevant parameters are showed. The considered parameters are the most relevant in an AFM imaging experiment, such as cantilever force constant, tip radius and free oscillation amplitude as well as the stiffness of the sample's surface. From this kind of study, we obtained a good match between simulated trend and experimental one, even if just from a qualitative point of view.

In Chapter 6, the first work of quantification of Young's modulus by higher harmonic imaging is presented. The experimental value of 6^{th} higher harmonic amplitude on BCPs sample with different Young's modulus values were compared with the simulations results. The comparison gives Young's modulus values that agree with the results obtained on the same kind of samples with other techniques. The incertitude on this values is comparable too.

In Chapter 7, a resume of all the results obtained in this Thesis can be find along with possible future improvements.

Chapter 1

Probe-Surface interactions

1.1 Surface forces

The surface can be defined as the outside part or uppermost layer of objects. From a physical point of view, we could say that the interface is the transitional zone between the bulk of a medium and another medium, which can be another material, gas, liquid or vacuum. The properties and structure of the first layers of a material can be different from those of the bulk. Long and short range forces act making the molecules stick to the surface, stabilizing it, making gases condense to liquid, and liquids freeze to solids. Since ancient times, humankind has tried to figure out and model why and how these phenomena happen. As J. N. Israelachvili explains in his historical review [Israelachvili and Ruths, 2013], the earliest development of the concept of force arises among the ancient Egyptians around 1200 B.C. and relates the force to the deity. The first explanations not based on religion were proposed by the ancient Greeks, who observed how certain kinds of materials mysteriously interacted and influenced each other: what we now recognize as magnetic, electrostatic and gravitational interaction forces [Verschuur, 1993]. For the early philosophers, science went hand-in- hand with religion and philosophy and in the debate about the origins of interactions and also about the structure of matter and the space between interacting bodies, the structure of matter was closely connected with concept of force. Empedocles (ca. 490-450 B.C.) theorized that all matter in the universe was composed of four basic elements: earth, air, fire and water. These elements were combined with two cosmic principles: love or harmony and strife or disorder. He also introduced the idea that the sum of all the constituent of the universe was constant, a forerunner to the principle of conservation of energy. At the same time, Anaxagoras (ca. 500-428 B.C.) thought of a separate moving force external to matter as a sort of fluid, which was related to the mind and reason [Jammer, 1957]. Plato then interpreted Empedocles' harmony and disorder forces as attraction and repulsion, moving closer to the current interpretation, and Aristotle (ca. 384-322 B.C.) developed the concepts of forces, introducing two types: those inherent in matter and others emanating from substances that produce the effect of push and pull. Aristotle was working in the right direction but did not believe in atoms and voids or in the forms of mechanical interactions between atoms, that his atomist colleagues were proposing. Aristotle's way of thinking was so influential that his ideas formed the basis of physics and chemistry for the next two millennia while other lines of thoughts remained ignored. With Posidonius (ca. 135-51 B.C.) the concept of a force linking two bodies simultaneously started to spread. The theories of Aristotle and Posidonius were adopted by the Romans and became the basis of the explanation of nature for several centuries up to the beginning of the Middle Ages.

In that period of greek philosopher, magnetism was not understood but through the discovery of lodestone (a naturally magnetized magnetite), the effects were observed and looked on with superstition until the 19th century. Electromagnetism was also observed by rubbing some materials, such as amber, and attracting small objects (the electrostatic effect). Finally, awareness of a third force developed that was not easily reconciled with the other two phenomena: what we now recognize as gravitation. Archimedes (287-212 B.C.) discovered in his one "Eureka"; moment that the resultant force on a body , composed by the force of gravity and the still unknown Archimede's force, can change from attractive to repulsive, when placed in a medium that it displaces. Of course, such displacements also occur because of other forces such as Van der Waals and electric polarization, which were discovered almost two millennia later.

In this summary, we have arrived at the Middle Ages and the Renaissance but little progress was made during these periods: Roger Bacon (ca. 1220-1292) started to propose experiments in opposition to a just rhetorical and philosophical study; Leonardo da Vinci (1452-1519) was convinced of the truth of the notion of natural versus emanating forces [Jammer, 1957]; and first mathematical formulations of a law of motion were proposed, even though changes in movement of bodies were still considered of divine origin. There were also those who proposed that gravity acted between the centers of gravity of bodies, but the divine explanation was still strong and this idea was strongly criticized because occult properties were assigned to points in space. In this period, the basis for the scientific investigation of interaction forces was established and, thanks to alchemy and astronomy, the discipline of physics and chemistry were also shaped. With Galileo Galilei (1564-1642), we come to the first systematic experiments on gravity, motion of bodies, optics, astronomy and proof of the existence of vacuum [Galileo, 1952]. Testing his theories with direct experimental evidences, he introduced the modern scientific method, while Francis Bacon (1561-1626) introduced the concept of inductive reasoning and of experimental research. In the same period, the mathematician and astronomer Johannes Kepler (1571-1630) began the quantitative mapping of the motions and orbits of planets, albeit with the notion that the origin of gravitation was magnetic, which was a great help to Newton in the development of his laws of motion and gravitation [Jammer, 1957].

The 17^{th} century saw a transition, from just the observation and experimentation to the quantification of experimental data. This was Isaac Newton's (1642-1727) moment: he contributed to the understanding of matter on the molecular scale about structure and interactions. With his theories, he introduced the concept that matter and light were composed of particles that attracted each other by gravity. This hypothesis ran against the ideas of Robert Boyle (1627-1691), who had proposed 20 years before that the particles repel each other. How could this contradiction be resolved? He knew that gas particles could condense to form liquids and solids: in doing so, they had to attract each other, maybe at smaller distance, but they also had to repel, otherwise the material could "disappear". His conclusion, developed simultaneously with Gottfried Leibniz (1646-1716), was that particles attract as $1/r^2$ (inverse-square law of gravitation) and at smaller distance they repeal as $1/r$. From the beginning of 19^{th} century, these facts regarding the apparent contradictions between attraction and repulsion, generated many different and conflicting theories about the structure of matter and its interactions.

1.1.1 Van der Waals forces

An important step forward in the research about intermolecular forces was made in 1802 when Jacques Charles and Joseph Gay-Lussac published the equation of state for an ideal gas ($PV = nRT$), where P is the pression of the gas, V the volume, n the amount of substance in mole, R_g the ideal gas constant and T the absolute temperature of the system. This was followed by Johannes Diderik van der Waals (1837-1923) idea of attractive forces between molecules in gases in attempting to explain why gases did not obey the Charles and Gay-Lussac's equation. In 1837 Van der Waals proposed the following formula for real gases:

$$\left(P + \frac{a}{V^2}\right)(V - b) = R_g T, \tag{1.1}$$

where a is a parameter representing a measure of the average attraction between particles, and b, the volume excluded from V by one particle. In this formula he introduced two corrections: the first correction,a/V^2, took into account attractive intermolecular forces, known since as Van der Waals forces; the second correction, b, accounted for the finite size of gas molecules. Van der Waals hypothesis regarding forces was finally able to begin to explain intermolecular interactions, something that the too weak gravitational forces could not do. It is now known that these forces are dominant for distances from 1 nm out to several hundred nanometers, while below 1 nm, they become repulsive. From this early work, scientists began to search for ways to generalize this law of forces in order to explain the reason of intermolecular interactions. In the first two decades of 1900, Peter Debye (1884 - 1966) introduced the concept of dipole moment applied to the charge distribution in asymmetric molecules, and Willem Hendrik Keesom (1876 - 1956) described mathematically the dipole-dipole interaction. These two kinds of interactions were included in the Van der Waals forces and depend on whether the interacting materials are polar or not.There is also a third contribution discovered in 1930, by Fritz London (1907 - 1970): it is the dispersion forces, always present because they are caused by electrons orbiting around their nuclei and generating instantaneous dipole moments (Figure 1.1). London's contribution can be more significant than that of the Debye and Keesom, depending on the polarizability of the materials. An expression from classical arguments can be obtained beginning from a dispersion interaction between two Bohr atoms. Let's consider an atom with a dipole $p_1 = qa_0$, where a_0 is the Bohr radius and q is its charge, which generates an electric field E_2:

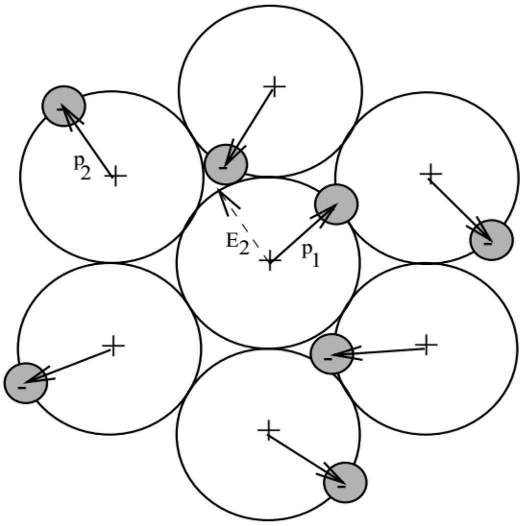

Figure 1.1: Schematic of the coordinates for the classical model for the dispersion interaction.

$$E_2 = \frac{p_1}{4\pi\epsilon_0 a_0^3}, \tag{1.2}$$

which induces a dipole moment p_2, to a second atom:

$$p_2 = \alpha E_2, \tag{1.3}$$

where α is the polarizability of the atom or molecule, and has the following expression:

$$\alpha = \frac{p_2}{E_2} = \frac{qa_0}{\frac{q}{4\pi\epsilon_0 a_0^2}} = 4\pi\epsilon_0 a_0^3. \tag{1.4}$$

The energy of the second dipole can be expressed as

$$U = -p_2 E_2 = -\frac{\alpha q^2 a_0^2}{(4\pi\epsilon_0)^2 r^6} \tag{1.5}$$

where r is the separation between the two interacting molecules. Substituting the Bohr radius with the following relationship with ν, the orbiting frequency of the electron in a Bohr atom,

$$a_0 = \frac{q^2}{2(4\pi\epsilon_0)^2 h\nu}. \tag{1.6}$$

The energy of the second dipole can be expressed as

$$U = -\frac{2h\nu\alpha^2}{(4\pi\epsilon_0)^2 r^6}. \tag{1.7}$$

Actually, London provided a rigorous and quantitative description of this phenomenon by quantum mechanics theory and obtained the same power-law dependence [London, 1937]:

$$U = -\frac{3}{4}\frac{\alpha^2 h\nu}{(4\pi\epsilon_0)^2 r^6} = -\frac{C}{r^6}, \tag{1.8}$$

where C is a constant.

Mie and Lennard-Jones potentials

It has to be underlined that, until London considered the combination of the influence of the Keesom, Debye and dispersion interactions, several models were developed to describe the observed repulsive and attractive forces by interaction potential between atoms and molecules. All of these approaches were empirical, the most noticeable and still used are the Mie and Lennard-Jones potentials, respectively. Let's make a small jump back in time and look at them in some detail.

At the beginning of 1900, it was clear that intermolecular forces were not of a simple nature. The scientific community was still not able to interpret them, although attempts were made to explain these phenomena empirically. In 1903, Gustav Mie (1869 - 1957) proposed an interaction potential of the form [Mie, 1903]

$$w(r) = -\frac{A}{r^n} + \frac{B}{r^m}, \tag{1.9}$$

where, for the first time, a repulsive term was included. The Mie potential was and still is used for a wide range of phenomena and the constants A and B can be related to the Van der Waals equation of state.

In 1924, just few years before the London's quantum mechanics description, a British mathematician, Sir John Edward Lennard-Jones (1894- 1954), proposed a potential based on the same analytical expression as that of form as Mie's 1.9, in order to describe the interaction between a pair of neutral atoms or molecules [Lennard-Jones, 1924]. Known also as the "6-12" potential, it has the following expression:

$$w(r) = 4\epsilon \left[\left(\frac{r_0}{r} \right)^{12} - \left(\frac{r_0}{r} \right)^{6} \right], \tag{1.10}$$

where ϵ is the minimum of the potential, r_0 is the distance at which the inter-particle potential becomes zero, and r is the distance between two particles. The r^{-12} term is the repulsive term and describes the short range repulsion due to the overlapping of the electron orbitals (Pauli repulsion), and the r^{-6} term describes the long range attraction (van der Waals forces, or dispersion force). The Lennard-Jones potential has been shown to be quite a good approximation and, due to its simplicity, it is still used to describe the properties of gases and to model dispersion and overlapping interactions in molecular models, especially in the case of neutral atoms and molecules, as in noble gases.

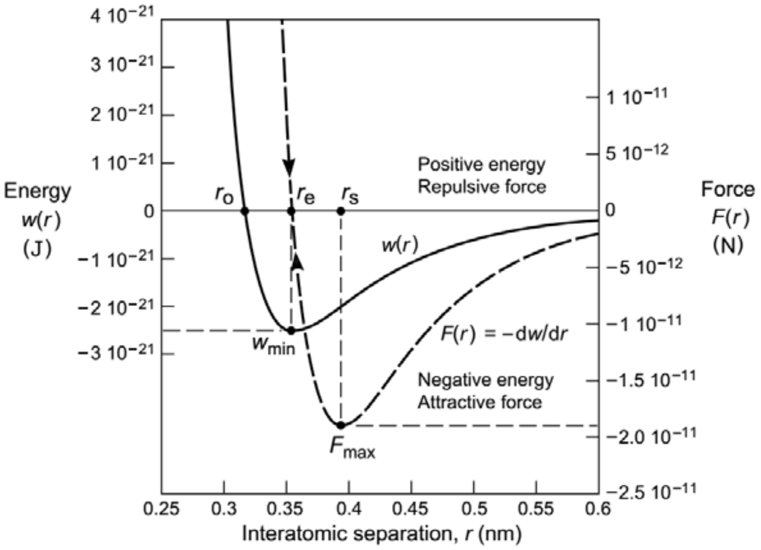

Figure 1.2: Typical Lennard-Jones potential describing van der Waals interaction energy function $w(r)$ and force function $F(r)$ between two atoms. The relation between the two function is $F(r) = -\frac{dw}{dr}$. r_e is the equilibrium distance where the force is zero, r_s represents the the separation at which the maximum force has to been applied in order to separate the two atoms. The plotted curves are for a Lennard- Jones potential, with parameters $A = 10^{-77} Jm^6 and B = 10^{-134} Jm^{12}$. Figure extracted from [Israelachvili, 2011].

Microscopic model

With the advent of the theory of relativity and the introduction of the speed of light as a constant, the retardation effect when the interacting atoms or molecules have a separation distance on the order of the characteristic absorption wavelength, was taken in account. This retardation effect is caused by the finite time that is required for the field transmitted from a fluctuating dipole to reach a neighbouring atom and then return. There is retardation when the distance the field travels is comparable to the period of the fluctuation. This effect decreases the power-law of the interaction by an order of magnitude. As the separation increases, there is a gradual transition back to the non-retarded power-law dependence. Taking the retarded and non-retarded effects into account, a general expression for the van der Waals forces between atoms and molecules is:

$$F_{mol}(z) = -\frac{C_{nr}}{z^7} - \frac{C_r}{z^8}, \tag{1.11}$$

where C_{nr} and C_r are the non-retarded and retarded London coefficients [London, 1937].

Assuming that the Van der Waals potential between atoms is additive, Hugo Christiaan Hamaker (1905 - 1993) used the London's model to calculate the interaction between two spheres and a sphere and a flat surface [Hamaker, 1937], integrating the interaction over their geometric shapes. This model is known as the microscopic model because it is based on the summation over the contributions of each atoms contained in the objects involved. The general potential interaction, using equation 1.11 is:

$$U_{micro} = \int_{body1} \int_{body2} \left(\frac{C_{nr}}{z^6} + \frac{C_r}{z^7} \right) d\Omega_1 d\Omega_2 \tag{1.12}$$

where Ω_1 and Ω_2 refer to the interacting bodies. As usual, the interacting force is obtained from the derivative of the potential interaction. Hamaker was one of the first to derive a theory for an interaction across an interface, so the coefficients bear his name and measures the relative strength of the attractive van der Waals forces between two surfaces. The general form of this constants is:

$$H_i = \pi^2 C_i \rho_1 \rho_2 \tag{1.13}$$

$$i = (nr, r) \tag{1.14}$$

where i indicates the non-retarded and retarded coefficient, C_i are the London coefficients and ρ_1 andρ_2 are the atomic densities of the two objects [Hamaker, 1937]. Although this approach ignores the contributions of neighbouring atoms, the result is consistent with more complete models derived using quantum theory [Langbein, 1973].

Macroscopic Model

The problem of the microscopic model, described above, is that the contribution of dispersion forces is not additive. The problem of half spaces separated by vacuum using a continuum approach and a macroscopic model based on quantum field theory was first developed in 1956 by Evgeny Lifshitz (1915 - 1985) [Lifshitz, 1956]. This new approach consisted of considering the interaction forces as a result of the resulting fluctuating electromagnetic field present between the two media, instead of considering the summation of each individual fluctuating dipole of the two half spaces. In 1961, Liftshitz with Dzyaloshinskii and Pitaeevskii generalized his original model relating the interaction forces with the optical properties of the media. The DLP model [Dzyaloshinskii et al., 1961] takes into account two media with dielectric constants ϵ_i, with $i = (1, 2)$, separated by as third medium of thickness l and dielectric constant ϵ_3. By using of the macroscopic properties of the materials, the same power-law dependence is obtained, and the Hamaker constants are an expression of the optical properties of the interacting materials. Just to give an idea of the model, the general expression for the force per unit area, f_{DLP}, between the two media is shown below:

$$f_{DLP} = \frac{\hbar}{2\pi^2 c^3} \int_0^\infty \int_1^\infty dp\, d\xi p^2 \xi^3 \epsilon_3^{\frac{3}{2}}$$
$$\left\{ \left[\frac{(s_1 + p)(s_2 + p)}{(s_1 - p)(s_2 - p)} \epsilon^{\frac{2p\xi l \sqrt{\epsilon_3}}{c}} - 1 \right]^{-1} + \left[\frac{(s_1 + p^{\frac{\epsilon_1}{\epsilon_3}})(s_2 + p^{\frac{\epsilon_2}{\epsilon_3}})}{(s_1 - p^{\frac{\epsilon_1}{\epsilon_3}})(s_2 - p^{\frac{\epsilon_2}{\epsilon_3}})} \epsilon^{\frac{2p\xi l \sqrt{\epsilon_3}}{c}} - 1 \right]^{-1} \right\}. \tag{1.15}$$

$$s_1 = \sqrt{\frac{\epsilon_1}{\epsilon_3} - 1 + p^2} \tag{1.16}$$

$$s_2 = \sqrt{\frac{\epsilon_2}{\epsilon_3} - 1 + p^2} \tag{1.17}$$

p and ξ are variables of integration related to the electromagnetic wave vectors. In order to calculate the integral, it is necessary to know the dielectric behaviour of the media over the entire electromagnetic spectrum. The typical expression for the permittivity is

$$\epsilon(\omega) = 1 + \frac{C}{\omega_0^2 - \omega^2 + i\Delta\omega \cdot \omega}, \tag{1.18}$$

where C is a constant, ω_0 is the resonance frequency of the media, where the material shows the strongest absorption peak, and $\Delta\omega$ is the half width of the absorption peak. Permittivity is, actually, a complex function with the following form,

$$\epsilon(\omega) = \epsilon^{'}(\omega) + i\epsilon^{''}(\omega). \tag{1.19}$$

By the Kramers-Kronig relation:

$$\epsilon(i\xi) = 1 + \frac{2}{\pi} \int_0^\infty \frac{\omega \epsilon^{''}(\omega)}{\omega^2 + \xi^2} d\omega \tag{1.20}$$

it is possible to calculate the integral, assuming $\epsilon''(\omega)$ know.

In the case of a small separation compared with the absorption wavelengths of the dielectric, therefore in case of non-retarded regime, the expression for the force is

$$f_{nr} = \frac{\hbar}{8\pi^2 z^3} \int_0^\infty \sum_{n=1}^{\infty} \frac{1}{n^3} \left[\frac{(\epsilon_1 - \epsilon_3)(\epsilon_2 - \epsilon_3)}{(\epsilon_1 + \epsilon_3)(\epsilon_2 + \epsilon_3)} \right]^n d\xi = \frac{H_{132}}{6\pi z^3}, \tag{1.21}$$

where H_{132} is the Hamaker constant for this media configuration in a non-retarded regime. For large separations, that is in retarded regime, the expression has an increased power-law dependence,

$$f_r = \frac{\pi^2 \hbar c}{240 z^4 \sqrt{\epsilon_3(0)}} \left(\frac{(\epsilon_1(0) - \epsilon_3(0))(\epsilon_2(0) - \epsilon_3(0))}{(\epsilon_1(0) + \epsilon_3(0))(\epsilon_2(0) + \epsilon_3(0))} \right) \phi(\epsilon_1(0), \epsilon_2(0), \epsilon_3(0)) = \frac{H_r}{z^4}. \tag{1.22}$$

where H_r is the Hamaker constant for this configuration in retarded regime and $\phi(\epsilon_1(0), \epsilon_2(0), \epsilon_3(0))$ is a function with value between 1 and $69/2\pi^4$, depending on the interacting media [Israelachvili and Tabor, 1972].

Since the 21^{st} century, several theories have been developed in order to describe interactions in different media between different kind of materials, dielectrics and metals. All these models always obtain the same power-law dependence for both the regimes, but differ in the way used to calculate the Hamaker constants. The Hamaker constants can also be calculated for the interaction between different geometries and a flat surface; for example, a model by Hartmann gives a general method [Hartmann, 1990] for this kind of calculation that can be applied to the interaction between an AFM tip, of known geometry, and a flat surface. The main problem from an experimental point of view in determining the Hamaker constant by fitting the attractive part of the approach curve, is the presence of the jump-to-contact (when the sum of the forces is attractive and therefore the tip jump into contact with the surface). In contrast, the main problem of measuring Van der Waals forces, is the characterization of the shape of the tip and the roughness of the sample, despite the fact that some studies on the comparison between modeling and experimental results has given comparable results [Zanette et al., 2000]. An adopted strategy to minimize the problems associated to the roughness and asperities is by attaching a particle with a large radius to the cantilever tip [Ducker et al., 1991,Segeren et al., 2002].

1.1.2 Electrostatic forces

As mentioned above, while electrostatic forces were first observed by the ancient Greeks, it was not until Charles Augustin de Coulomb (1736 - 1806), a french military engineer and physicist, that a force law between charged bodies was proposed, a law that is still used nowadays. The electrostatic force is a long-range force: it is additive and follows an inverse-square law. It depends on the spatial distribution of the charges on the interacting objects and can be repulsive or attractive, depending on whether the interacting charges have the same sign or not. When two different materials are brought in close proximity contact, since all matter has electric charges, a transfer of charge from one material to the other can occur, after separation, due to local inhomogeneities in the work function of the materials (the minimum energy needed to remove an electron from a solid to a point in the vacuum). This transfer generates a local dipole with moment $p = 4\pi\epsilon R^2 \Delta\phi$, where $\Delta\phi$ is the variation of the local work function. Restricting the phenomenon to two particles of radius R and separated by a distance r, the force on each particle will have a maximum value of [Rimai and DeMejo, 1996]:

$$F_{max} = \frac{3p^2}{\pi\epsilon_0 r^4} = 48\pi\epsilon_0 \left(\frac{R}{r}\right)^4 ; \tag{1.23}$$

and it varies with the dipole orientation. There are several ways in which particles can acquire charge: for example from triboelectric effect [Burgo et al., 2012, Burgo et al., 2013]. Tribocharging leads to an expected non-uniform charge distribution which can influence adhesion in a significant way. Despite the simplicity of the expression for the Coulomb force, calculating the net electrostatic interaction force is not straightforward: in the case of an AFM experiment, for example, the tribocharging, the unknown geometry of the AFM tip and the roughness of the topography contribute to complicate the boundary conditions of the system. Moreover, while for conductive tip and sample surface the boundary conditions of constant potential are valid, for insulating surfaces and tip, the constant potential condition is no longer valid. In any event, no simple analytical expression can be derived to describe the tip-sample interaction [Gady et al., 1997, Gómez-Monivas et al., 2001]. The interaction range is usually much shorter than expected and measuring the Coulomb forces can be useful to obtain information about tip shape and mechanical deformation when in contact [Leite and Herrmann, 2005, Lambert and Regnier, 2010, Cappella and Dietler, 1999]. In fact, several models have been implemented for this purpose [Butt et al., 2005, Hao et al., 1991, Patil et al., 2000, Patil and Dharmadhikari, 2002].

1.1.3 Capillary forces

Due to condensation of the surrounding humidity, droplets or a thin layer of liquid form on the surfaces. When two objects approach to each other, a meniscus between them is formed and capillary forces arise. These forces are also called surface tension forces because they actually arise from the surface tension of the interface between the two media. These kind of forces are really important because they can be stronger than other effects, such as electrostatic or chemical bonds forces, apart from Van der Waals forces with which can be comparable at nano-scale. Moreover, humidity is everywhere in ambient conditions and if the experiment is not performed in a controlled environment, the presence of water is guaranteed.

The fundamental equation describing capillary condensation dates back to the work of William Thomson (1824 – 1907), also known as Lord Kelvin. In 1870, he managed to describe how the vapour pressure of a liquid depends on the curvature of the liquid, using the equation:

$$R_g T \ln \frac{P}{P_0} = \gamma V_m \left(\frac{1}{R_1} + \frac{1}{R_2} \right), \tag{1.24}$$

where T stands for the temperature, V_m the molar volume of the liquid, P_0 the vapour pressure of the planar liquid, P the vapour pressure of the curved liquid, γ the surface tension of the liquid, and R_1 and R_2 are the radii of curvature. The system, consisting of a sphere in contact with a flat surface, and its parameters are shown in figure 1.3. The effective vapour pressure reduces with the curvature of the surface, therefore condensation can occur at relative humidity much below 100% for small radii of curvature. The pressure difference between the liquid and the surrounding vapour phase leads to the formation of a meniscus which exerts an attractive force between the sphere, first approximation of an AFM tip, and the surface. In 1804, Thomas Young, provided a way to describe this difference of pressure with his theoretical work about surface tension, capillary phenomena and contact angle of a liquid surface in contact with a solid. One year later, Pierre-Simon Laplace discovered the significance of meniscus radii related to capillary action. Finally, in 1830, Carl Friedrich Gauss unified the work of his two colleagues deriving the Young-Laplace equation, describing this difference of pressure:

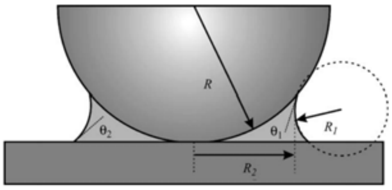

Figure 1.3: Schematic of a water meniscus between a sphere with radius R and a flat surface. R_1 and R_2 are the two characteristic radii for the meniscus, while θ_1 and θ_2 are the relative angles. Figure extracted from [Butt et al., 2005].

$$\Delta P = \gamma \left(\frac{1}{R_1} + \frac{1}{R_2} \right). \tag{1.25}$$

The capillary force F_{cap} between a sphere with radius R and a flat surface, was later calculated by O'Brien and Hermann in the 1973 [O'Brien and Hermann, 1973] using this expression:

$$F_{cap} = 2\pi R\gamma(\cos\theta_1 + \cos\theta_2), \tag{1.26}$$

where θ_1 and θ_2 are the contact angles between the two surfaces (sphere and flat surface) and the liquid, as shown in figure 1.3. Comparing the contributions of the meniscus, Van der Waals and electrostatic force under ambient conditions (around 50% of relative humidity), the meniscus makes the largest contribution to adhesion. Obviously, as equation 1.26 shows, the capillary force is expected to be higher for hydrophilic surfaces and lower or null for hydrophobic surfaces as a result of differences in the size of contact angles ($\theta_1, \theta_2 < 90°$ for hydrophilic surfaces and $\theta_1, \theta_2 > 90°$ for hydrophobic surfaces). This finding has since been confirmed by several studies showing a decrease in capillary force with an increase in hydrophobicity [Bhushan and Dandavate, 2000, Xiao and Qian, 2000, Jones et al., 2002, Fuji et al., 1999].

Parameters not taken in account in the Young-Laplace equation 1.25, are the relative humidity and the roughness: it is known that as humidity increases, mostly with granular matter, cohesion increases as higher roughness leads to many small menisci localized on the asperities. Formation of these numerous liquid bridges between asperities, creates one large meniscus and a higher meniscus force [Bocquet and Barrat, 1993]. In recent years, many experiments and theoretical models have been performed and developed to describe this kind of force including humidity [Ando, 2000, Fuji et al., 1998], condensation time of the liquid [Bocquet and Barrat, 1993], roughness [Ata et al., 2002, Rabinovich et al., 2002], and retract speed in the case of moving objects like an AFM tip [Wei and Zhao, 2004]. With regard to the AFM tip, the meniscus interaction between AFM tip and flat [de Lazzer et al., 1999, Stifter et al., 2000] or curved surfaces has been studied [Sirghi et al., 2000, de Lazzer et al., 1999], with the finding that the local curvature strongly affects the capillary force. A larger adhesive force for a concave and a smaller for a convex surface was found, as compared to a flat surface. Meniscus forces show a complex behaviour depending on surface roughness, geometry, and hydrophilicity. Nevertheless, various discrepancies stil have to be clarified, as kinetics of neck formation and how water layers distribute at the surface are issues still not well understood.

1.1.4 Solvation forces

In general, liquid distribution change from the bulk to the region near a surface or an interface. The liquid density profiles and potentials of mean force between two solute molecules in a solvent medium oscillate with a periodicity close to the molecular diameter of the solvent molecules and within a range of a few solvent molecules. In case of the presence of an extended surface, oscillating short-distance interactions also arise and they are referred to as solvation forces; in the case of a water medium, they are referred to as hydration forces. In principle, solvent molecules at an interface do not behave differently from how they can organize around a small solute molecule or even around an solvent molecule of the same kind. But at a solid-liquid interface, theoretical studies and computer simulations [Evans and Parry, 1990] show how attractive interactions between the surface and liquid molecules force them to order into quasi-discrete layers. These layers shows an oscillatory density profile, extended for several molecular diameters into the liquid medium [Abraham, 1978, Rao et al., 1979]. In the ideal case of a flat surface, the molecules randomly order whithin each layer and show a liquid-like ordered layering effect organization only in a short range, tipically about 1nm. If the surface is structured at the atomic level, as in a crystalline lattice, then an epitaxial sort of ordering of the liquid-molecules may be induced within the several layers [Cheng et al., 2010, Israelachvili and Pashley, 1983].

In the case of a liquid confined between two surfaces, the liquid molecules order themselves and this ordering makes solvation forces arise between the confining surfaces even if there is not any attractive or structured interaction between the liquid and surfaces. In the simplest case of spherical molecules interacting with hard and smooth surfaces, the solvation force has usually an exponentially decaying oscillatory behaviour depending on the distance (as shown in Figure 1.4)

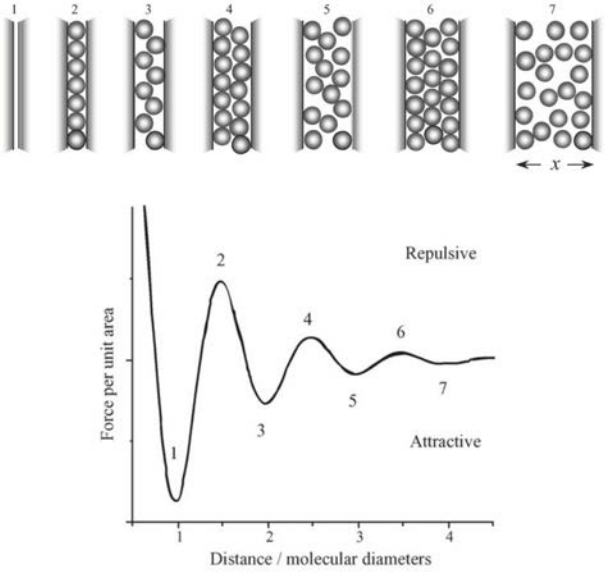

Figure 1.4: Schematic structure of a liquid confined between two parallel and smooth surfaces. The ordering of the molecules changes with the distance x of the two surfaces, resulting in an oscillatory force. Figure extracted from [Butt et al., 2005]

and often well described by function of the form:

$$f = f_0 \cos \frac{2\pi x}{\sigma} e^{-x/\lambda_S}, \tag{1.27}$$

where σ is the molecular diameter, λ_s the decay length, and x the distance between the confining surfaces. Using the Derjaguin's approximation, it is possible to calculate the force between a sphere of radius R, approaching a flat surface at distance D [Horn and Israelachvili, 1981]:

$$F = F_0 \cos \frac{2\pi D}{\sigma} + \phi e^{-D/\lambda_S}. \tag{1.28}$$

Phase shift ϕ and the measured force amplitude are obtained by $\tan(\phi) = \frac{\lambda_S}{\sigma}$ and $F_0 = Rf_0 / \sqrt{(2\pi\lambda_S)^{-2} + \sigma^{-2}}$, respectively. From the expression for the phase shift, it is noticeable that the distance needed to make the inner layer of the liquid in contact with the surface is smaller than the distances needed for the other layers.

In the case of molecules with asymmetric shapes or having an anisotropic or non pair-wise additive interaction potential, the solvation force of the system can be very complex and show a monotonically repulsive or attractive component. The same can happen if the confining surfaces are rough or in anyway not well-ordered, also resulting in smoothed oscillations. Measurements of solvation forces with AFM are usually performed by force-distance curves (see subsection 2.2.1). The problem with this kind of experiment is the lack of a trustworthy zero distance reference. Considering the zero distance as the closest distance approach, there is the possibility of still not having penetrated several layers. Studies have been conducted in this direction, with a solution found in combining force and conduction measurements [Klein and McEuen, 1995].

1.1.5 Adhesion

When two dissimilar particles or surfaces come into contact, they tend to adhere. Let us consider, in an AFM force-distance curve, the moment at which the tip is retracting: it stays in contact with the surface until the force exerted by the cantilever overwhelms the sum of the interaction forces between tip and sample. The first measurements of this adhesive force F_{ad} date back to 1988, when Martin (1988) and Erlandsson (1988) performed capacitance and friction measurements on mica, respectively. Generally, the adhesion force is constituted by contributions from the electrostatic force F_{el}, the Van der Waals force F_{vdW}, the capillary force F_{cap} and the forces due to chemical interactions F_{chem}:

$$F_{ad} = F_{el} + F_{vdW} + F_{cap} + F_{chem}. \tag{1.29}$$

In the case of insulators surfaces in gaseous or low humid environments, the electrostatic contribution is expected to be dominant due to the ineffective charge dissipation. The van der Waals contribution is always present and in most cases it is attractive (because of the tip-surfac distance), as it is the capillary force due to the formation of a water neck between tip and sample surface in ambient conditions and it depends on the relative humidity and the level of hydrophilicity of the tip and sample surface. Usually, the boundary conditions in AFM studies on adhesion force are chosen in order to make the van der Waals contribution dominant; in this way, the adhesion force is mainly given by the Hamaker constant, determined by tip-sample interaction, and by the contact geometry. Contact geometry is usually hard to determine precisely, and along with surface roughness and the adsorption of contaminants on the surface, the comparison between experimental results and theoretical predictions can become really difficult. Roughness affects the determination of contact region, as shown in studies where the expected adhesion force value was higher than the measured one [Schaefer et al., 1994, Schaefer et al., 1995]. Models, describing how surface roughness influences the adhesion, have been studied considering a single asperity with a known radius [Rumpf, 1990], different length scales of surface roughness [Rabinovich et al., 2000a], distribution of asperities [Cooper et al., 2000] and even modeling by fractals and fast Fourier transform algorithms [Eichenlaub et al., 2004]. Since the main way to determine surface roughness is the root mean square value of z value in topography images, and not the mean asperity radius, some of these models have been modified in order to make them applicable for experimental purposes [Rabinovich et al., 2000b, Rabinovich et al., 2000a]. All these models agree on the fact that asperities reduce the adhesion force, impeding close contact between particles and surface. Experimental results confirm the value of these models [Rabinovich et al., 2000a, Beach et al., 2002] finding that they describe adequately the decrease of adhesion with the increase of surface roughness.

1.2 Contact mechanics and mechanical models

Contact mechanics can be defined as the study of how two bodies deform coming into contact and is divided into two branches: when the stress acts perpendicularly to the surfaces of the bodies in contact, we are speaking about deformation and, when the stress acts tangentially, we are speaking about frictional stresses or tribology. Since the 15^{th} century tribology has been studied: scientists such as Leonardo da Vinci, Leonhard Euler (the first to approach the problem mathematically) and C. A. de Coulomb put the basis, experimentally and theoretically, to understand and describe this phenomena. The first studies on deformation took place in the 17^{th} and 18^{th} centuries by R. Hooke, J. L. Lagrange and J. R. d'Alembert. But H. Hertz (1882) was the first to solve the contact problem of two elastic bodies with curved surfaces [Hertz, 1882]. After him, the most important theories that included the adhesion where those of Johnson, Kendall & Roberts (1971) who developed their model (JKR) in 1971 together with the Derjaguin-Müller-Toporov (DMT) model [Derjaguin et al., 1975, Muller et al., 1980, Muller et al., 1983] and the more general Maugis theory [Maugis, 1992].

Before giving an overview of these contact mechanics models, it is necessary to introduce some concepts. One method well suited to study contact mechanics at the nano-scale and to quantify the physical quantities involved consists in performing force distance curves with AFM. When the AFM tip, or more generally a body, comes into contact with a surface, both surfaces deform. If the exerted force by the tip on the surface is below a critical value (yielding point), the surface return to its previous status once the tip retracts: in this case the deformation is reversible and defined as elastic. This elastic deformation δ is necessary to relate the measured quantities to the elastic modulus of the surface, also called Young's modulus (E) because of the English physicist Thomas Young who introduced it in 1807 [Young, 1845]. E can be defined as the ratio between the tensile stress σ and the strain ϵ:

$$E \equiv \frac{\sigma(\epsilon)}{\epsilon} = \frac{F/A}{\delta/L_0} = \frac{FL_0}{A\delta}, \tag{1.30}$$

where F is the force exerted on the surface, A is the area of the cross-section perpendicular to the applied force, δ is the deformation, L_0 is the original length of the object (in case of a surface, L_0 is the length of the vertical cross-section of the considered surface). In the case of elastic deformation using AFM, a useful parameter to take in account is the potential energy U:

$$U = U_{ts}(d) + U_c(u) + U_s(\delta) = U_{ts}(d) + \frac{1}{2}k_c u^2 + \frac{1}{2}k_s\delta^2. \tag{1.31}$$

In this expression U_{ts} is the tip-sample interaction potential due to surface forces, U_c the energy related to the cantilever bending, U_s the elastic deformation energy of the sample surface, and k_s is the surface sample stiffness. d is the tip-sample distance and can be written, assuming that the tip does not deform, as the sum of the height position of piezo Z that displaces the cantilever, the cantilever deflection u and the surface sample deformation δ,

$$d = Z + u + \delta. \tag{1.32}$$

In contact $d = 0$ and, in the case of equilibrium, the Hooke's law can be written as $k_s\delta = k_c u$. Writing δ in terms of Z and u, we obtain:

$$k_c u = -\frac{k_c k_s}{k_c + k_s} Z = k_{eff} Z. \tag{1.33}$$

This relation shows how the slope of the force-displacement curve is related to the stiffness of the sample and how the cantilever spring constant has a crucial role in this kind of measurement. In fact, if the cantilever spring constant is much lower ($k_s >> k_c$) than the sample spring constant, $k_{eff} \approx k_c$, meaning that the force curve mainly probes the stiffness of the cantilever and not of the sample surface. This fact is important to take in account when the exerted forces are calibrated in force-distance curve measurement (see the subsection 2.2.3 about calibration methods).

The Young's modulus is related to the sample stiffness by the following relations [Butt et al., 2005]

$$k_s = \frac{3}{2} a E^* \tag{1.34}$$

$$\frac{1}{E^*} = \frac{3}{4}\left(\frac{1-\nu_s^2}{E_s} + \frac{1-\nu_t^2}{E_t}\right) \tag{1.35}$$

where ν_t and ν_s, are the Poisson's ratio (the ratio of transverse strain to axial strain) of the tip and the surface, respectively. E_t and E_s are the Young's modulus of tip and sample, E^* the reduced Young's modulus and a the tip-sample contact radius. In the case that the tip is much stiffer than the sample surface, the tip deformation is negligible and the equation 1.34 can be written as

$$k_s = 2a\left(\frac{E_s}{1-\nu_s^2}\right) \tag{1.36}$$

The several theories that describe the elastic deformation of the sample surface differ in the relations between the applied load F, the contact radius a and deformation δ due to the consideration of the presence or not of adhesion in the system.

There are several problems to take into account with respect of the mechanical contact problem. Beginning with the adhesion-less contact model and considering an axis-symmetric punch exerting a force against a rigid flat surface, mixed boundary conditions have to be taken into account. In this regard, the stresses normal to the surface are considered outside the contact zone while the displacements normal to the surface are considered inside. Moreover, as loading increases, the force F exerted on the surface, a increases and so does the penetration δ, but in a non-linear way. A possible solution to these problems is to consider an equilibrium stress field, associated with a displacement field, that provides a set of two relations called contact equations and that relate the three macroscopic contact variables a, δ and F.

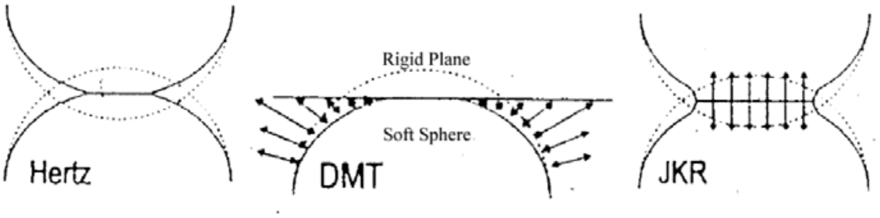

Figure 1.5: Schematic of the interactions included in the different models: Hertz considers just fully elastic contact; JKR considers fully elastic contact with adhesion forces inside the contact zone; DMT considers fully elastic contact with adhesive forces and Van der Waals forces around the contact area. Figure extracted and modified from [Johnson, 1985].

1.2.1 Hertz model

Known for proving the existence of electromagnetic waves, Heinrich Hertz was the first to study the topic that came to be recognized as contact mechanics. In 1882, he solved the problem of two curved bodies in contact, as shown in figure 1.5, without taking into account adhesion forces: his work is valid in case of deformations much smaller than the sphere radius and it has been used as the base for successive models.

Considering a sphere of radius R, the punch shape $f(r)$ (r is the spatial coordinate) is:

$$f(r) = \frac{r^2}{2R} \tag{1.37}$$

In his work, Hertz (1882) demonstrated that an ellipsoidal distribution of contact stresses, inside the contact area, flattens the elastic sphere. The penetration depth, or indentation, δ_H can be related to the radius R of the sphere and the contact radius a by the expression

$$\delta_H(a) = \frac{a^2}{R} \tag{1.38}$$

and the force can be expressed in terms of contact radius by

$$F_H(a) = \frac{4E^* a^3}{3R}. \tag{1.39}$$

Equations 1.38 and 1.39 are the contact equations for an adhesion-free elastic contact of spheres. In adhesion-less contact theory, the distance between two opposite surfaces outside the contact zone is called gap and denoted as $h_H(r)$. This gap is due to the deformation of the punch shape $f(r)$ for effect of the non local elastic response to the contact and adhesive interaction stresses (the last one if present).

1.2.2 DMT model

As mentioned above, the Hertz model does not include adhesion forces. The first model, which included adhesion, was proposed by Derjaguin in 1934 [Derjaguin, 1934]. In this study, the assumption is that the contact stresses and the gap are the same as in the Hertz model. The adhesion is included as energy w necessary to separate a unit area of contacting surfaces. Including adhesion energy w and indicating elastic energy as E_H, the total energy of the system is

$$E(\delta) = E_H(\delta) - w(\pi a^2) \tag{1.40}$$

and from the derivative with respect to δ we obtain the force. In this way the contact equations (equation 1.38 and 1.39) become

$$\delta_D = \delta_H(a) \tag{1.41}$$

$$F_D = F_H(a) - \pi R w. \tag{1.42}$$

As can be noted, in this earlier model the force is Hertzian with an offset of $-\pi w R$. This offset is defined as pull-out force, in other word the force required to separate the surfaces, and it is also the minimum of the force-penetration curve. This model is a useful approximation to obtain an estimation for order of magnitudes of elastic adhesive contact properties [Johnson et al., 1971].

In this first model, Derjaguin also introduced attractive interactions between surfaces not in contact but at close proximity. Separated by a distance $\delta > 0$, they are attracted to each other by a surface stress $\sigma_z(r)$ having radial distribution. The total force is

$$F_{ext} = 2\pi \int_0^\infty dr\, r\sigma_z(r). \tag{1.43}$$

Considering an interaction potential $V(z)$ between flat surfaces of unit area separated by a gap with boundary conditions

$$V(\infty) = 0 \text{ and } V(0) = V_0 \tag{1.44}$$

and considering the surface stress $\sigma_z(r)$ derived from this potential, it is possible to write equation 1.43 for a sphere as:

$$F_{ext}(\delta) = 2\pi R V(\delta), \tag{1.45}$$

where δ is the body displacement, and not the indentation depth because there is no contact. This approximation is used widely in surface forces measurements [Israelachvili, 2011]. This equation shows how the force between the sphere and the plane is proportional to the interaction potential between flat surfaces at the same distance and how this proportionality coefficient is the sphere radius. Introducing the attractive interactions in the form of the potential V, the new expression for the pull-out force is:

$$F_{p-o} = -2\pi R V_0. \tag{1.46}$$

Taking the separation between the surfaces $\delta = 0$ and comparing with the preview expression for the pull-out force, F_D in equation 1.42, it is clear how $w = 2V(0) = 2V_0$.

In order to understand this discrepancy, in 1983, Derjaguin and his coworkers worked on a "natural" extension of the Derjaguin approximation and proposed an adhesive contact theory, the DMT model [Muller et al., 1983, Pashley, 1984], which included contact stress. Hertzian stress distribution and deformation fields are included, as in the previous model [Derjaguin, 1934], but the adhesive interaction stresses are considered as an additional force and treated as in Derjaguin's approximation. In this way, the set of contact equations becomes:

$$\delta_{DMT} = \delta_H(a) \tag{1.47}$$

$$F_{DMT} = F_H(a) - F_{ext}(a), \tag{1.48}$$

where the external force term is

$$F_{ext}(a) = 2\pi \int_a^{\infty} dr\, r\sigma_z(r). \tag{1.49}$$

As with Derjaguin's approximation, the adhesive interaction stresses are related to the interaction potential $V(z)$ and the spatial distribution of attractive stresses is expressed in terms of this potential and the gap $h_H(r)$ introduced in the Hertz contact model, in the form:

$$\sigma_z(r) = -\frac{dV}{dz} h_H(r). \tag{1.50}$$

Knowing the interaction potential, the adhesive force F_{ext} can be calculated numerically [Pashley, 1984]. For the DMT contact model, the pull-out force is

$$F_{po} = -2\pi R w \tag{1.51}$$

because at contact radius $a = 0$, the DMT theory coincides with the Derjaguin approximation.

The DMT model is typically relevant for small rigid spheres and conditions where the contact radius is much smaller than the region over which the attractive interaction stresses act [Greenwood and Johnson, 1981]. In summary, the DMT

model depends on the reciprocal influence between the interaction potential and the punch shape. The adhesion energy w is not a very relevant parameter, the relevant one for adhesion is the amplitude V_0 of the interaction potential.
This model will be the one adopted in the work of thesis for the simulations and data analysis, as described in chapters 3 and 4

1.2.3 JKR model

Few years before the publication of the DMT model, in 1971, Johnson and his coworkers Kendall and Roberts observed the formation of a neck, of height δ_{neck} around the contact area of adhesive hemisphere [Johnson et al., 1971]. In their study, they found that the contact radius a was related to the work of adhesion. In case of soft materials, δ_{neck} is large enough and embrace the whole range of interaction δ_{int}; a contact radius variation Δa leads to a transfer of work, from the contact zone to the interacting sphere, equal to $w\, d(\pi a^2)$. Actually, Johnson and coworkers introduced the neck singularity in the first Derjaguin's model completing it. So the energy transfer appears to be controlled by the neck height δ_{neck} and from energy minimization [Johnson et al., 1971, Johnson, 1985] it was obtained how δ_{neck} is related to the reduced Young modulus E^* and the adhesion energy w:

$$2\pi a w = E^* \delta_{neck}^2. \tag{1.52}$$

From this equation it is understandable how, in the local treatment of the adhesive process, the neck height does not depend on the punch shape. In addition, the relevant parameters are the contact radius and the adhesion energy.

The contact equations for this model are obtained by linear superposition of the adhesion-less contact and flat punch solutions [Barthel, 2008]:

$$\delta(a) = \delta_H(a) + \delta_{neck} \tag{1.53}$$

$$F(a) = F_H(a) - F_{neck}(a). \tag{1.54}$$

Contrary to the DMT model, the flat punch term offsets both the hertzian terms of force and penetration. The correction terms are

$$F_{neck} = \delta_{neck} S(a) \tag{1.55}$$

$$S(a) = 2aE^* \tag{1.56}$$

and F_{neck} is linear in δ_{neck} because the contact radius a is constant. Equations 1.53 and 1.54 can be used for different kinds of punch shapes, being the most used in the majority of the experiments is the spherical one. For a homogenous elastic sphere, approximated by a paraboloid, the contact equations become:

$$\delta_{JKR} = \frac{a^2}{R} - \sqrt{\frac{2\pi a w}{E^*}} \tag{1.57}$$

$$F_{JKR} = \frac{4E^* a^3}{3R} - 2\sqrt{2\pi E^* w a^3} \tag{1.58}$$

Minimizing the total force F_{JKR}, it can be calculated the pull-out force, which results in:

$$F_{po} = -\frac{3}{2}\pi w R \tag{1.59}$$

The JKR model, contrary to the DMT one, is most suitable for large interaction stresses and compliant materials.

1.2.4 Maugis' model

As mentioned before, the Hertz model neglects adhesion contribution between the contacting surfaces, while the DMT model takes account of it outside the contact area and the JKR model inside of it, as schematically shown in figure 1.5. Both models are approximations. In fact, in the case of AFM tips, the DMT model is valid for small tip radius and stiff samples and the JKR theory is valid for large tip radius and soft samples. In 1992 with his work [Maugis, 1992], Maugis improved the previous Tabor's study [Tabor, 1977] of 1977 and showed how these two models are limits of the same theory. He described the elastic deformations of all samples as a function of the λ parameter:

$$\lambda = \frac{2.06}{D_0}\sqrt[3]{\frac{Rw^2}{\pi {E^*}^2}}, \tag{1.60}$$

where D_0 is a typical atomic dimension. The Maugis theory describes the deformation and the contact radius by the following set of parametric equations

$$\bar{\delta} = \bar{A}^2 - \frac{4}{3}\lambda \bar{A}\sqrt{m_M^2 - 1} \tag{1.61}$$

$$\bar{F} = \bar{A}^3 - \lambda \bar{A}^2 \left(\sqrt{m_M^2 - 1} + m_M^2 \arctan \sqrt{m_M^2 - 1}\right) \tag{1.62}$$

with

$$\bar{A} = \frac{a}{\sqrt[3]{\pi W R^2 / E^*}}, \qquad \bar{F} = \frac{F}{\pi W R}, \qquad \bar{\delta} = \frac{\delta}{\sqrt[3]{\pi^2 W^2 R / {E^*}^2}}, \tag{1.63}$$

and

$$\frac{\lambda \bar{A}^2}{2}\left[\sqrt{m_M^2 - 1} + (m_M^2 - 2)\arctan\sqrt{m_M^2 - 1}\right] + \frac{4\lambda^2 \bar{A}^2}{3}\left(1 - m_M^2 + \sqrt{m_M^2 - 1}\arctan\sqrt{m_M^2 - 1}\right) = 1, \tag{1.64}$$

where m_M is the ratio between the contact radius a and the annular adhesion region. Equation 1.62 gives the JKR contact equations for $\lambda \rightarrow \infty$ and the DMT contact equations for $\lambda \rightarrow 0$, respectively.

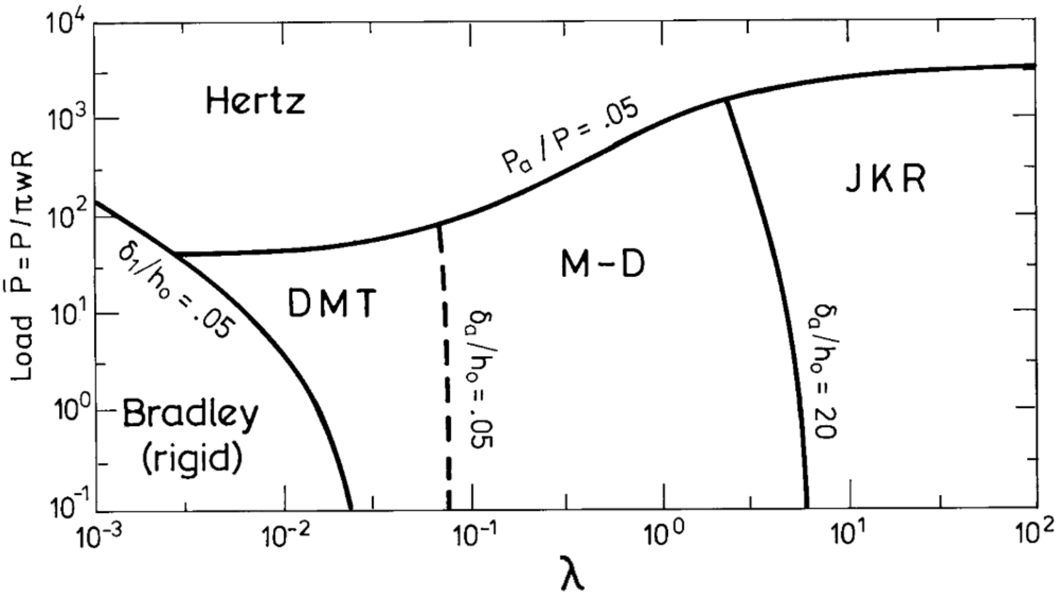

Figure 1.6: Map of the elastic behavior of bodies depending on load force and Maugi's λ parameter: in case of negligible adhesion, deformation falls in the Hertz limit; when the deformation is small the DMT theory is valid; JKR theory describes the behavior of bodies with high adhesion; the Maugi's theory is valid for the intermediate region. Graph extracted from [Johnson and Greenwood, 1997]

The Maugis theory tries to unify the different contact models, as shown in figure 1.6 and was experimentally verified by Lantz et al. [Lantz et al., 1997]. This theory showed also how it is impossible to determinate the Young's modulus E and the work of adhesion w exactly just by performing force-distance curves: in fact, the problem is self-recursive because the parameter λ depends on E and w.

In the case $R \longrightarrow 0$, which includes ultrasharp tips, the force exerted on the surface during indentation acts directly on the surface atoms and atomic bonds play a more crucial role in the mechanical response. The deformation becomes local, because of the smaller contact area, and less atoms are involved making in-plane interactions critical in the deformation of the surface. From an experimental point of view, it has been found that larger tip radius leads to an underestimation of the Young modulus value while smaller corner angles of the tip cause an overestimation of E [Calabri et al., 2008, Costa and Yin, 1999]. Several studies about models and analysis methods, in order to evaluate better the experimental results, can be found in the literature [Calabri et al., 2008, Choi et al., 2004, Fraxedas et al., 2002].

1.2.5 Viscoelasticity

Viscoelasticity has started to be studied more intensively in the last years of the twentieth century, because of the increasing importance of polymers. In fact, polymers and soft materials show both elastic (spring-like) and viscous (dashpot-like) behaviour when are subjected to deformation. The stress-strain relationship in this kind of material is time and temperature dependent and show three main properties: stress relaxation, i.e. decreasing stress produces a step constant strain (figure 1.7a); creep, increasing strain induces a step constant stress in the material (figure 1.7b); and hysteresis, there is a time delay in phase between the stress and the strain responses.

Hysteresis behaviour can be seen performing stress-strain curves on viscoelastic materials, where the loading curve is different from the unloading curve. In figure 1.8a, it is shown the stress-strain curve associated to an elastic material, where the loading and unloading curves cannot be differentiated. In In figure 1.8b, it is shown the stress-strain curve for a viscoelastic material: in this case, the loading and unloading curves can be distinguished exhibiting an hysteretical behaviour. Several theoretical models for viscoelasticity exists. The three most common models are: the Kelvin-Voigt model, which models viscoelasticity as a spring and a damper in parallel, figure 1.9a; the Maxwell model, a spring and a

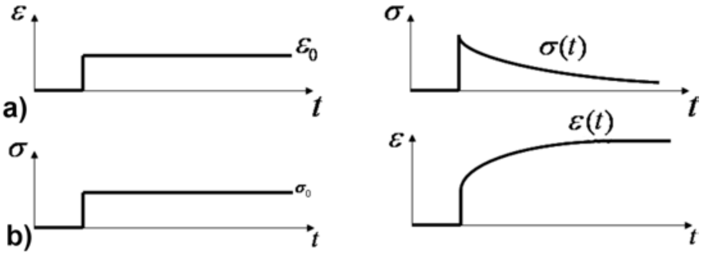

Figure 1.7: Stress (ϵ) and strain σ behaviour in a) stress relaxation test and b) creep test. Figure extracted from [Banks et al., 2011]

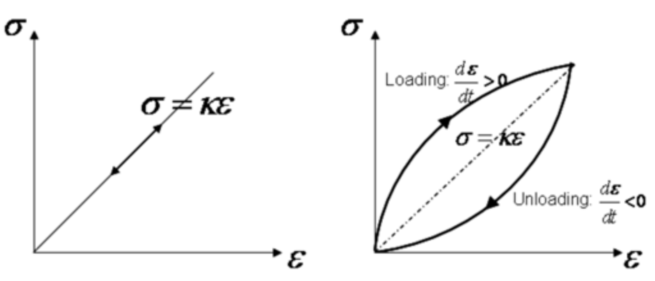

(a) (b)

Figure 1.8: Stress-strain curves in the case of a) elastic material and b) linear viscoelastic material. Figure extracted from [Banks et al., 2011]

.

damper in series, figure 1.9b; and the three elements model, a spring in series with a Kelvin-Voigt element as shown in figure 1.9c. The three element model will be used in chapter 4 to check the viscoelasticity contribution to our simulation results.

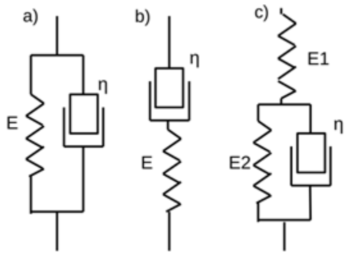

Figure 1.9: The three classical viscoelastic elements. (a) the Kelvin-voigt model, a spring and a damper in parallel. (b) the Maxwell model, a spring and a damper in series, (c) the three element model (delayed elasticity), a spring in series with a Kelvin-voigt element. Figure extracted from [Melcher et al., 2012]

Chapter 2

Experimental methods for mechanical characterization

The determination of nanomechanical properties of materials is an intensive topic of study in several fields of nanophysics, from surface and materials science to biology. It is also known that the mechanical behaviour of the surface of the materials depends strongly on their properties at nanoscale. For this reason, in the last decades several novel characterization techniques were developed with the intent to reach sub-micron resolution. Nano-indentation was the first approach to mechanical properties measurements on microscale and after on nanoscale; diamond sharp tips are employed as indenters, with a tip radius of few hundred nanometers. The typical modus operandi in nano-indentation is plastically deform the surface [Oliver and Pharr, 2004] and obtaining an image of the indented area by AFM or electron microscopy. In the last period, this kind of measurements was substituted by measuring the penetration depth as function of the applied load; along with information about the tip geometry, it is possible to avoid the AFM or electron microscopy measurements. Moreover, it is possible to obtain some information about the local Young modulus too [Oliver and Pharr, 1992]. Since the typical diameter of this kind of measurements can reach few microns, this technique is not suitable for raster mapping of mechanical properties but just for discrete sampling points.

In order to avoid these problems and obtain higher spatial resolution measuring elastic moduli, nano-indentation and force modulation system were combined, obtaining the so called nanoscale modulus mapping [Syed Asif et al., 2001, Zlotnikov et al., 2017]; with this technique the contact area achieved is less than a one equivalent to a tip radius of 20 nm. After this technique, other methods were studied in order to improve the speed of the measurements and the precision as the number of parameters obtainable from the same measurement.

With the invention of atomic force microscope (AFM) in 1986 by Binnig, Quate, and Gerber [Binnig and Quate, 1986], that opened a new era for surface science and nanotechnology, it started to be possible to study the surface mechanical properties of materials and contact forces with a higher sensibility and resolution thanks to a smaller contact area. By using force modulation techniques [Giessibl, 2003], investigation moved towards the improvement of sensitivity and spatial resolution thanks to the possibility to separate elastic signals from inelastic ones. Other techniques, such as contact resonance, ultrasonic force microsocopy [Yamanaka et al., 1999] or atomic force acoustic measurements [Rabe et al., 2002], use ultrasonic transducer to achieve the same goal. A wide overview of the different kind of techniques can be found in the next sections.

2.1 Non AFM methods

2.1.1 Indentation method

There are mainly two methods of indentation, macroindentation and nanoindentation, which differ in the load applied. Micro-indentation was introduced in 1900 by a Swedish researcher, J. A. Brinell, facing a problem with the material properties of the metal indenter, that was not hard enough for the materials he was studying introducing significant errors in the hardness evaluations. In order to fix this problem, Shore [Shore and Hadfield, 1918] introduced a spherical diamond indenter with obvious problems with the manufacturing of a perfectly hemispherical surface. In 1922, Smith and Sandland [Smith and Sandland, 1922] introduced the use of a square-based diamond pyramid indenter (Vickers test) allowing the evaluation of the hardness of almost all materials except diamond itself. For samples in the range down to mm^2, the Vickers test is one of the most common methods. For brittle materials or small samples, Knoop introduced an alternative and more suitable hardness test in 1939 [Knoop et al., 1939], employing a rhombohedral-shaped diamond indenter used at low loads.

With the increasing need for more accurate characterization, especially on thin films with nano-scale thickness, it was necessary to develop nanoindentation methods working with ultra-low load (nN). In 1992, Pharr and Oliver proposed to extrapolate hardness and elastic modulus from the curves of indentation load depending on displacement data [Oliver and Pharr, 2004]. The employed indenters were a sharp Berkovich triangular pyramid or a sphere [Pharr, 1998], allowing resolution of changes in indentation depth at the nanometre level. In this way, it was possible to study thin films with thickness lower than few hundreds nm with a contact area of less than 10% of the film thickness. One has to take in mind that even if the indentation depth is on the scale of nanometres, the lateral size is still of microns or hundreds of nanometres. This method is now used in many nano-indenters system in order to measure mechanical properties at the nanoscale, even if for soft matter materials gentler techniques are required [Vanlandingham et al., 1997].

The nanoindentation technique is ideal to measure local elastic and plastic properties of materials up to the sub-micron scale. In order to obtain a proper quantitative analysis, a large number of laterally separated indents are required making it a time-consuming process with also limited lateral resolution. Evaluating elastic and viscoelastic properties is a problem too, because of the induced plastic deformation by the indentation process that modifies the architecture of the materials, especially for composite samples.

2.1.2 Nanoindenter-based modulus mapping

Nanoindenter-based dynamic mechanical analysis (DMA) techniques are ideal to probe local plastic, elastic, and viscoelastic properties. They are also employed successfully to map the mechanical properties of complex composite structure varying from inorganic to organic and even biological structures.

Dynamic mechanical analysis principles Contrary to static tensile compression, bending test or indentation technique, in DMA a periodically varying or constant force is applied to the sample. The force is applied at different frequencies ω and the displacement of the tip is measured by dedicated sensing device. In this way, the force induces a periodically stress on the sample having amplitude σ_a:

$$\sigma = \sigma_a \sin(\omega t) \tag{2.1}$$

and the measured displacement permits to calculate the strain with amplitude ϵ_a:

$$\epsilon = \epsilon_a \sin(\omega t - \delta). \tag{2.2}$$

In case of pure elastic response, the phase shift will be null and the Young's modulus E, for a perpendicular applied force, can be extracted as:

$$E = \frac{\sigma_a}{\epsilon_a}. \tag{2.3}$$

In case of viscous relaxation of the material, a part of the strain energy is dissipated and phase shift of the mechanical response is not in phase. In this case the Young's modulus is complex and having form

$$E^* = E' + iE'' \tag{2.4}$$

with E' and E'' storage and loss modulus, respectively. From the ratio of the complex stress and strain, the complex modulus is obtained:

$$E^* = \frac{\sigma_a \, e^{i\omega t}}{\epsilon_a \, e^{i\omega t - \delta}} = \frac{\sigma_a}{\epsilon_a} e^{i\delta} \tag{2.5}$$

Expressing the stress-strain relationship by real quantities, we obtain the expression

$$\sigma = E'\epsilon + \frac{E''}{\omega}\frac{d\epsilon}{dt} \tag{2.6}$$

where the first term represents the elastic response and the second term represents the viscous one.

DMA method was integrated in many techniques, mainly to characterize mechanical properties of significantly viscoelastic materials e.g. polymers. Time dependent behaviour can be extracted varying the frequency of the applied force or, keeping the frequency constant, is possible to measure temperature depending properties. The idea to use force modulation in order to separate storage and loss moduli was applied to nanoindenter-based techniques and also to AFM-based ones.

Experimental set-up The typical experimental set-up for modulus mapping (figure 2.1a) is composed by a nano-indenter equipped with a piezo-scanner, a lock-in amplifier, and a force modulation system. The nano-indenter tip apply a static force F_{DC} towards the sample's surface penetrating elastically only few nanometres avoiding plastically deformation. In addition, F_{DC} is modulated with a force F_{AC} having smaller amplitude. The sample's area is scanned by the piezo-scanner and, thanks to this force, the topography of the surface is obtained. Monitoring the tip displacement U (green curve in figure 2.1b), its amplitude U_0 and phase shiftδ relative to the exciting modulating signal, it's possible to calculate the local storage and loss moduli. Additionally, 2D images of elastic and viscoelastic properties are obtainable.

Theory In order to obtain the mechanical properties of the studied material by the lock-in amplifier signal, theoretical considerations have to be taken in consideration [Syed Asif et al., 2001, Zlotnikov et al., 2014, Ganor and Shilo, 2006]. The tip displacement U is described by the following differential equation:

$$m\ddot{U} + C\ddot{U} + KU = F_{AC} \, e^{i\omega t}, \tag{2.7}$$

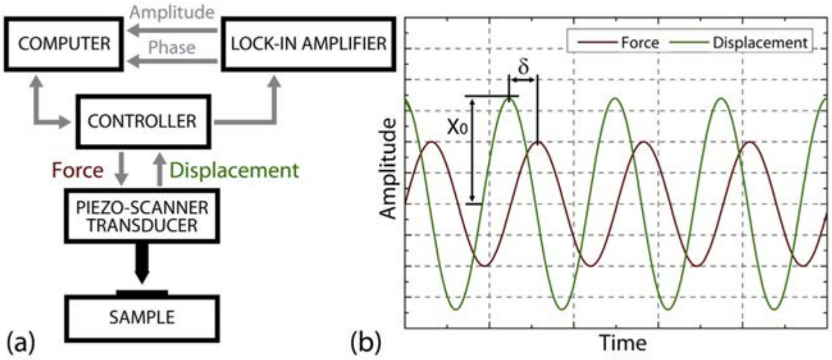

Figure 2.1: (a) Schematics of the nano-indentation based modulus mapping set-up. (b) Rapresentation of the modulated force $F_{DC} + F_{AC}$ and of the displacement signal. Figure extracted from [Zlotnikov et al., 2017]

.

where m is the mass, C is the effective damping coefficient, and K is the effective stiffness of the sample-tip system. The solution of the motion equation is the periodic displacement:

$$U = U_0 \, e^{i\omega t - \delta}. \tag{2.8}$$

From equations 2.7 and 2.8, we can find the amplitude U_0 and the phase shift δ:

$$U_0 = \left| \frac{F_{AC} \, e^{i\delta}}{K - m\omega^2 + i\omega C} \right| = \frac{F_{AC}}{\sqrt{(K - \omega^2)^2 + \omega^2 C^2}} \tag{2.9}$$

$$\delta = \tan^{-1} \left(\frac{\omega C}{K - m\omega^2} \right) \tag{2.10}$$

The contact stiffness K^*, defined as the load divided by the displacement, is a complex quantity:

$$K^* = K' + iK'' = F_{AC} \, e^{i\omega t - \delta} = K - m\omega^2 + i\omega C \tag{2.11}$$

with the real part related to the storage stiffness (in phase with the applied force) and the imaginary one (90 deg-phase shift with respect to the applied force) related to the loss stiffness. The stiffness K and the damping coefficient C can be related to the measured parameter K^* and δ with these relations:

$$K = | K^* | \cos(\delta) + m\omega^2; \qquad C = | K^* | \sin(\delta)/\omega \tag{2.12}$$

By a Kelvin-Voigt mechanical equivalent model, they can be decoupled in sample and indenter contributions to the measured storage and loss stiffness:

$$K = K_s + K_i \qquad C = C_s + C_i \tag{2.13}$$

where K_i and C_i are the stiffness and damping coefficient of the tip when not in contact with the surface, respectively. In the same way is possible to relate the complex Young's Modulus ($E = E' + iE''$) to the local storage stiffness K_S and loss stiffness ωC_S. Using the Hertz contact mechanics, the storage and loss moduli have the following form, respectively:

$$E' = \frac{K_S}{2}\sqrt{\frac{\pi}{A_C}}; \qquad E'' = \frac{\omega C_S}{2}\sqrt{\frac{\pi}{A_C}}, \tag{2.14}$$

where A_C is the contact area between the indenter and the sample surface. From the showed formulas, the indenter's physical and geometric parameters (C_i, K_i, m and A_C) are necessary for the quantitative extrapolation of the sample's mechanical properties. Therefore a indenter tip calibration is necessary in order to obtain quantitative results. This technique is used to characterize and map elastic moduli in composite structures [Syed Asif et al., 2001, Ganor and Shilo, 2006] and natural composite materials as teeth [Balooch et al., 2004], bones [Balooch et al., 2005] and silk [Ebenstein and Wahl, 2006] with successful results.

2.2 AFM methods

AFM principles

The AFM scans the surface using a sharp probe, typically pyramidal, with height of 10 µm to 20 µm and radius r_{tip} having values starting from 2 nm (super sharp) up to 50 nm (diamond or coated tip). The probe is located at the end of a cantilever with length of hundred microns, width of few tens microns and thickness of few microns and is moved across the surface of the sample. A laser beam hits the cantilever on the opposite site of the position where the tip is situated and the reflected beam is collected by a four-segmented photo-diode: the cantilever vertical deflection is detected through the difference of signal measured by the two upper and two lower segments, whereas the difference between the signal measured by the two right and two left segments gives the cantilever torsion signal, as shown in figure 2.2a. The tip is moved across the sample surface and its deflection and/or torsion are monitored at each point of the surface and used as input signal for the feedback loop signal. The basic AFM operation modes are the contact mode (CM), the intermittent (ICM) or tapping mode, and the non contact mode (NCM). Each of these modes work in different regions of the interaction force and at different distance from the surface as shown in figure 2.2b. In contact mode, the tip and the sample surface are in close contact, in the regime where the tip-sample force is completely repulsive, and the feedback signal consists in the cantilever static deflection. By monitoring the cantilever static deflection, it is also controlling how much the tip pushes against the surface and therefore how

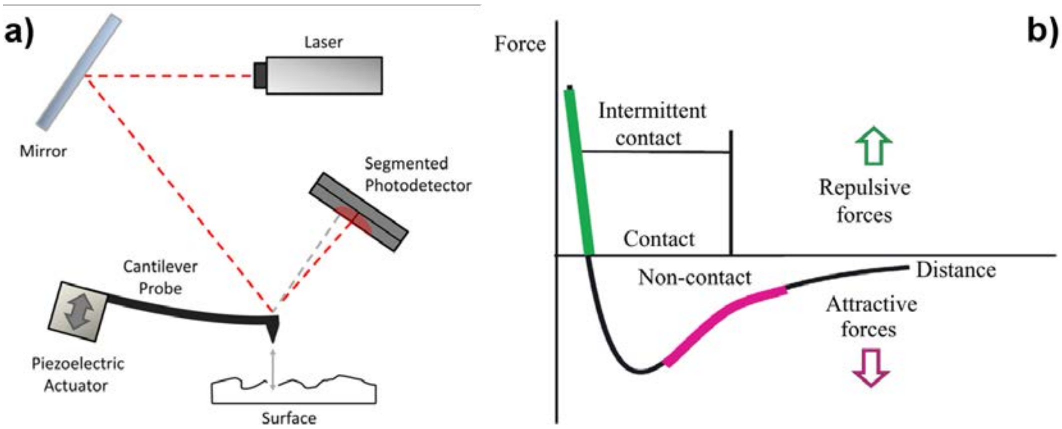

Figure 2.2: (a) Schematics of typical AFM configuration of cantilever and optical lever detection [Parker and Dick, 2012]. (b) Lennard-Jones (subsection 1.1.1) representation of interaction forces as a function of the tip-sample separation. When the tip approaches the sample surface, transition in the interaction force occurs from attractive due to the van der Waals attraction to the repulsive due to the repulsion of electron clouds of the nearest atoms on the tip apex and the sample surface [Hussain et al., 2017]

.

the tip-sample interaction can be gentler or more invasive. Another possibility is making to maintain the probe at a fixed height above the sample, disabling the feedback control. This mode is typically used in atomic resolution AFM and has the advantage to obtain a high scanning speed but at the same time samples has to be sufficiently smooth in order to avoid damages. Being the tip in close contact with the surface, CM is a technique very sensitive to friction and adhesion phenomena. For that reason, lateral force mode AFM was implemented to study these phenomena. In lateral force mode, the imaging is performed as in contact mode except the scanning motion is perpendicular to the axis of the cantilever. In this way, friction and adhesion can be measured by the torsional deflection of the cantilever.

The most common intermittent mode technique is the amplitude modulation AFM (AM-AFM mode), where an actuator (mechanic, magnetic or piezo) excite the cantilever around its resonance frequency; the feedback signal consists in cantilever oscillation amplitude. In both modes, the feedback loop maintains the feedback signal (set point value) constant during the scanning by raising or lowering the cantilever or the sample with a piezo transducer in the vertical direction. In this way the distance of the tip from the surface increases or decreases, respectively. The cantilever vertical displacement at each point of the scanning gives the local height variation of the surface reflecting the sample topography. Depending on the application, Intermittent contact or tapping mode is usually preferred to contact mode because the contact between tip and sample surface is shorter in the first case than in the second, reducing the possibility of damaging or contaminating tip and sample surface. Moreover, this technique provides information on surface mechanical properties from the phase signal which reports the oscillation phase difference between the response of the cantilever when not interacting with the surface and when engaged with it. The image generated from the phase signal gives information about mechanical properties of the surface and energy dissipation by the contrast or the difference of phase value showed between the different areas [Tamayo and Garcia, 1996]. Important factor to take in account is that the phase shift is influenced by other factors such as set point value or tapping frequency, that depends in a totally not straightforward way on the tip-surface interaction and tip height [Bar et al., 1997,San Paulo and Garcia, 2001].

In NCM-AFM (attractive region in figure 2.2b), the tip does not enter in contact with the surface and the cantilever oscillates at its resonance frequency (frequency modulation) or next to it (amplitude modulation). In frequency modulation (FM-AFM), a phase-locked loop is used to control the cantilever's oscillation frequency and keep the cantilever vibrating at its resonance frequency with a constant amplitude. The spatial dependence of the cantilever's frequency shift, induced by the tip-sample interaction, is used as the source of contrast: during the scan, the tip-sample distance is varied in order to achieve a set value for Δf. For that, the topography in the images represents a map of constant frequency shift over the surface that can provide information about tip-sample interaction. Because of the distance between tip and sample, this mode does not suffer from tip or sample degradation effects. This characteristic makes NCM-AFM ideal for measurement on soft samples such as biological or organic samples. Moreover, frequency can be measured with very high sensitivity and this fact allows the utilization of stiff cantilevers that provide more stability close to the surface. This stability lead to obtain a better resolution as shown in the first true atomic resolution image in ultra-high vacuum conditions [Giessibl, 2003]. However, because of the non-contact between tip and surface, the imaging is more sensitive to adsorbed fluid on the surface that could affect the surface image. Amplitude modulation in NC mode has the same characteristics as in IC, but with the same advantages and disadvantages due to the distance between tip and sample's surface mentioned for the frequency modulation mode.

However, the main techniques used for nano-mechanical characterization are described in the next sections of this chapter.

2.2.1 Quasi-static measurements of mechanical properties by AFM

The first work on nanomechanical properties using AFM as a probe was performed by Colton and Burham in 1989 [Burnham and Colton, 1989]. Years later, Brushan and Kionkar demonstrated that nanoindentation performed by AFM has the advantage of high spatial resolution together with a indentation depth of few nanometres [Bhushan and Koinkar, 1994]. The versatility of AFM-based methods was demonstrated by many studies on various types of surfaces,going from soft matter and biological samples to hard surfaces [Chyasnavichyus et al., 2015, McConney et al., 2010], not just for mechanical characterization but for many different physical (i.e. electric or magnetic) properties. The nanometre lateral resolution, achievable with sharp tips, has induced the development of several techniques focused on obtaining qualitative and quantitative mapping with simultaneously imaging or reconstruction of the sample surface. As mentioned above, the possibility of exerting loads down to nano-newtons or even pico-newtons, permits to probe thin and ultra thin films of compliant materials such as polymers.

Quasi-static indentation

In this technique force curves are performed. It means that the cantilever tip is made to approach to the surface and, once in contact, it is retracted. During both the approaching and retracting phases, the cantilever deflection u is monitored and the tip-sample separation distance d is controlled. By calibrating the cantilever spring constant k_c, and relating u to the force exerted by the tip to the surface ($F = k_c u$), it is possible to transform these curves in a force-distance curve that provides information about several properties of the materials [Cappella and Dietler, 1999, Butt et al., 2005]. Once the tip is in contact with the surface, on a stiff material any variation of ΔZ produces a variation in u proportional to k_c. Instead on a compliant material, a reduction of ΔZ produces an increase in u but also make the

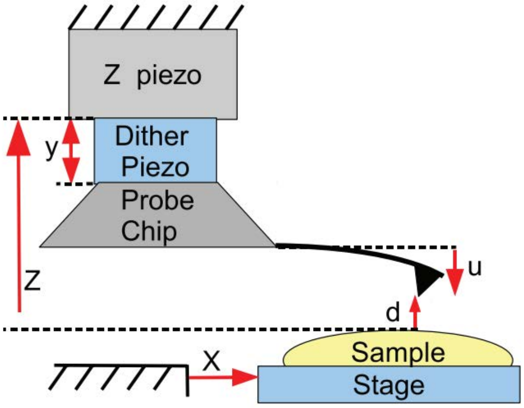

Figure 2.3: Schematic of the coordinates used in cantilever dynamic modeling. FIgure extracted from [Kiracofe et al., 2012].

tip penetrate into the surface (indentation). The penetration depth δ is related to the curve parameters ΔZ and u: in this way from the curve $u(\Delta Z)$, it is possible to obtain the curves $u(\delta)$ and $F(\delta)$ [Weisenhorn et al., 1993]. An example of a force-tip position curve is shown in figure 2.4. $F(\delta)$ and $F(\Delta Z)$ curves can be used to

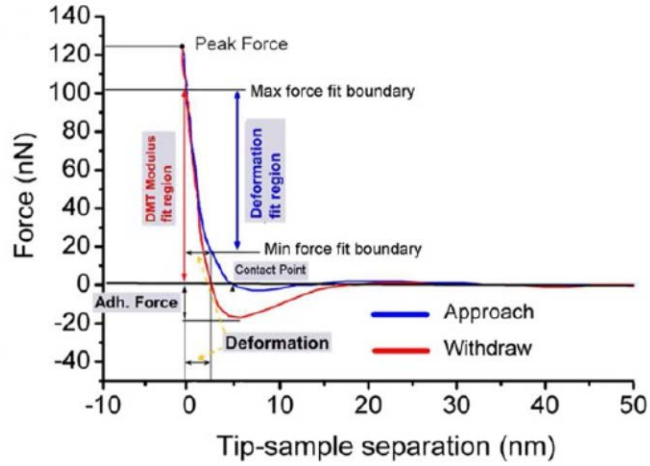

Figure 2.4: Example of Force vs distance curve. In the image the mechanical properties deducible from the force-distance curve applying a mechanical model (in this case the DMT) are hightlighted. Figure extracted from [Lorenzoni et al., 2015b]

.

extrapolate the mechanical properties of the surface. In fact, the slope of $F(\delta)$ at the onset of the unloading curve corresponds to the tip-sample contact stiffness K^* that can be evaluated by the relation:

$$K^* = 2aE^*, \tag{2.15}$$

where a is the tip-sample contact radius and E^* is the reduced Young's modulus, as defined in equation 1.35. The term related to the sample surface in E^* can be determined by the unloading curve using suitable contact mechanics model such as the DMT model. Several parameters can be obtained by this kind of technique such as the hardness, the peak force, tip-sample adhesion and the dissipated energy.

The merits of this kind of technique is the possibility of exert ultra low loads (pN) and reach low indentation depths down to few nanometres. This factors allow the mechanical characterization of thin films also on stiff substrates. The employment of cantilever with different spring constant value allows penetration depths from few to several hundreds nanometres, giving the possibility to investigate the mechanical properties of surfaces and bulk too. The drawbacks of this kind of measurements are the difficulties of describing the tip geometry, its effective shape and especially its curvature radius. All these parameters produce large uncertainties in the determination of the elastic modulus. In addition, the possible non-linearity and hysteresis of the piezo transducer and the inclination of the cantilever have to be taken in account. All these problems can be partially resolved with an efficient calibration method, as described in subsection 2.2.3.

Force-volume mode AFM

Taking advance of the AFM accuracy with regard to the in-plane positioning and the scanning capabilities, it is possible to acquire two-dimensional arrays of quasi-static curves. In this way maps of the tip-sample contact stiffness are collected and transformed into quantitative elastic modulus maps. The drawbacks and advantages of this technique are the same as for the quasi-static indentation. Additional drawbacks are the limited lateral resolution and the long time necessary to obtain a complete map.

2.2.2 Dynamic measurements of mechanical properties by AFM

Begun to be developed in the first years of 1990, these methods exploit the idea that the resonance frequency of the vibrating cantilever tip depends on the elastic properties of the investigated sample surface.

Single-frequency techniques

Force modulation microscopy Force modulation microscopy (FMM) was the first CM dynamic technique developed for the study of surfaces mechanical properties [Maivald et al., 1991]. It is based on the monitoring of the deflection signal of a stiff cantilever maintained at a constant deflection during the scan. In this way, it is possible to obtain a topographical image. In addition, a small sinusoidal displacement is generated at the base of the cantilever or directly applied to the sample. The frequency of this displacement is between few to hundreds of kHz, which is much faster than the time constant of the instruments of the feedback loop and below the resonance frequency of the system cantilever-surface. Therefore, the topographical measure is not affected. Applying this displacement to the cantilever in contact with the surface (or the contrary in case that the displacement is applied to the sample), the tip indent the surface and higher is the amplitude of the cantilever deflection, less compliant is the sample surface. Measuring the dynamic deflection of the cantilever and the difference between it and the applied dynamic amplitude, it is possible to obtain a map of the stiffness. The map of the measured stiffness is convertible in to the elastic modulus using a contact mechanics model.

Compared to other static techniques, FMM take advantage of the use of the lock-in amplifier, allowing the detection of low signals with high signal-to-noise ratios. Moreover, the hardware and software are the same of a standard AFM for ICM operations so the implementation is easy and consist just in a lock-in amplifier and a piezo-actuator. This technique in unsuitable for stiff surfaces because the cantilever spring constant can be not high enough and the cantilever is more easily deflected than the surface indented. Too soft materials are also not suitable for this technique due to the necessity of a continuous contact that can damage or modify the surface. There is also a lack of theoretical models for interpreting dynamic indentation for viscoelastic materials in case of small amplitude oscillations and contact dimensions comparable with the film thickness [McGuiggan and Yarusso, 2004]. Anyway, using really stiff cantilever and applying loads of hundreds of micronewtons it is possible to characterize the loss and storage moduli but damaging the sample and reducing the quality of the imaging capability.

Contact resonance techniques Contact resonance AFM (CR-AFM) can be considered an evolution of FMM. This technique was developed in the 1990's by the Yamanaka and Arnold groups [Yamanaka et al., 1994,Rabe and Arnold, 1994]. Taking in account the system constituted by the AFM cantilever in contact with the sample surface, the basic principle is that the contact resonance frequency and the quality factor (Q) of this system changes in response to the variations of tip-sample stiffness and damping (see figure 2.5). As in the FMM, the vertical distance tip-sample is modulated by a very small vertical amplitude. If the vertical modulation is applied to the cantilever, the method is called Ultrasonic Force Microscopy (UFM). If the vertical modulation is applied to the sample, it is called also Atomic Force Acoustic Microscopy (AFAM). In both cases, the cantilever response is detected in order to measure the contact resonance. First versions of this technique operated at a single frequency and measured the amplitude deflection of the cantilever near the contact resonance. The contrast obtained in the images depends on the elastic and dissipative interactions and directly to the stiffness, but only qualitatively. In fact,

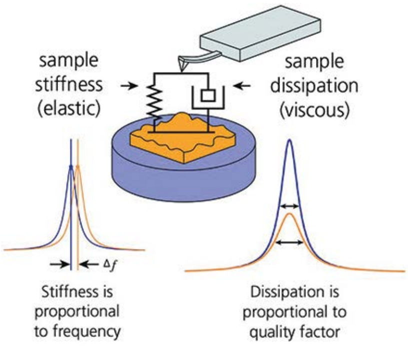

Figure 2.5: Schematics of tip-sample system in CR-AFM. Figure extracted from [Ohler and Kocun, 2013]

.

working near the contact resonance, the contrast can be inverted whether the working frequency is above or below the contact resonance [Rabe et al., 2002]. A way to fix this problem was to directly track the resonance frequency by a phase-locked loop lock-in (PLL), but spurious phase shifts make the tracking stability difficult. One solution can be to perform a frequency sweep around the resonance frequency; in this way the quality of the signal improves but the acquisition speed decrease drastically. Novel multi-frequency strategies try to fix these problems without affecting the scan speed, for example working at two frequencies around the resonance one permits to avoid more easily the inversion of contrast without perform the frequency sweep [Ohler and Kocun, 2013]. As in most of the mechanical characterization techniques, one of the major problems are the analytical model that are incomplete or not straightforward even in case of the simplest cases. Moreover, the continuous contact may damage soft samples or the tip in case of stiff materials.

Pulsed-force In pulsed-force AFM (PF-AFM), the tip-sample separation d is modulated by a sinusoidal signal at a frequency well below the fundamental resonance frequency of the cantilever. The amplitude is adjusted in order to make the cantilever jumping in and out of contact during each cycle [Rosa-Zeiser et al., 1997]. In this way, the cantilever performs a periodic indentation of the sample surface; its deflection signal is analysed obtaining approaching and retracting $F(d)$ curves. This technique is considerably faster than the force-volume AFM and permits to scan the sample and acquire the topography maintaining a constant value of the maximum force applied to the surface. The latest improvement in data acquisition and processing data allow to storage and analyse whole force-distance curves at each point of the scanned area [Young et al., 2011] obtaining simultaneously maps of topography, elastic modulus, maximum deformation, adhesion and dissipation. These physical quantities are obtained fitting the force-distance curves with a contact mechanical model, but it has to be taken to account that all these quantities extracted are not completely independent and viscoelasticity is not considered. This recently improved technique is more often referred to as $Peakforce^{TM}$ quantitative nanomechanical analysis and use the DMT model to extrapolate the mechanical parameters of the surface.

The advantages of this technique are the relative high speed and high resolution obtainable with no specific cantilevers and the possibility to control the tip-sample interaction permitting to work also on soft materials. The measurements can be performed both in air and in liquid. Some drawbacks are that the spring constant of the cantilever should match the sample stiffness and that this technique require a calibration procedure on samples with known elastic modulus in order to set the parameters (for example the tip radius which is unknown) and make the extrapolated elastic modulus value coincide with the one of the calibration sample. This fact make the results subject to eventual changes in the elastic modulus of the calibration sample due to its deterioration.

Phase imaging This technique consists in the interpretation of the phase image obtained during a AM-AFM scan of the sample surface. During an AM-AFM scan, as we already explained, the cantilever oscillation amplitude is monitored and used as feedback. The phase shift ϕ between the cantilever oscillation and the excitation signal is detected and recorded as an image. The interpretation of phase signal is not straightforward: theoretical and experimental studies affirm that the ϕ signal can be expressed as the sum of an elastic properties term and a dissipated energy term [Cleveland et al., 1998]. Because the cantilever oscillation amplitude is kept constant (set point), the term that contribute to the contrast in the obtained image is just the dissipated energy one [Tamayo and Garcia, 1996, Garcia and San Paulo, 1999, San Paulo and Garcia, 2002]. It has to be said that this technique, is the most used one for every kind of materials, both in air and in liquid. In fact the phase image is obtainable just with a scan in tapping mode AFM. Despite many theoretical and experimental works, it is still a challenge to extract quantitative information because of its dependency on many factors such as instrumental parameters, tip shape changes and also environmental changes during the image. Moreover, in bistable working condition [San Paulo and Garcia, 2002] (i.e. when the tip is at the limit between attractive and repulsive regime) inversion in the phase contrast can be observed complicating the interpretation.

Multi-frequency techniques

In the last years, the necessity to expand the possibilities of the AFM started to be stronger. The lack of sensitivity to underlying structures or the difficulties distinguishing between elastic from non-conservative components in force measurements, pushed the AFM scientific community to expand their vision about this group of techniques. The main idea is that all the information about the properties of a sample is enclosed in the tip's motion and therefore, due to the highly nonlinearity of the cantilever dynamics, the harmonics and eigenmodes components are part of the tip's motion and contain part of that information that is lost because it is not monitored. Multifrequency AFM methods take inspiration from this concept and consist in exciting and/or detect more than one higher harmonics of the oscillation or eigenmodes of the cantilever.

Theoretical basis The highly nonlinearity of cantilever dynamics is due to the oscillation magnitude ($>5\,\mathrm{nm}$) higher than the decay lengths of the interaction forces ($<1\,\mathrm{nm}$) [Raman et al., 2008, Stark, 2010]. Moreover, it is known that the oscillation of the cantilever is thinkable as constituted by several frequency com-

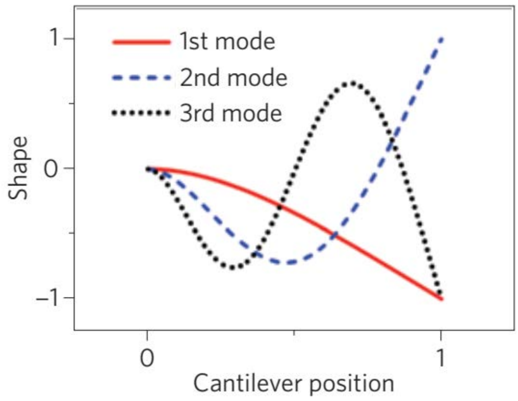

Figure 2.6: Modal shapes of the first three flexural eigenmodes of a rectangular tip-less cantilever vincualted only at one end. Extracted from [Garcia and Herruzo, 2012]

.

ponents [Butt and Jaschke, 1995, Stark and Heckl, 2000]. Anyway, the sensitivity of these components to the material properties has been neglected because of their amplitude several order smaller than the fundamental one [Stark and Heckl, 2000, Rodriguez and Garcia, 2002], except in case of applied large tip-surface forces, that it is not appropriate for high resolution imaging [Stark and Heckl, 2000]. So the difficulties to exploit this kind of signal are many: the low amplitude needs an instrumentation with high signal-to-noise ratio or technologies in order to enhance them; once being able to detect them properly, a theory to interpret these components is still missing.

The cantilever is a vibrating mechanical system characterized by its eigenmodes (flexural or normal modes) [Rabe et al., 1996, Rodriguez and Garcia, 2002, Melcher et al., 2007]: the eigenmodes, see figure 2.6, are describable by the effective stiffness k_j, the resonant frequency ω_j, the quality factor Q_j and the optical sensitivity σ_j. The relationship among these parameters, for a rectangular cantilever without tip, are reported in the table [Garcia and Herruzo, 2012] below.

Eigenmode	k_j	Frequency	Force constant	Quality factor	Optical senstivity
j		$\omega_j = \left(\frac{k_j}{k_1}\right)^2 \omega_1$	$k_j = \left(\frac{\omega_j}{\omega_1}\right)^2 k_1$	$Q_j = \frac{\omega_j}{\omega_1} Q_1$	$\sigma_j = \frac{\phi_j}{\phi_1}\sigma_1$
1	1.875	$\omega_1 = \omega_0$	k_1	Q_1	σ_1
2	4.694	$6.27\omega_0$	$39.31\, k_1$	$6.27\, Q_1$	$3.473\sigma_1$
3	7.855	$17.55\omega_0$	$308\, k_1$	$17.55\, Q_1$	$5.706\sigma_1$
4	10.996	$34.39\omega_0$	$1183\, k_1$	$34.39\, Q_1$	$7.985\sigma_1$

The reported relationship are approximated, in fact the mass of the tip, the non uniformity of the cantilever and other factors could introduce significant changes [Melcher et al., 2007, Kiracofe and Raman, 2010] that could limit the validity of the employed analytical expressions.

The non-linearities in the interaction force introduces,in the cantilever motion, higher harmonic components with a frequency equal to an integer multiple of the excitation frequency ($n\omega$). The spectra composed by these components contains information about the tip-surface force. In AM-AFM, the amplitude of the higher harmonics has this form [Dürig, 2000]:

$$A_n = S\frac{\omega_0}{k}\sqrt{|\left(\int_2^T F_{ts}(d)\cos(n\omega t)\,dt\right)|^2 + |\left(\int_2^T F_{ts}(d)\sin(n\omega t)\,dt\right)|^2} \quad (2.16)$$

where $S = 1/(\pi n^2)$ and $n > 3$, T is the period of oscillation and d is the instantaneous tip-sample distance. The amplitude of the higher harmonics is really small, decreases with the order as $1/n^2$ and is proportional to the higher force gradients [Hembacher et al., 2004, Wright and Solares, 2011] (more details can be found in section 4). Whenever a higher harmonic has its frequency close to the one of an eigenmode, it acts as an effective driving force exciting the vibration of that higher eigenmode of the cantilever [Stark et al., 2004] leading to an increasing of the higher harmonic amplitudes too. Consequently, the frequency spectra is modulated by the eigenmodes presence, as shown in fig 2.7. For example, in a rectangular cantilever, the frequency of the second eigenmode is $6.27\omega_0$ and it is really close to the frequency ($6\omega_0$) of the sixth higher harmonic as such as the third eigenmode that has its frequency takes place next to the seventeenth eigenmode. In order to enhance the amplitude and the number of the higher harmonics, special cantilevers have been studied [Sahin et al., 2004a, Sarioglu and Solgaard, 2011]. Among these new kind of cantilevers, the development of a torsional harmonic one has permitted

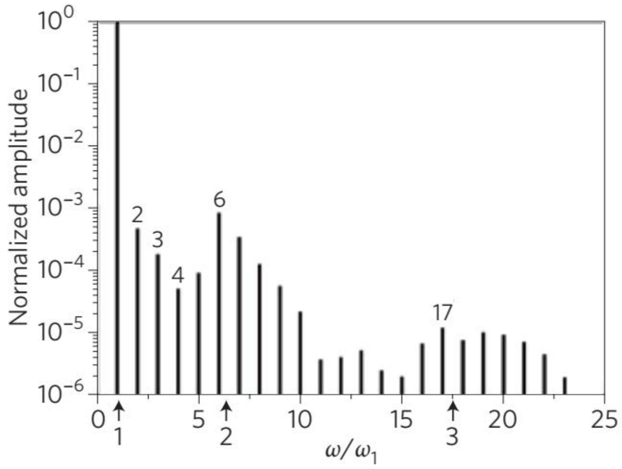

Figure 2.7: Simulation of the amplitude of the higher harmonics of a rectangular cantilever subject to non-linear force. The enhancement of the 6^{th} and 17^{th} harmonics is observable due to the coupling with the 2^{nd} and 3^{rd} eigennmode, respectively. Figure extracted from [Garcia and Herruzo, 2012]

.

the improvement of the signal-to-noise ratio of the higher harmonics [Sahin et al., 2007], see figure 2.8. Another strategy to enhance the amplitude is exciting several of them simultaneously, for example exciting the first two eigenmodes [Rodriguez and Garcia, 2004, Proksch, 2006], and then acquire the signal for each excited eigenmode [Lozano and Garcia, 2008]. Moreover, the excitation of two eigenmodes enhances the coupling with the nonlinear force, helping to increase the sensitivity of the second mode to material properties [Martínez et al., 2008]. From this approach, many techniques was studied exciting several eigenmodes and monitoring more than one higher harmonic; however, it has always to be taken in account that the higher the eigenmode the lower is the sensitivity to the material properties.

Multi-harmonic AFM imaging This technique consists in monitoring the higher harmonic components generated during a conventional dynamic AFM measurement [Stark et al., 2000, Sahin et al., 2004b, Balantekin and Atalar, 2005, Gramazio et al., 2018]. The problems of low amplitude, already mentioned above, in case of low force exerted for high resolution images suggest the use of special cantilevers [Sahin et al., 2004a] designed in order to enhance the higher harmonics signal. This technique has accomplished to obtain images in liquid, where the higher harmonics are easier to detect, of a bacterial S-layer with a spatial resolution of 0.5 nm [Preiner et al., 2007]. Images of living bacterium with an enhanced contrast was obtained [Turner et al., 2009], and also nano-mapping of local stiffness and viscoelastic dissipation in living cells [Raman et al., 2011].

Bimodal AFM In this method, the cantilever is excited using two driving forces [Rodriguez and Garcia, 2004, Martinez et al., 2006] tuned to match with two of the flexural eigenmodes of the cantilever. The output signal of the first mode is used to obtain the topography, while the second one is used to measure changes in mechanical [Martinez et al., 2006], magnetic [Li et al., 2009] or electrical properties [Stark et al., 2007] of the surface. Bimodal AFM permits a straightforward approach to separate topography from other interactions that influence the tip motion.

Torsional harmonic AFM This approach is based on collecting the higher harmonics of the torsional signal [Sahin et al., 2007]. By a conventional AM-AFM topographic image, the tip-sample force is obtained by the integration of the higher harmonic of the torsional signal. This kind of method needs a specially designed cantilever where the tip is collocated outside the cantilever axis, as shown in figure 2.8. With this design, the torque around the axis of the cantilever is favoured enhancing the presence of a large number of higher harmonics. Calculating the time-varying force is possible to measure the local mechanical properties, such as the Young’s modulus [Dong et al., 2009].

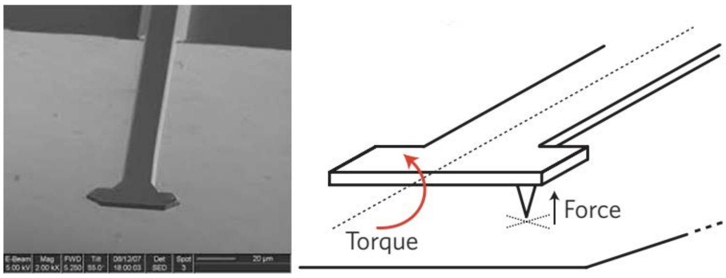

Figure 2.8: Scanning electron microscopy image and schematic of a torsional harmonics cantilever. Adapted from *"http : //www.rowland.harvard.edu/rjf/sahin/development/rev2/research.html"* .

2.2.3 Calibration methods

The major challenge in the study of material properties is quantifying. Without a good calibration and valuable methods, it can be difficult to obtain a rigorous uncertainty quantification and therefore be able to properly compare measurements between different instruments, groups or simulation results. In a typical AFM experiment, the main calibration parameters are: The X-Y-Z piezo-scanning stage; the sensor stage, i.e. the photodiode sensitivity or deflection sensitivity; the cantilever spring constant.

Scanning stage It is known that piezoelectric actuators are subject to non-linearity, hysteresis and deformation over time. all of these problems introduce non-ideal effect that affect the accuracy and the reproducibility of mapping. The procedure of calibration of Piezoelectric actuators consists in the scanning of standard calibrations samples that show a periodical geometry with known and precise dimensions. These calibration samples allow to check and fix any deviation of linearity, orthogonality and magnification in the x-y plane and calibrate the piezo elongation in the z plane.

Photodiode sensitivity The photodiode is the part that convert the laser spot signal in the cantilever deflection. In order to convert the voltage signal of the photodiode into the cantilever deflection in nm, it is necessary to calibrate the conversion coefficient namely photodiode or deflection sensitivity. The deflection sensitivity calibration consist in an approach curve on a stiff sample and calculating the derivative of the deflection vs piezo displacement in the region when it decreases. Another possible calibration method is by matching the termal oscillations of the cantilever with the cantilever spring constant. It has to take in account that the deflection sensitivity calculated in contact (static) mode is different from the one calculated in dynamic mode. For that, depending on which AFM mode it is used, the deflection sensitivity has to be calibrated statically or dynamically. Some theoretical approximations are available to convert the static deflection sensitivity in the dynamic one [Schäffer, 2005, Garcia, 2010].

Spring constant A reliable quantification of nano-mechanical properties requires a precise knowledge of the parameters of the cantilever in use, and the spring constant is one of most difficult to calibrate with precision. Once measured the cantilever deflection, that can be measured with accuracy up to sub-Angstrom sensitivity, it is necessary to determine the spring constant in order to convert the deflection in force units via Hooke's law. The nominal value reported by the manufacturers can vary largely. This is because the fabrication processes not assure to obtain cantilever with the same dimensions, especially thickness that varies from wafer to wafer or within the same wafer too [Albrecht et al., 1990, Tortonese, 1997]. This high incertitude is a problem in the case quantitative results are needed, for that many techniques have been proposed to calibrate the spring constant. These methods can be divided in three groups: i) dimensionless models [Albrecht et al., 1990, Butt et al., 1992, Sader and White, 1993, Cleveland and Bocek, 1993], where theoretical analysis or semi-empirical formulas which determine the spring constant by the dimensions of the cantilever and its material properties; ii) static deflection measurements [Senden and Ducker, 1994, Rabinovich and Yoon, 1994], where the spring constant is determined by loading the cantilever with a known static force (usually a calibration mass); and iii) dynamic deflection measurements, where the resonance behaviour of the cantilever is related to its spring constant. Of course, rectangular and V-shaped cantilever have different dynamic behaviour, and the calibration of the second one is more complex. The description of the current methods is focused on the dynamical deflection measurements applied to rectangular cantilever, because of interest for this study.

The dynamic deflection measurements category includes three of the most used calibration methods: the added mass method [Cleveland and Bocek, 1993], the thermal tune method [Hutter and Bechhoefer, 1993], and the Sader method [Sader et al., 1999].

Added mass method Also known as Cleveland method, it is based on adding a known mass, usually tungsten microspheres, to the cantilever and measure the resonance frequency shift due to the added mass M. In fact, the resonance frequency f_0 is related to the spring constant and the mass by the following formula:

$$f_0 = \frac{1}{2\pi}\sqrt{\frac{k_c}{M + m^*}}, \tag{2.17}$$

where m^* is the effective mass of the cantilever, a quantify proportional to the actual mass of the cantilever that for a rectangular one is $m^* = 0.24 m_b$ [Cleveland and

Bocek, 1993] (m_b is the mass of the beam). Rearranging the equation above:

$$M = \frac{k_c}{(2\pi f)^2 - m^*} \tag{2.18}$$

Adding several masses and measuring the new resonance frequency after each addition, the slope of the plot of M *vs* $1/(2\pi f)$ gives k_c. In the case of just an addition, the formula for k_c is

$$k = \frac{(2\pi)^2 M_1}{(1/f_1^2 - 1/f_0^2)} \tag{2.19}$$

where f_1 and M_1 are the frequency and mass with the added mass, and f_0 is the original frequency, i.e. without the added mass.

This method has the problem that it implies the manipulation of the cantilever, and that the position where the mass is applied is critical. Another source of error is the measurement of the mass that is mainly done by measuring its volume, assuming it spherical and constant density. Of course the particle are not perfectly spherical and this fact introduce an error.

Sader method Sader, among his several studies of cantilever calibration, has developed a technique for rectangular cantilevers where the required parameters are only the top view dimensions, the resonance frequency, quality factor Q, and the density and viscosity of the fluid in which the measurement is performed [Sader et al., 1999]. The requisites about the geometry of the cantilever is that $L >> w >> t$ (L is the lenght, w is the width, and t is the thickness), even if $L/w > 3$ has been found acceptable [Chon et al., 2000].

The Sader's expression for k_c is:

$$k_c = 7.5246 \rho_f w^2 L Q f_0^2 \Gamma_i(Re) \tag{2.20}$$

with

$$Re = \frac{2\pi \rho_f f_0 w^2}{4\eta_f} \tag{2.21}$$

where ρ_f is the density of the fluid in which the measurement is performed, η_f is the viscosity of that fluid, and Γ_i is the imaginary component of the hydrodynamic function depending on the Reinolds number Re.

The resonance frequency and the quality factor are measured by a power spectral density analysis of the oscillations of the cantilever thermally driven. The calculation of hydrodynamic function is more complicated, but an analitical expression can be found in Sader's work [Sader, 1998]. Even if mathematically complex, this method is experimentally easy to use. In fact, the resonant frequency and the quality factor can be measured accurately, while the cantilever dimensions can be obtained by optical microscope measurement. The limiting factor is the geometry of the cantilever which has to be rectangular and with the right ratio between its dimensions. Anyway the correction parameters for always more kind of commercial cantilevers have been measured and on the Sader's website is also possible to calibrate directly on line at the web page "https://sadermethod.org/" [Sader et al., 2016].

Thermal tune The thermal tune method is probably the most widely used method and has become a standard routine in many commercial AFM brand. The method is based on modeling the cantilever as a simple harmonic oscillator. Using the equipartition theorem, it is possible to relate the thermal motion of the fundamental eigenmode of the cantilever to its thermal energy, $k_B T$, via this formula:

$$k_c = \frac{k_B T}{\langle z_c^2 \rangle} \tag{2.22}$$

where k_b is the Boltzmann constant, T is the temperature and $\langle z_c^2 \rangle$ is the mean square displacement of the cantilever [Hutter and Bechhoefer, 1993]. $\langle z_c^2 \rangle$ is found by performing a power spectral density analysis of the cantilever oscillations and integrating the area under the peak of the fundamental eigenmode. It was realized that two important corrections were necessary. The first correction takes into account that the cantilever does not behave as an ideal spring: therefore, the energy of a simple harmonic oscillator is different from that of the cantilever [Butt and Jaschke, 1995]. The second correction takes into account that the cantilever displacement, as measured by the optical detection scheme, is different from the actual displacement of the cantilever because it is proportional to angular changes in the cantilever position, not its absolute deflection. These angular changes depend on the bending mode of the cantilever. Taking in account all these factors, the equation becomes [Ohler, 2007]

$$k_c = \frac{0.971 k_B T}{\chi^2 \langle z_c^2 \rangle} \tag{2.23}$$

with $\chi^2 = 1.09$ for a rectangular cantilever. The value of χ^2 changes with the type of cantilever.

The thermal tune method is a really attractive method because is simple and it is applicable to many kind of cantilevers. The only real limitation is related to the range of spring constant of the cantilever: in fact, it is more effective for relatively soft cantilevers ($k_c < 10N/m$) where the thermal noise is well above the noise floor of the deflection measurement and lead to an incertitude around 10% while the incertitude increases up to 20% or more for harder cantilever [Song et al., 2015].

Cantilever tilt angle contribution One more factor, that was not taken into account until recently, is the tilt of the cantilever. In fact, AFM cantilever are generally mounted at a slight angle from horizontal, typically about 12°. This is done in order to avoid the contact of the cantilever beam with the sample and make sure that only the tip is interacting with the sample. This tilt, if not considered and corrected [Heim et al., 2004, Hutter, 2005], can lead to errors in force measurements. The overestimation, due to the the tilt, is by a factor $\cos^2\alpha$, where α represents the tilt angle. Therefore, the effective spring constant is obtainable applying the following correction factor:

$$k_{eff} = \frac{k_c}{cos^2\alpha}. \tag{2.24}$$

It has to be taken into account, moreover, that this correction factor it's not necessary for the thermal tune methods while it is for the added mass and Sader's methods.

Another consideration to do is about the uncertainty obtained with each methods. As reported in a comparative by Ohler [Ohler, 2007], Sader's method obtained the less uncertainty (4%) followed by Thermal tune method (8%). The others method have a higher uncertainty, comprised between 9% and 30% of the added mass method due to the uncertainty on the particle diameter.

Tip radius The ideal tip should have a delta-function shape and be made of an infinitely stiff, durable and non-reactive material. In practice, the actual production processes can just assure a range of indetermination of the radius and shape. Furthermore, the cantilever tip is a really delicate part and at each contact can modify its shape and radius. Indeed, the tip is continuously modifying during a scan. One possibility is to characterize the shape, radius and height of the tip by scanning electron microscopy (SEM), but it requires the removal of the probe from the instrument and the coating of the tip if not conductive enough (altering the original shape). Moreover, the electron flux that interact with the tip modifies the tip. These factors make the process time consuming and difficult the utilization of the tip after the characterization. The ideal characterization methods should be carried out in situ and performed without taking the probe out of the AFM. For that, the main methods consider the scan of samples with well defined shapes, such as cylindrical nanostructure [Bushell et al., 2011, Bustamante et al., 1992]; nano-spheres of gold or polysterene [Odin et al., 1994, Vesenka et al., 1993]; holes or pillars arranged in grids [Griffith et al., 1991, Glasbey et al., 1994]; and structures with a shape as much as possible similar to a delta function spike [Jensen, 1993, Montelius and Tegenfeldt, 1993, Atamny and Baiker, 1995]. Once obtained the image of topography, the parameters are extrapolated by geometrical models and simulations. Anyway, all these methods imply the utilization of dedicated calibration samples that obligate to stop the on going experiments and switch to the calibration procedure.

Chapter 3

Experimental and Simulation Methods

3.1 Experimental Section

AFM experiments were performed with a Bruker ICON instrument hosted in a homemade controlled humidity environment with a Multimode V control electronics with a photodiode bandwith of 5 MHz. The amplitudes of the higher harmonics were registered using, initially, the internal lock-in amplifier, and in a second stage using an external lock-in: a SIGNAL RECOVERY Model 7280 Digital Signal Processing (DSP) dual phase, wide bandwidth. The external lock-in allowed the improvement of the signal to noise ratio reaching a sensitivity of up to 60 μV against the 100 μV with the lock-in integrated in the Multimode control. As it is shown in figure 3.1, the signal of cantilever vertical deflection was sent to the lock-in input (blue line), and the cantilever driving signal was sent to the lock-in as reference signal (light blue line). Then the amplitude output of lock-in was sent to the AFM controller as external input (yellow line), in order to obtain a map of the sample surface. Commercial rectangular cantilevers (Bruker)were used, mainly two types: the first one was the model OTESPA-R3 (rebranded Olympus AC160TS-R3) with nominal values of spring constant $k_c = 26\,\mathrm{N\,m^{-1}}$, resonance frequency $f_0 = 300\,\mathrm{MHz}$ and tip radius $R_t = (7 \div 10)nm$; the second model was the Bruker's TESP-SS, a super sharp probe with nominal values of $k_c = 42\,\mathrm{N\,m^{-1}}$, resonance frequency $f_0 = 3320\,\mathrm{MHz}$ and tip radius $R_t = 2\,\mathrm{nm}to5\,\mathrm{nm}$. The complete specifications, from the Bruker's website, are reported in the following table:

Model	$f_0(kHz)$			$k_c(N/m)$			Lenght (μm)			Width (μm)			$R_t(nm)$	
	Min.	Nom.	Max.	Min.	Nom.	Max.	Min.	Nom.	Max.	Min.	Nom.	Max	Nom.	Max.
OTESPA-R3	200	300	400	8.4	26	57	145	160	175	38	40	42	7	10
TESP-SS	230	320	410	20	42	80	110	125	140	25	30	35	2	5

for all experiments, the humidity was kept below 10%, introducing nitrogen in the noise insulating box in order to limit the surface water contribution as much as pos-

Figure 3.1: Schematic of the experimental set-up with the external lock-in: the blue line highlights the vertical deflection of the cantilever sent to the lock-in as signal input to filter. The reference signal of the lock-in is highlighted in light blue and consisted in the driven signal that excited the cantilever. The amplitude and phase signals in output from the lock-in were sent to the external input of the AFM controller in order to obtain a map of the scan.

sible. First of all, the laser spot was aligned in order to illuminate the tip position as better as possible, following the reccomandations in the Proksch study [Proksch et al., 2004]. The cantilever was left for at least 45 minutes thermalizing with the environment in order to make the calibration stabler: the calibration protocol consisted of obtaining the dynamic deflection sensitivity coefficient by performing a ramp in dynamic mode on a sapphire surface, taking care to make the tip interact with the surface as little as possible in order to not to modify the tip and increase its radius. The tip was made oscillating with an amplitude equal to the one needed for the experiment, or in case of a varying amplitude experiment, with an amplitude value in the middle of the amplitude range. Then the amplitude trigger threshold was set at a value between the $40\% - 30\%$ of the free one; the fit range to extrapolate the deflection sensitivity was taken around the 50% of the free amplitude value, as shown in figure 3.2. The typical deflection sensitivity values obtained were between $70\,\mathrm{N\,nm^{-1}} to 120\,\mathrm{N\,nm^{-1}}$, while the default one should be $100\,\mathrm{N\,nm^{-1}}$. Once the deflection sensitivity was obtained, the spring constant k_c was calibrated by thermal noise technique applying the Sader's correction factors for the specific cantilever [Sader et al., 2014]. The thermal noise procedure has been included in the Bruker's control software and the version used was 8.15r3sr8, which was used to determine the deflection sensitivity and the spring constant by the thermal tune technique.

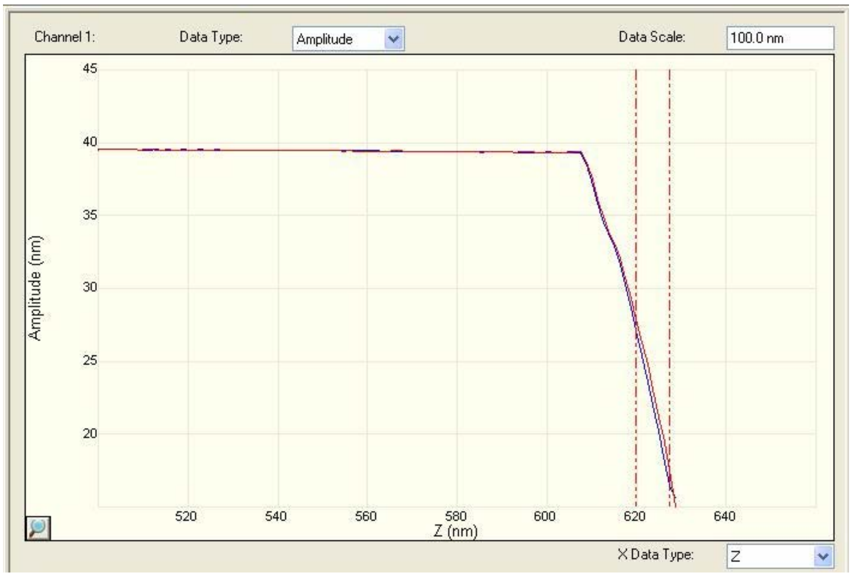
Channel 1:

Data Type: Amplitude

Data Scale: 100.0 nm

X Data Type: Z

Figure 3.2: Amplitude behaviour in a dynamic mode ramp for the deflection sensitivity calibration. the fit range is delimited by the two vertical red dashed line. In this case the free amplitude is 40 nm, the trigger threshold has been set to 15 nm and the fit range is 27 nmto17 nm

3.2 Computer Simulations: Virtual Environment for Dynamic AFM

Virtual Environment for Dynamic AFM (VEDA) is a suite of simulation tools developed by A. Raman and collaborators and freely available at the *www.nanohub.org* website. At the base of these simulations there is the development of a general multiple degree of freedom model for the description of the cantilever and its interaction with the sample. As described in [Kiracofe et al., 2012], the whole system is described by the following models: materials and tip-sample interaction; cantilever dynamics; lock-in amplifier and noise model; controller; numerical integration algorithms to solve the system equations; and a tip-sample geometry convolution model for the scanning tools.

The materials and tip-sample interaction models have been already described in subsection Contact mechanics and mechanical models. The cantilever dynamics is modeled as a multi-degree of freedom oscillator in order to be able to simulate multiple eigenmodes, necessary for multi-frequency techniques [Sahin et al., 2004a, Rodriguez and Garcia, 2004, Garcia and Herruzo, 2012]: the derivation of the model starts from the classical Euler-Bernoulli partial differential equation for small deflections of a rectangular cantilever bounded at one edge and subject to hydrodynamic damping force, driving force and tip-sample interaction force:

$$EI\frac{\partial^4 w(x,t)}{\partial x^4} + \rho_c A\frac{\partial^2 w(x,t)}{\partial x^2} = F_{hydro}(w) + F_{drive}(x,t) + F_{ts}(w(L,t)+Z)\delta(x-L), \tag{3.1}$$

where E is the cantilever Young modulus, I the moment of inertia, ρ_c density, A the cross-sectional area, w deflection, x axial coordinate, t time, F_{hydro} hydrodynamic force [Tung et al., 2008], F_{ts} tip-sample interaction force, F_{drive} driving force, L cantilever length, Z cantilever-sample separation and δ Dirac delta function 2.2. After having converted the hydrodynamic forces into an effective viscosity and added mass [Kiracofe and Raman, 2010], the equation is discretized in the base of the cantilever eigenmodes using the Galerkin's method [Meirovitch, 2001]. Basically, the cantilever's deflection w is written as $\sum_{i=1}^{\infty} q_i(t)\psi_i(x)$ with $\psi_i(x)$ the ith eigenmode shape and $q_i(t)$ the modal coordinates or more simply the tip deflection due to the ith eigenmode, as described in detail in [Melcher et al., 2007]. Obviously, the most indicated strategy to do should be taking in consideration as many eigenmodes as possible. However, VEDA allows consideration of up to $N = 9$. In this way, it is possible to reduce the original equation to a set of ordinary differential equations:

$$\frac{\ddot{q}_i}{\omega_i^2} + \frac{\dot{q}_i}{\omega_i Q_i} + q_i = \frac{F_{ts}(d)}{k_i} + \frac{F_i\cos(\Omega dt)}{k_i}, \quad i = 1....N \tag{3.2}$$

where ω_i stands for natural frequency, Q_i quality factor, k_i equivalent stiffness, F_i driving force of the ith eigenmode, $d = Z + \sum_{i=1}^{N} q_i$ tip-sample gap, and Ω_d the driving frequency that could be different from ω_i. The configuration of the coordinates used are shown in figure 2.3. After modeling the cantilever dynamics, the next step is modeling the optical beam deflection [Meyer and Amer, 1988] remembering that it measures slopes and not deflections. The observed deflection, assuming that the deflection sensitivity has been calibrated for the 1^{st} eigenmode, has the following form:

$$\tilde{u} = \sum_{i=1}^{N} \frac{\chi_i}{\chi_1} q_i \tag{3.3}$$

where χ_i is the slope at the end of the i^{th} cantilever's eigenmode. As explained before, the photodiode deflection sensitivity is typically calibrated by an F-Z curve or an approach ramp on a stiff surface, much harder than the sample surface on which the measurement has to be performed. Part of the cantilever dynamics is also the excitation force, which in VEDA arise an acoustic source (by piezo shaker), magnetic (by magnetic coating and generating an alternating magnetic field) and Lorentz force (by a conducting loop of metal and running an AC current through it exposing all the system to a steady magnetic field). For the acoustic driving force, which was the driving method used in the AFM used for this study, the expression of the force is the following:

$$F_j(\omega) = Y(\omega)\left\{\frac{\beta_j + \bar{m}}{\alpha_j + \bar{m}}\omega^2 - i\frac{\beta_j\omega_j}{\alpha_j Q_j}\omega\right\}, \tag{3.4}$$

where $m_c = \rho_c AL$ is the cantilever mass, m^* is the hydrodynamic added fluid mass and $\bar{m} = m_{tip}/(m_c + m^*)$ is the ratio of tip mass to total effective mass of the cantilever, $\beta_j = (1/L)\int_0^L \psi_j(x)dx$, $\alpha_j = (1/L)\int_0^L \psi_j^2(x)dx$, ψ_j is the j^{th} eigenmode shape, and $Y(\omega)$ is the Fourier transform of the base motion. Equation 3.4 is obtained by the general formula in liquid neglecting the fluid borne loading. The complete derivation can be found in [Kiracofe and Raman, 2011].

The latest version of VEDA (Version 2.1.12), also includes models to simulate real instrumentation and controllers: a phased-locked loop (PLL) and amplitude controller using proportional integral derivative (PID) feedback were implemented along with a complete model of the lock-in amplifier with a choice of several orders of filtering and adjustable constant time, which allow simulation of the effects of speed response, choice of lock-in amplifier, or of noise rejection and controller performance. Up to ten different lock-ins are available simultaneously to extract higher harmonics information.

All the VEDA tools include a variety of different tip-sample interaction models, including DMT, JKR, and Hertz, as well as capillary and viscoelastic forces. Furthermore, the simulated experiments can be performed in different environment: air,vacuum or liquid. The AFM simulated experiments under different conditions and environments [Kiracofe et al., 2012] are the following:

- **amplitude modulated approach curves and scanning**: a cantilever excited near its resonance frequency is simulated and, in the case of the approach curves, brought towards a sample surface. The assumption is that there are nonlinear interactions between tip and sample that affect the oscillations of the cantilever [Garcia and San Paulo, 1999, Berg and Briggs, 1997]. These nonlinear interactions are due to the interaction of attractive and repulsive forces and also to the detuning on the resonance frequency of the cantilever from the fixed excitation frequency when the tip starts to interact with the sample surface. Monitoring the cantilever's oscillations while approaching the sample surface allows information regarding the mechanical properties of the sample and interaction forces between tip and surface to be obtained [Lee et al., 2002]. The simulated system consists of a cantilever excited near its fundamental resonance frequency and moved towards the sample surface by the Z-piezo extension. In the case of scanning mode, the simulations include scans over specified geometry features also with different material properties.

Both kinds of simulation can also be performed by exciting the cantilever with multiple frequencies.

- **jump mode and single point tools**: jump mode is a mode in which a series of F-Z curves are performed in quick succession at each point of an image. The deflection is monitored and the curve is stopped when a certain threshold value has been reached. From the data of this series of F-Z curves, various parameters can be extrapolated, such as elasticity and adhesion force. Until now, only a single point can be simulated because a whole surface can not simulated. The single point tool does not compute the solution of the F-Z curve but just a single point. This allows analysis of the time histories for a certain Z value without simulating all the curve.

- **contact mode scanning**: contact mode is the first and simplest AFM imaging mode where the surface of the sample is scanned by a tip in contact with the surface. With this tool, it is possible to simulate the topography depending on the geometry of the tip

- **frequency sweep**: the nonlinear response of a driven cantilever, swept across a frequency interval next to the resonance frequency, is simulated when the tip interacts with the sample. It is possible to take into account more than one eigenmode or higher harmonic of the cantilever.

- **force - distance curves and force viewer**: the solutions of an unexcited cantilever, approaching and retracting from a sample surface, are solved. The assumptions for this kind of experiment are that, being undriven, the cantilever deflects just because of interactions between tip and sample, and that during the approach or retraction, the cantilever does not move laterally. Depending on the mechanical model, viscous forces can be included. The difference between the F-Z curve tool and the force viewer is that the F-Z curve tool simulates the cantilever dynamics, and therefore the regions where the cantilever snaps-in or pulls-off are not visible, while the the force viewer plots the entire F-Z curve independently from the cantilever dynamic. These tools are useful for studying bi-stabilities and the ”snap-in” and ”pull-off” phenomena.

- **frequency modulated curves and scanning**: in frequency modulation mode, the cantilever is excited at a frequency that is tuned to the nonlinear natural frequency through the use of a phase locked loop (PLL) and amplitude is maintained constant with an active feedback loop. The approach curve and scanning experiment are simulated in the same way as with the amplitude modulation mode, except for the control parameters of the PLL.

For the purpose of this thesis, the amplitude modulated approach curve tool was used. The main parameters for this kind of simulated experiment are the mechanical cantilever properties, the mechanical properties of the surface and the interaction forces coefficient depending on the utilized mechanical model. The parameters and their typical values or ranges for the performed simulations are as follows:

- Operating conditions & cantilever properties
  - Operating mode: approach
  - Excitation source: acoustic
  - Frequency scheme: single frequency
  - Number of eigenmodes: 2
  - Unconstrained amplitude (A_0): 20 nm to 100 nm
  - Cantilever stiffness k_i: 5 N m^{-1} to 50 N m^{-1}
  - Q factor: 400 to 600
  - Natural frequencies: 200 kHz to 400 kHz
  - Driving frequency: natural frequency
  - Tip mass: 0 (defined as fraction of cantilever mass, m_t=0 means that m_t=m_c)
  - Z approach velocity: 25 nm s^{-1}
  - Z range: $(A_0 + 10)$ nm to 0.1 nm
  - Lock-in filter order: none
  - Output type: photodiode with autocalculated slope
- Tip-Sample interaction properties
  - Tip-Sample interaction model: DMT
  - Tip radius: 2 nm to 50 nm
  - Young Modulus of the tip: 70 GPa
  - Poisson Ratio of the tip: 0.3 to 0.4
  - DMT calculation option: autocalculation Hamaker constant & intermolecular distance
  - Young Modulus of sample: 0.1 GPa to 350 GPa
  - Poisson Ratio of the sample: 0.3 to 0.4
- Simulation parameters
  - Number of point plotted: 1000
  - Accuracy vs speed trade off: standard speed/accuracy
  - Number of Higher Harmonic: 1
  - Choose Higher Harmonics: 6

In the Simulation parameters option, there is also the possibility to chose the output plots such as Fourier integral plots (in order to obtain amplitude and phase values not from the lock-in); root mean square amplitude value; amplitude and phase values of various eigenmodes and higher harmonics; mean and peak interaction forces; dissipated energy, and indentation and contact time. The software runs under linux and permits the launch of a batch of simulations defining the varying parameters. The typical output file contains a header, with all the simulation parameter values and chosen options, the results of the simulations and finally, a summary of the main parameters value. In the case of a batch, the result consists in a series of files, one for each simulation, with the same structure. The batch of output files was analysed by a home-made matlab script that reads the files, stores the needed outputs, and plots them. There is also the possibility of choosing the amplitude set point at which the higher harmonic amplitude value is desired to be monitored. The typical plots are shown in Figure 3.3 below: In the end, VEDA was chosen as simulator software for this study because of its several advantages: VEDA solves the differential equations of motion directly in time domain, making it slower but more accurate, able to simulate complex dynamics and interaction models that perturbation models cannot; it is a general simulator, this means that it is able to handle a wide variety of kind of experiments, as shown above, in different conditions and with the possibility to control numerous parameters; and finally it simulates also the response of the different higher harmonics and eigenmodes, that for this kind of study is quite fundamental.

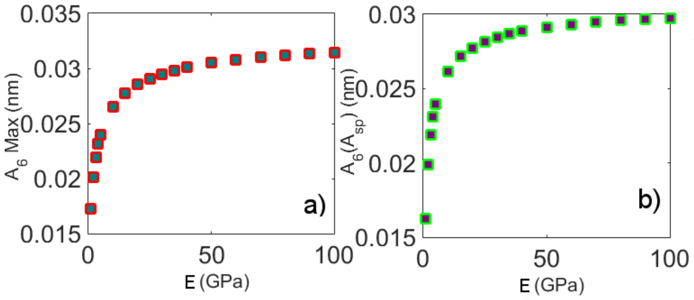

Figure 3.3: Typical plots from a batch of simulations performed with VEDA software and analysed by a Matlab script: a) dependence of maximum value of the 6^{th} higher harmonic amplitude (A_6), as a function of surface Young Modulus, b) dependance of A_6 at the amplitude set point (A_{sp}) equal to 50% of free amplitude.

For a detailed report about the results and discussion, we refer the readers to the relevant sections of Chapter 4 and Chapter 5.

Chapter 4

Functional dependence of resonant harmonics on nano-mechanical parameters in dynamic mode atomic force microscopy

Federico Gramazio[1], Matteo Lorenzoni[2], Francesc Pérez-Murano[2], Enrique Rull Trinidad[3], Urs Staufer[3] and Jordi Fraxedas[1]

1 Catalan Institute of Nanoscience and Nanotechnology (ICN2), CSIC and The Barcelona Institute of Science and Technology, Campus UAB, Bellaterra, 08193 Barcelona, Spain, **2** Instituto de Microelectrónica de Barcelona (IMB-CNM, CSIC), Campus UAB, 08193 Bellaterra, Barcelona, Spain and **3** Technical University of Delft, Mekelweg 2, 2628CD Delft, The Netherlands.

Keywords: atomic force microscopy; metrology; multifrequency; nanomechanics

4.1 Abstract

We present a combined theoretical and experimental study of the dependence of resonant higher harmonics of rectangular cantilevers of an atomic force microscope (AFM) as a function of relevant parameters such as the cantilever force constant, tip radius and free oscillation amplitude as well as the stiffness of the sample's surface. The simulations reveal a universal functional dependence of the amplitude of the 6^{th} harmonic (in resonance with the 2^{nd} flexural mode) on these parameters, which can be expressed in terms of a gun-shaped function. This analytical expression can be regarded as a practical tool for extracting qualitative information from AFM measurements and it can be extended to any resonant harmonics. The experi-

ments confirm the predicted dependence in the explored 3 N m^{-1} to 45 N m^{-1} force constant range and 2 GPa to 345 GPa sample's stiffness range. For force constants around 25 N m^{-1}, the amplitude of the 6th harmonic exhibits the largest sensitivity for ultra-sharp tips (tip radius below 10 nm) and polymers (Young's modulus below 20 GPa).

4.2 Introduction

When an AFM cantilever oscillating freely and harmonically at a given frequency f and amplitude A_1 approaches a solid surface, the oscillation becomes anharmonic due to the non-linear interaction, represented by the force field F_{ts}, between the cantilever tip and the surface [Garcia, 2010]. Thus, the time dependent trajectory $a(t)$ of the cantilever tip, which can be expressed in the harmonic limit by $a(t) = A_1 \cos(2\pi f t)$, is transformed into a Fourier series with harmonic oscillations of amplitudes A_n and frequencies $f_n = nf$ [Stark and Heckl, 2000, Garcia, 2002]:

$$a(t) = a + \sum_{n=1}^{\infty} A_n \cos(2\pi n f t) \tag{4.1}$$

where a is a constant amplitude value. The A_n coefficients can be analytically calculated, in the limit of weak tip–sample interaction ($A_1 >> A_n$ for $n > 1$), by integrating the force field F_{ts} that is modulated by weighted Chebyshev polynomials of the first kind, $T_n(u)$ [Dürig, 2000, Giessibl, 2006]. The simplified expression is:

$$A_n \cong \frac{2}{\pi k_c} \frac{1}{1-n^2} \int_{-1}^{1} F_{ts}(z + A_1 u) T_n(u) \frac{du}{\sqrt{1-u^2}} \tag{4.2}$$

where k_c stands for the cantilever stiffness, z is the distance between the cantilever base and the sample surface and $T_n(u) = \cos(n \cos^{-1}(u))$. Note that$A_n$ decreases for increasing order number (n) and k_c values. The tip-surface interaction F_{ts} can be expressed as a function of experimental parameters, such as the tip radius (R) and the Young's modulus of the sample (E). A list of well-accepted models can be found in the literature, including the most widely used Hertz, Derjaguin-Muller-Toporov (DMT) and Johnson-Kendall-Roberts (JKR) models, describing the analytical dependence on such parameters [Hertz, 1882, Burnham and Kulik, 1999, Burnham et al., 1993, Israelachvili, 2011, Fraxedas et al., 2002]. The DMT model, which will be used in this work, has the following expression in the repulsive regime:

$$F_{ts} = -\frac{HR}{6a_0^2} + \frac{4}{3} E^* \sqrt{R(a_0 - d)^{3/2}} \tag{4.3}$$

where H is the Hamaker constant, a_0 the intermolecular distance, d the tip–sample gap (related to z) and E^* the reduced Young modulus, which includes the contribution from the tip. Thus, by combining Equation'4.2 and Equation 4.3 it is possible to determine the dependence of A_n as a function of all relevant parameters. However, A_n can be hardly solved analytically, so that numerical simulations are required. On the other hand, the dynamics of the oscillating cantilever cannot be oversimplified and flexural eigenmodes must be considered, in particular when they are located close to one of the harmonics [Sahin et al., 2004a]. Here, we report a combined theoretical and experimental study on the functional dependence of the amplitudes of higher harmonics on relevant parameters such as the tip radius, free oscillation amplitude, cantilever stiffness and sample Young's modulus. Because of the low amplitudes of the involved harmonics (well below 1 nm), we concentrate on the repulsive regime of the tip–sample interaction and on those harmonics close to flexural eigenmodes of rectangular cantilevers, hence the term resonance, so that their intensities can be reliably determined [Sahin et al., 2004a, Stark and Heckl, 2000]. Previous results have shown that the intensity of the 6th harmonic is noticeably larger that the intensities of the neighbouring 5^{th} and 7^{th} harmonics, respectively, using cantilevers with 350 kHz resonant frequency and polystyrene samples [Fraxedas et al., 2015]. Such study has provided a practical qualitative method to continuously monitor changes in the shape and radius of a cantilever tip in amplitude modulation AFM mode. Here, we will also focus on the 6^{th} harmonic since it provides the larger amplitude, but the methodology can now be extended to other harmonics. The work presented here provides a tool to help to prepare experiments. Such tool is a mathematical expression describing the evolution of the 6^{th} harmonic on experimental parameters such as tip radius, free amplitude, cantilever and sample's stiffness. For given experiments directed to, e.g., the determination of the evolution of the tip radius evolution and of sample stiffness, the mathematical tool should help in the selection of the favourable range of parameter values (including amplitude set-point).

4.3 Results and Discussion

4.3.1 Simulations

Let us analyse first the dependence of the amplitude of the 6^{th} harmonic, A_6, on the independent parameters R, E and A_1, respectively, for a fixed k_c value. We will analyse the dependence of A_6 on k_c at a later stage. Note that A_1 can be externally and continuously varied by selecting the excitation amplitude and frequency of the cantilever base and that R and E depend both on the materials used. Figure 4.1a and Figure 4.1b show the calculated approach curves (as a function of z) corresponding to the amplitude and phase lag ϕ of the fundamental mode, respectively, for $A_1 = 30\,\mathrm{nm}$, $R = 10\,\mathrm{nm}$ and $E = 3\,\mathrm{GPa}$ using a $25\,\mathrm{N\,m^{-1}}$ silicon cantilever with a resonant frequency $f_0 = 300\,\mathrm{kHz}$ and a Q factor of 400. The threshold of the repulsive region ($\phi > 0°$) is represented by a vertical discontinuous grey line. Figure 4.1c displays the A_6 approach curves corresponding to the parameters used in Figure 4.1a and Figure 4.1b (continuous black line), as well as those obtained by increasing R (continuous red line), E (continuous blue line) and A_1 (continuous magenta line), respectively. The black line shows the shape of the $A_6(z)$ curve, with $A_6 > 0$ above the repulsive regime threshold, exhibiting a maximum value at $z \approx A_1/2$ and decreasing back to zero for sufficiently small z values, which correspond to small oscillation amplitudes, as depicted from Figure 4.1a. From Figure 4.1c we readily observe that A_6 increases for increasing R, E and A_1 values at a given z value, respectively. When R increases (continuous black and red curves) we observe, in addition, that the maximum of the curve shifts towards lower z values, a behaviour that is also observed for increasing E values (compare continuous black and blue lines). In fact the weight of the area under the curves is shifted towards lower z values in both cases. The comparison between the continuous black and red curves indicates that the variation of the radius has an impact in the value of A_6

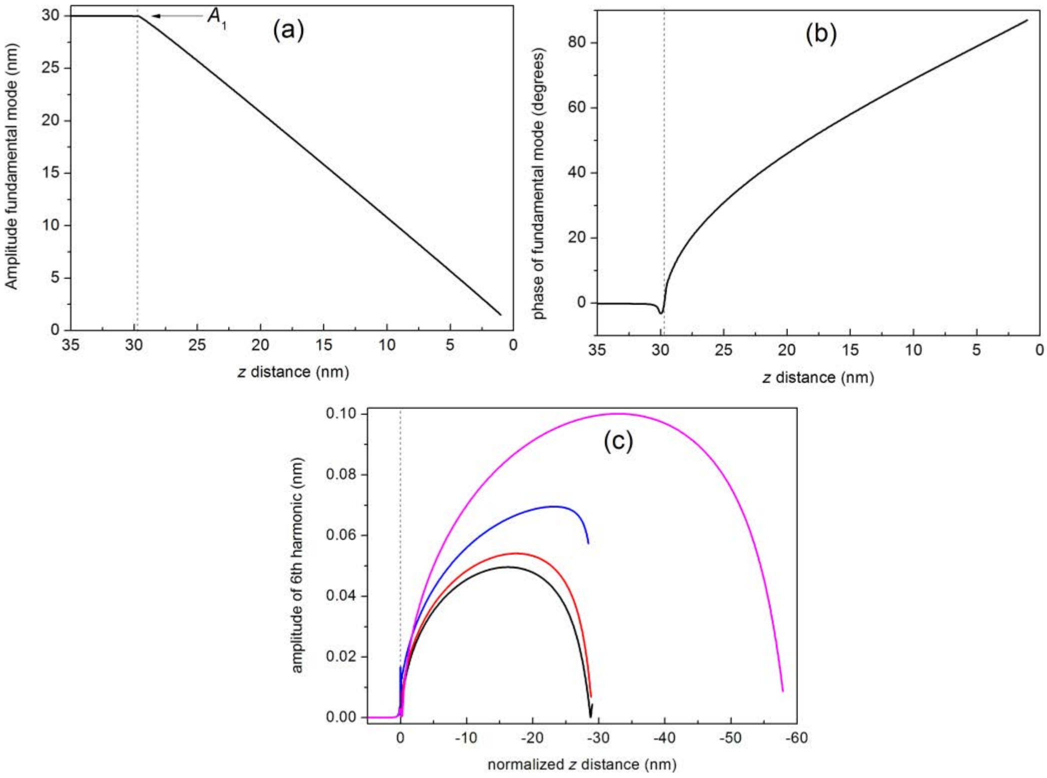

Figure 4.1: (color online) Simulated approach curves: (a) amplitude of the fundamental mode, (b) phase of the fundamental mode and (c) amplitude of the 6^{th} mode as a function of the normalized z distance. The calculations have been performed for a silicon rectangular cantilever with $k_c = 25\,\mathrm{N\,m^{-1}}$, $f_0 = 300\,\mathrm{kHz}$ and $Q = 400$. The following parameters have been used: (a) and (b) $A_1 = 30\,\mathrm{nm}$, $R = 10\,\mathrm{nm}$, $E = 3\,\mathrm{GPa}$, (c) continuous black curve $A_1 = 30\,\mathrm{nm}$, $R = 10\,\mathrm{nm}$, $E = 3\,\mathrm{GPa}$; continuous red curve $A_1 = 30\,\mathrm{nm}$, $R = 30\,\mathrm{nm}$, $E = 3\,\mathrm{GPa}$; continuous blue curve $A_1 = 30\,\mathrm{nm}$, $R = 10\,\mathrm{nm}$, $E = 130\,\mathrm{GPa}$; continuous magenta curve$A_1 = 60\,\mathrm{nm}$, $R = 10\,\mathrm{nm}$, $E = 3\,\mathrm{GPa}$.

only for certain values of the amplitude setpoint (A_{sp}): for example at $A_{sp} = 25\,\text{nm}$ ($z = 24.2\,\text{nm}$) the difference between the black and red curves is clearly smaller than for $A_{sp} = 15\,\text{nm}$ ($z = 14.2\,\text{nm}$). The same argument applies for the case of increasing E values. It means that the previous modelling of the system is necessary in order to select the appropriate experimental conditions. Let us now explore in detail the dependence of A_6 as a function of R, E and A_1. The corresponding curves are shown in Figure 4.2, where the filled black points correspond to calculated values and the continuous lines to least-square fits. The simulations have been performed for silicon with the following parameters: $k_c = 26\,\text{N}\,\text{m}^{-1}$, $f_0 = 300\,\text{kHz}$ and $Q = 400$, with $A_{sp} = 0.5A_1$. All curves confirm the increase of A_6 for increasing values of R, E and A_1 but with different evolutions. In the case of the phase of the 6^{th} harmonic the behaviour is opposite, i.e., it decreases for increasing R values (see Supporting Information File 1, Figure S1). In all cases the points closely follow a gun-shaped function with the expression:

$$G(x) = \frac{x}{g_1 + g_2 + g_3\sqrt{x}}, \tag{4.4}$$

where g_1, g_2 and g_3 are real numbers. This function covers the limiting cases of $G(x) = x/g_1$ for $g_1 \neq 0$ and $g_2 = g_3 = 0$, $G(x) = 1/g_2$ for $g_2 \neq 0$ and $g_1 = g_3 = 0$ and $G(x) = \sqrt{x}/g_3$ for $g_3 \neq 0$ and $g_1 = g_2 = 0$. Figure 4.2c exemplifies the case where the dependence is nearly linear, an approximation certainly valid for smaller intervals around a central amplitude value. In the case of Figure 4.2a and Figure 4.2b we clearly observe two well defined regions corresponding to lower and higher R and E values, respectively. At lower values A_6 exhibits a strong variation as a function of R and E (large slope) while at higher values A_6 tends towards an asymptotic limit (small slope). Thus, for the k_c values used in this simulation ($26\,\text{N}\,\text{m}^{-1}$) A_6 is most sensitive for values of tip radius below ca.10 nm (ultrasharp tips) and sample's Young's modulus below ca. 20 GPa (typically polymers). The dependence of A_6 on the cantilever properties is more complex because the cantilever shape, the elastic constant k_c, the resonance frequency f_0 and the quality factor Q are interrelated parameters that all contribute to the dynamics of the oscillation. For simplicity, we characterize the cantilever by k_c. Sader's formula, also termed Sader's method, gives a well-accepted expression of the dependence of k_c on the other parameters [Sader et al., 1999]:

$$k_c \cong 0.1906 \rho_f S_c Q f_0 \Gamma_i(f_0), \tag{4.5}$$

where ρ_f is the density of the fluid (in our case air), S_c is the plan view area of the cantilever (width × length) and Γ_i the imaginary component of the hydrodynamic function [Sader, 1998]. This expression is valid for $Q >> 1$. In order to obtain an approximate manageable expression of the functional dependence of A_6 on k_c

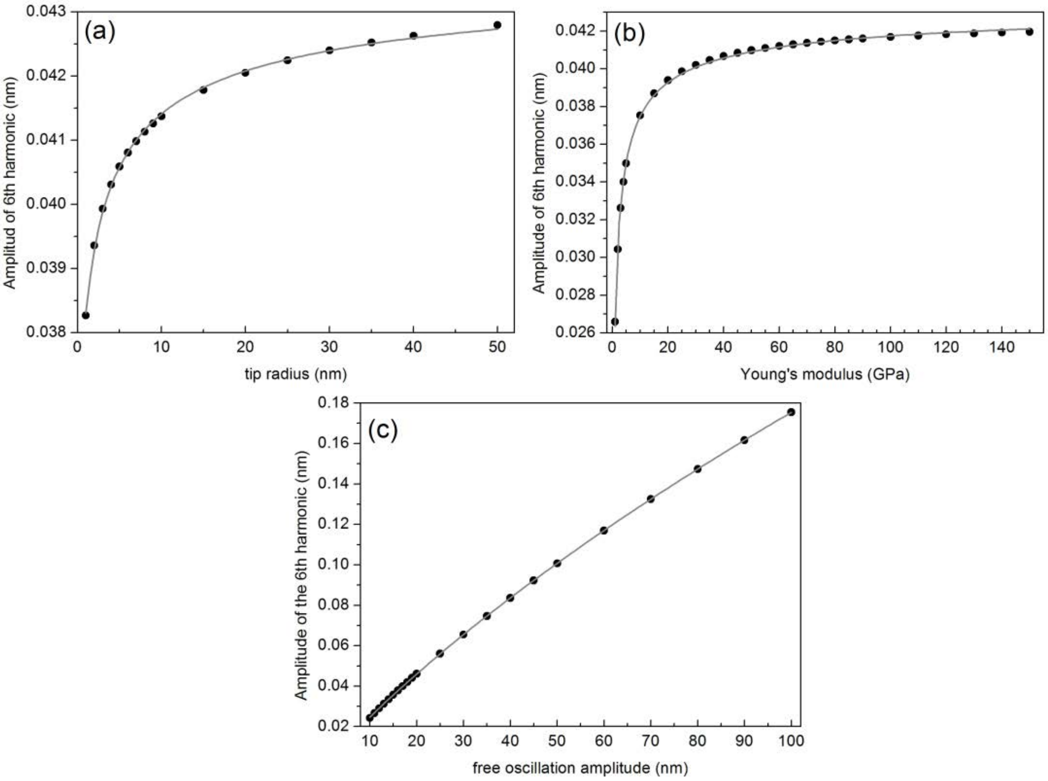

Figure 4.2: Simulated dependence of the amplitude of the 6th harmonic as a function of: (a) tip radius, (b) sample's Young's modulus and (c) free oscillation amplitude, respectively. The calculated points (filled black circles) have been performed for $k_c = 26\,\mathrm{N\,m^{-1}}$, $f_0 = 300\,\mathrm{kHz}$ and $Q = 400$ with $A_{sp} = 0.5A1$ and $A_1 = 20\,\mathrm{nm}$ for (a) and (b) and have been fitted to the gun-shaped function G described in equation 4.4. The values of the g_1, g_2 and g_3 parameters obtained from the fits are: (a) $g_1 = -1.63$, $g_2 = 22.727\,\mathrm{nm^{-1}}$, $g_3 = 5.007\,\mathrm{nm^{-1/2}}$, (b) $g_1 = 4.373\,\mathrm{GPa\,nm^{-1}}$, $g_2 = 22.84\,\mathrm{nm^{-1}}$, $g_3 = 10.737\,\mathrm{GPa^{1/2}/nm}$ and (c) $g_1 = 338.23$, $g_2 = 0.285\,\mathrm{nm^{-1}}$, $g_3 = 20.325\,\mathrm{nm^{-1/2}}$.

we have used the nominal geometrical and resonance frequency values of different commercial rectangular cantilevers, as provided by the manufacturers and Q factor values in the range $200 \leqslant Q \leqslant 600$. The resulting k_c values obtained from Equation 4.4 have been used as input to the VEDA code [Kiracofe et al., 2012]. The result from this calculation is shown in Figure 4.3. The selected cantilevers with their values are shown in the caption to the figure. The calculated points in the figure also follow quite closely Equation 4.4, with $g_1 = -63.092\,\mathrm{nN\,nm^2}$, $g_2 = 42.371\,\mathrm{nm^{-1}}$ and $g_3 = -42.223\,\mathrm{nN^{1/2}nm^{-3/2}}$. Thus, the simulations provide a functional dependence of A_6 on the relevant R, E, A_1 and k_c parameters, which can be stated as:

$$A_6 \propto G(R, E, A_1, k_c) \equiv G_r(R)G_e(E)G_a(A_1)G_k(k_c), \tag{4.6}$$

where G_r, G_e, G_a and G_k represent the decoupled gun-shaped functions with their corresponding coefficients g. The apparently different behaviours can be described by a single universal curve, where the magnitudes and signs of the g coefficients

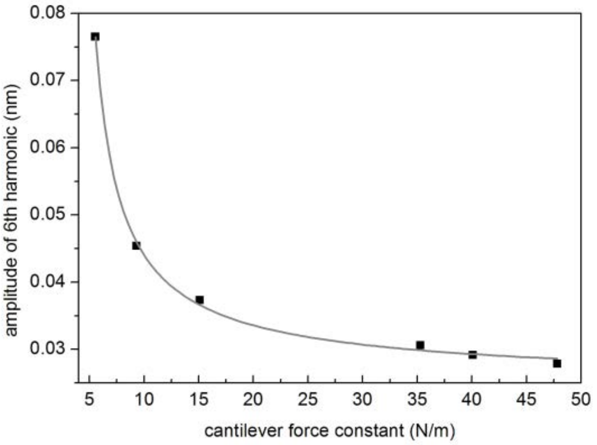

Figure 4.3: Simulated dependence of the amplitude of the 6^{th} harmonic as a function of selected values of cantilever force constants. The chosen commercial cantilevers are: RTESP-150 (BRUKER) ($f_0 = 150\,\mathrm{kHz}$, $L = 125\,\mu\mathrm{m}$, $W = 35\,\mu\mathrm{m}$), $Q = 250$, $k_c = 5.5\,\mathrm{N\,m^{-1}}$; 200ACNA ($\mu$MASCH) ($f_0 = 150\,\mathrm{kHz}$, $L = 200\,\mu\mathrm{m}$, $W = 40\,\mu\mathrm{m}$), $Q = 330$, $k_c = 9.6\,\mathrm{N\,m^{-1}}$; PPP-SEIH (NANOSENSORS) ($f_0 = 130\,\mathrm{kHz}$, $L = 225\,\mu\mathrm{m}$, $W = 33\,\mu\mathrm{m}$), $Q = 490$, $k_c = 15.1\,\mathrm{N\,m^{-1}}$; RFESPA 190 (BRUKER) ($f_0 = 190\,\mathrm{kHz}$, $L = 225\,\mu\mathrm{m}$, $W = 40\,\mu\mathrm{m}$), $Q = 550$, $k_c = 35.3\,\mathrm{N\,m^{-1}}$; RTESP-300 (BRUKER) ($f_0 = 300\,\mathrm{kHz}$, $L = 125\,\mu\mathrm{m}$, $W = 40\,\mu\mathrm{m}$), $Q = 570$, $k_c = 40.1\,\mathrm{N\,m^{-1}}$; LTESP (BRUKER) ($f_0 = 190\,\mathrm{kHz}$, $L = 225\,\mu\mathrm{m}$, $W = 38\,\mu\mathrm{m}$), $Q = 590$, $k_c = 47.8\,\mathrm{N\,m^{-1}}$.

determine the final shapes. This expression can substantially simplify the analysis of partial contributions. In addition, it paves the way to define a methodology for finding the optimal experimental conditions to monitor or characterize a specific magnitude from the acquisition of the amplitude of a higher harmonic.

4.3.2 Experiments

In the following section we compare the proposed functional dependence with experimentally derived results to validate the modelling and simulations described in previous sections.

Dependence of the amplitude of the 6th harmonic on tip radius

Let us first explore the shape of the experimental approach curves and compare to the calculations shown in Figure 4.1. Figure 4.4 shows simultaneously acquired experimental approach curves, i.e., amplitude (a) and phase (b) of the fundamental mode and amplitude of the 6^{th} harmonic (c), respectively, as a function of the piezo displacement in the direction perpendicular to the surface (z) for a nominally $k_c \approx 44\,\mathrm{N\,m^{-1}}$ cantilever with resonance frequency 293 kHz on silicon surfaces and $A_1 = 34\,\mathrm{nm}$. The black curve in Figure 4.4c was taken at the beginning of the experiment (fresh tip). The rest of the curves are acquired after the acquisition of several intermediate images (i.e., several images are taken in between each approach curve). The order in which the curves are taken was black, green, red and blue, respectively. The first conclusion that we can extract is that the simulated curves (Figure 4.1a and Figure 4.1b) reproduce well the shape of the experimental ones (Figure 4.4a and Figure 4.4b). In addition, Figure 4.4a and Figure 4.4b provide evidence that both the amplitude and phase of the fundamental mode remain unchanged during the experiments, except for a small variation in the phase at the transition between attractive to repulsive regimes ($\phi \approx 0$). Conversely, the value of A_6 as a function of the piezoscanner displacement exhibits an increase over the noise level above the threshold corresponding to the onset of the repulsive regime. We clearly observe an increase of the maximum value of A_6 as well as an increase of the position of the maximum, a trend that is reproduced by the simulations, as depicted from Figure 4.1c. Assuming that both sample's Young's modulus and k_c remain constant, then the increase of A_6 can be attributed primarily to an increase in R. The small variation of the phase (see Figure 4.4b) occurs at the transition between attractive to repulsive regimes, where the critical amplitude A_c is defined [Santos et al., 2012]. It turns out that A_c depends on R, closely following a power law function ($A_c \propto R^m$), where the parameter m ($m < 1$) depends on the particular cantilever used [Santos et al., 2012, Verdaguer et al., 2012, Ramos,

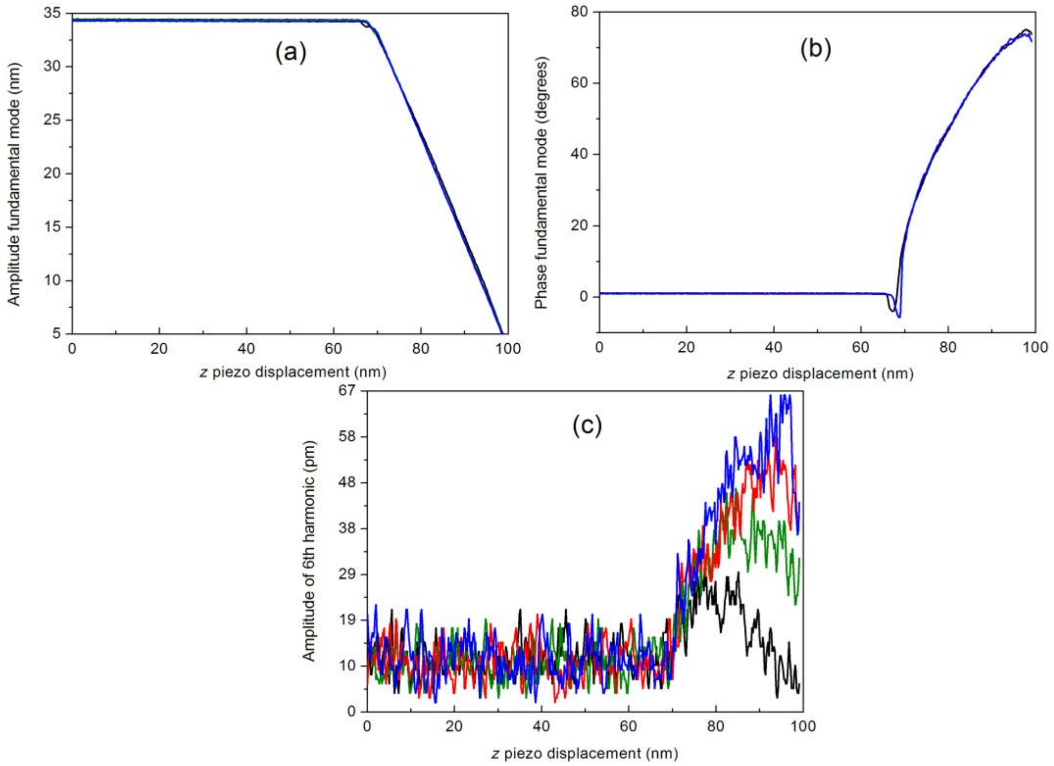

Figure 4.4: (color online) Approach curves taken alternatively with the acquisition of topographic, phase and amplitude images. (a) Amplitude of the fundamental mode, (b) phase of the fundamental mode and (c) amplitude of the 6^{th} harmonic. Experiments have been performed with a nominally $k_c \approx 44\,\mathrm{N\,m^{-1}}$ rectangular AFM cantilever with $f_0 = 293\,\mathrm{kHz}$ on silicon surfaces and $A_1 = 34\,\mathrm{nm}$.

2014, Maragliano et al., 2015]. This provides a further evidence that the observed increase of A_6 can be attributed to an increase in R. On the other hand, A_c is evaluated, in those works, at the sharp attractive–repulsive transition, which implies a rather involved experimental determination, while using approach curves one can select the set-point and thus the A_6 intensity in a larger range (within the repulsive mode). However, larger repulsions may lead to wear, and thus to damage of the tip [Liu et al., 2010b, Carpick and Salmeron, 1997, Bassani and D'Acunto, 2000, Vahdat and Carpick, 2013, Gotsmann and Lantz, 2008].

Additional information can be obtained from the acquired images. Figure 4.5 shows the evolution of the mean A_6 value acquired simultaneously with the topographic and phase images. As it is observed from the simulations and experiments, the value of A_6 is below 0.1 nm, which implies a very low signal to noise ratio. To overcome this difficulty, A_6 is acquired at each point of the AFM image ($256x256$ points) and then it is calculated by averaging all the values obtained at the image. In this way, the time evolution of the value of A_6 is expressed in terms of sequentially acquired images (each point corresponds to one image), where the experimental parameters such as A_1 and the amplitude set-point do not change over time. We observe a rapid increase from image 1 to 10 followed by an increase with a smaller slope above image number 10. The figure resembles Figure 4.2a with a higher slope at the beginning and a lower slope afterwards. Because of the expected tip wear, the evolution observed in Figure 4.5 can be again ascribed to an

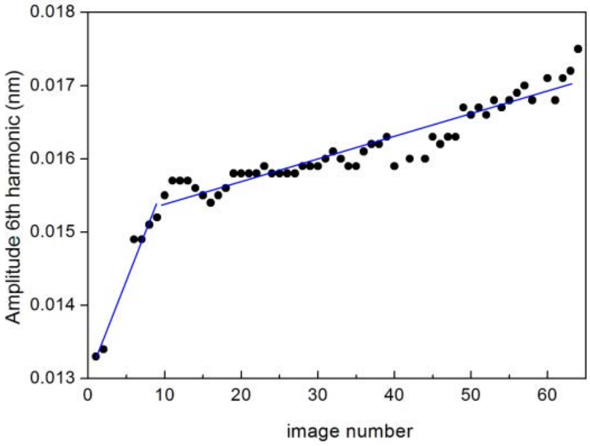

Figure 4.5: (color online) Evolution of the mean value of the amplitude of the 6^{th} harmonic extracted from the amplitude image simultaneously acquired with the topography and phase images. Experiments have been performed with a nominally $44\,\mathrm{N\,m^{-1}}$ rectangular AFM cantilever with resonance frequency 350 kHz on silicon surfaces under ambient conditions. The time evolution is expressed in terms of sequentially acquired images. The free oscillation amplitude was set to 30 nm and set-point to $A_{sp} = 27$ nm, respectively. The missing points 3, 4 and 5 correspond to approach curves taken for amplitude calibration. The continuous blue lines are guides to the eye.

increase in tip radius. This method has been proposed to monitor the stability of the tip in a continuous manner [Fraxedas et al., 2015, Killgore et al., 2011, Yan et al., 2016]. The quantitative determination of the actual tip radius at each image is a rather difficult task, since it depends critically in several experimental parameters. We have performed a parallel calibration of the tip radius with reference samples. Supporting Information File 1, Figure S2 shows the evolution of A_6 as a function of R obtained from commercial gold nanoparticles (5.5 ± 0.7 nm diameters) dispersed on a thin poly-lysine film grown on mica. From the figure we can observe the increase of A_6 for increasing R values.

Dependence of the amplitude of the 6th harmonic on bulk modulus

Figure 4.6 shows the evolution of A_6 for discrete values of Young's modulus from different materials, namely PDMS ($E = 0.0025\,\mathrm{GPa}$), LDPE ($E = 0.1\,\mathrm{GPa}$), PS ($E = 2.7\,\mathrm{GPa}$), fused silica ($E = 72.9\,\mathrm{GPa}$), titanium ($E = 110\,\mathrm{GPa}$) and sapphire ($E = 345\,\mathrm{GPa}$), using a $10.9\,\mathrm{N\,m^{-1}}$ cantilever, as determined with the thermal tune method and Sader's corrections [Sader et al., 2014]. In spite of the reduced number of experimental points, the curve can be compared to Figure 4.2b, with a sharp increase at low E values and a nearly constant value for larger E values. One has to take into account that during the experiments, where the tip has to be retracted and samples have to be changed, a variation of the tip radius cannot be excluded. The sample with the highest wear was titanium, because of its higher roughness as compared to the rest of the samples, and for this reason it was measured at the end of the cycles. From the figure it can be clearly observed that A_6 for the titanium sample shows the larger values.

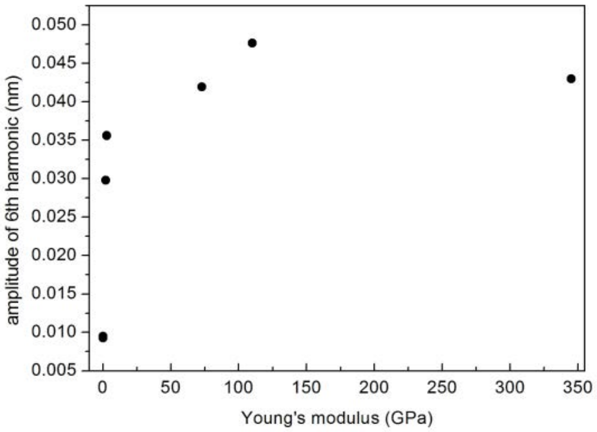

Figure 4.6: Experimental evolution of $A_6 vs E$ for PDMS ($E = 0.0025\,\mathrm{GPa}$), LDPE ($E = 0.1\,\mathrm{GPa}$), PS ($E = 2.7\,\mathrm{GPa}$), fused silica ($E = 72.9\,\mathrm{GPa}$), titanium ($E = 110\,\mathrm{GPa}$) and sapphire ($E = 345\,\mathrm{GPa}$) using a $10.9\,\mathrm{N\,m^{-1}}$ cantilever.

Dependence of the amplitude of the 6th harmonic on free oscillation amplitude

Figure 4.7a shows the evolution of A6 as a function of the free oscillation amplitude as determined experimentally with nominally $26\,\mathrm{N\,m^{-1}}$ cantilevers. The experimental points (full black circles) correspond to the mean A_6 values obtained from the average of a full image acquisition of the 6^{th} harmonic, in analogy to the experiments described in Figure 4.5. The points have been fitted to the G function from Equation 4.4. The nearly linear behaviour agrees with the predictions shown in Figure 4.2c and strongly suggests that the tip radius has not changed during the measurements, since otherwise the behaviour of A_6 would have been nonlinear, with a slope increasing for increasing A_1 values. In addition, Figure 4.7b shows the evolution of A_6 as a function of sequentially acquired images using softer cantilevers ($k_c \approx 3\,\mathrm{N\,m^{-1}}$), where both A_1 and A_{sp} have been intentionally varied during the experiment. Note that here A_6 increases for increasing A_1 values, as observed in Figure 4.7a, and that for a particular couple of A_1 and A_{sp} values, A_6 increases due to tip wear, and thus to an increase in tip radius. Note the higher A_6 values in Figure 4.7b, as compared to those in Figure 4.7a for similar A_1 values. This is essentially due to the softer cantilevers used in Figure 4.7b, an effect described in Figure 4.3.

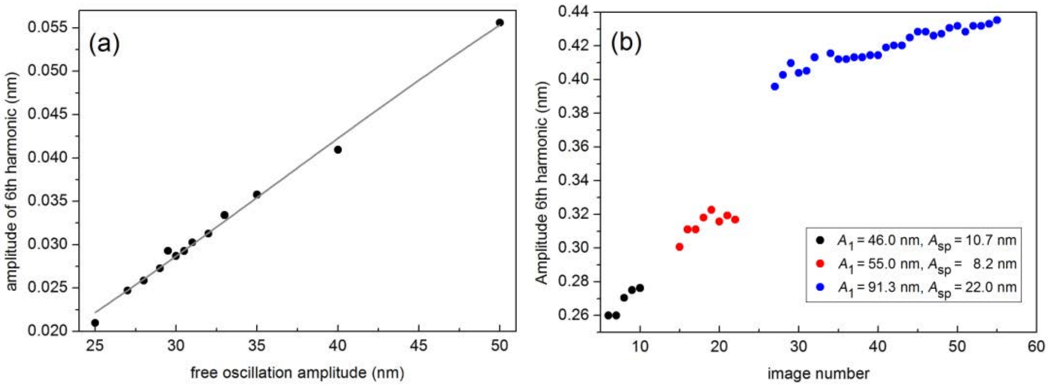

Figure 4.7: (color online) (a) Experimental evolution of A_6 as a function of the free oscillation amplitude using $26\,\mathrm{N\,m^{-1}}$ cantilevers. The fit to Equation4.4 leads to $g_1 = 3,016.794$, $g_2 = 38.23\,\mathrm{nm^{-1}}$ and $g3 = -569.14\,\mathrm{nm^{-1/2}}$. (b) Evolution of the mean value of the amplitude of the 6^{th} harmonic extracted from the amplitude images simultaneously acquired with the topography and phase images. The amplitude has been calibrated using the sensitivity determined from approach curves. The experiments have been performed with a $k_c = 3.1\,\mathrm{N\,m^{-1}}$ rectangular AFM cantilever with a resonance frequency of 74.46 kHz and $Q = 231$, as determined with the thermal tune method, on silicon surfaces. The time evolution is expressed in terms of sequentially acquired images. Three different A_1 and A_{sp} pairs have been used: $A_1 = 46.0\,\mathrm{nm}$, $A_{sp} = 10.7\,\mathrm{nm}$ (black full dots), $A_1 = 55.0\,\mathrm{nm}$, $Asp = 8.2\,\mathrm{nm}$ (red full dots) and $A_1 = 91.3\,\mathrm{nm}$, $A_{sp} = 22.0\,\mathrm{nm}$ (blue full dots).

4.4 Conclusion

Based on numerical simulations using the VEDA code we have proposed a functional dependence of the amplitude of the 6th harmonic of rectangular cantilevers on the tip radius, sample's Young's modulus, free oscillation amplitude and cantilever force constant. The 6th harmonic has been chosen because it is in close resonance with the 2^{nd} flexural mode, leading to observable signals, and because its frequency is within the reach of the control electronics used in the experiments. The outcome of the simulations is that the 6^{th} harmonic can be analytically expressed by the product of four identical decoupled gun-shaped functions, each one associated with a specific parameter and with its own coefficients. Thus, the partial evolution for a particular parameter can be traced using this universal behaviour. The simulations have been validated with AFM experiments using rectangular cantilevers in the $3\,\mathrm{N\,m^{-1}}$ to $45\,\mathrm{N\,m^{-1}}$ range and different samples in the 2 GPa to 345 GPa range. The predicted trends are well reproduced by the experiments. As we can notice from the different trends, the 6^{th} harmonic is most sensitive to changes in tip radius for values of tip radius below ca. 10 nm and Young modulus below ca. 20 GPa. If we consider the method for implementing tip radius real time monitoring, this will be more effective when sharp (new) tips are imaging stiff samples. Instead, in order to measure the surface Young modulus the modelling shows that the best results will be obtained using larger tip radius (10 nm to 15 nm) in order to have an almost constant radius-dependent contribution. So far the results are only qualitative. In order to obtain trustworthy predictions, a more precise and more accurate calibration of the cantilever is still necessary. The performed simulations might also be improved including parameters which could be varied and measured experimentally in order to refine the method and make the results of the simulations more comparable to the experimental ones. The mathematical tool that we present here based on gun-shaped functions allows to identify the optimal conditions to obtain information about the properties of materials from the harmonic response in non-contact dynamic modes.

4.4.1 Simulations and Experimental Details

Simulations

Simulations have been performed using the Virtual Environment for Dynamic AFM (VEDA) open code, which takes into account the dynamics of oscillating rectangular cantilevers with multiple eigenmodes [Kiracofe et al., 2012]. The frequencies, stiffness and quality factors of the 2^{nd} flexural eigenmode have been approximated by the known relationships $6.27f$, $6.272k_c$ and $6.27Q$, respectively, corresponding to a massless tip [Garcia and Herruzo, 2012]. As mentioned above, we have used the DMT model to describe the tip–surface interaction and the tip has been approximated by a hemisphere with a well-defined radius R. For simplicity neither viscoelastic nor capillary forces have been considered. The negligible contribution of viscoelastic forces in PS with $25\,\mathrm{N\,m^{-1}}$ cantilevers is discussed in the Supporting Information File 1 (see Figure S3).

Experimental

AFM experiments have been performed with a Bruker DIMENSION ICON instrument hosted in a homemade controlled humidity environment with Nanoscope V control electronics. Commercial rectangular microfabricated silicon cantilevers with ultrasharp silicon tips ($R < 10\,\mathrm{nm}$) have been used with the following nominal values: OTESPA (Bruker) with $k_c \approx 44\,\mathrm{N\,m^{-1}}$ and $300 \leq f_0 \leq 400$ kHz, OTESPA-R3 (Bruker) with $k_c \approx 25\,\mathrm{N\,m^{-1}}$ and $200 \leq f_0 \leq 400$ kHz, and PPP-FMR (Nanosensors) with $k_c \approx 3\,\mathrm{N\,m^{-1}}$ and $70 \leq f_0 \leq 80$ kHz, where f_0 stands for the resonance frequency. The amplitudes of the higher harmonics were registered using an internal lock-in amplifier. In general, such amplitudes will depend on the selected working frequency. The effect of working slightly off-resonance is discussed in Supporting Information File 1, Figure S4. The estimation of the A_n magnitudes (in *nm*) has been obtained by calibration of the laser-detector sensitivity, which is about $100\,\mathrm{nm\,V^{-1}}$, as determined from force curves. Humidity was kept below 20%. The z motion of the piezoscanner has been calibrated using virtual standards [Koops et al., 2015]. Due to the value of the fundamental resonance frequency of the employed cantilevers, we have focused in the resonance of the 2^{nd} flexural mode and the 6^{th} harmonic, which frequencies are below 2.5 MHz, since the control electronics is limited to 5 MHz.

4.5 Acknowledgements

This work has been performed within the aim4np project (Automated in-line Metrology for Nanoscale Production), which is supported by the EC through a grant (contract Nr. 309558) within the 7th Frame-work Program NMP Call 2012.1.4-3 on Nanoscale mechanical metrology for industrial processes and products (Patent pending), and within the framework of the PhD program in Physics of the Autonomous University of Barcelona. ICN2 acknowledges support of the Spanish MINECO through the Severo Ochoa Centers of Excellence Program under Grant SEV-2013-0295. IMB-CNM, CSIC acknowledges the grant CSD2010-00024.

4.6 Supporting Information

We have acquired AFM images of topograhy and amplitude of the 6th harmonic on a calibration sample of gold nanoparticles, with a diameter of $5.5 \pm 0.7\,\mathrm{nm}$,

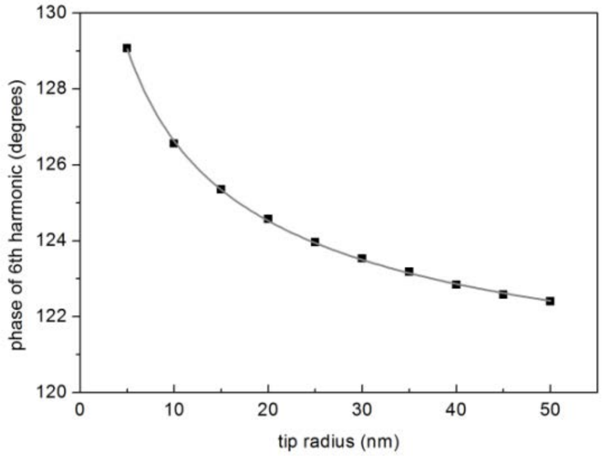

Figure 4.8: Simulated evolution of the phase of the 6th harmonic (full black squares) as a function of the tip radius. The calculations have been performed for a silicon rectangular cantilever with $k_c = 25\,\mathrm{N\,m^{-1}}$, $f_0 = 300\,\mathrm{kHz}$ and $Q = 400$ with $A_1 = 30\,\mathrm{nm}$, $R = 10\,\mathrm{nm}$, $E = 3\,\mathrm{GPa}$ (as in Figure 1) and an amplitude setpoint of 10.8 nm ($z = 10\,\mathrm{nm}$). The continuous grey line corresponds to a least-square fit using the gun-shape function from Equation4.4: $g_1 = 0.001\,38\,\mathrm{nm}\,{}^{\circ -1}$, $g_2 = 0.008\,45\,{}^{\circ -1}$ and $g_3 = -0.002\,18\,\mathrm{nm}^{0.5}\,{}^{\circ -1}$

.

dispersed on a thin layer of poly-lysine deposited on a mica substrate. The estimation of the tip radius has been extracted from the topography images using the geometrical model from Vesenka, J.; Manne, S.; Giberson, R.; Marsh, T.; Henderson, E. Colloidal gold particles as an incompressible atomic force microscope imaging standard for assessing the compressibility of biomolecules. Biophysical Journal 1993, 65, 992–997.

From Figure S4c we observe an asymmetric behaviour of the 6th harmonic: above resonance the amplitude is higher. Such an enhancement is due to the fact that, under the experimental conditions and for the particular cantilever used, the frequency of the 6^{th} harmonic is closer to the frequency of the maximum amplitude of the 2^{nd} flexural mode. In Figure S4d we plot the amplitude of the 6^{th} harmonic as a function of their corresponding amplitudes of the fundamental modes. In the absence of tip-surface interaction (free oscillation) we obtain an estimation of the noise level (about $\pm 100 \mu V$). Within the repulsive mode, the amplitude of the 6th harmonic increases for decreasing amplitudes of the fundamental mode (equivalent to the decrease of the amplitude set-point).

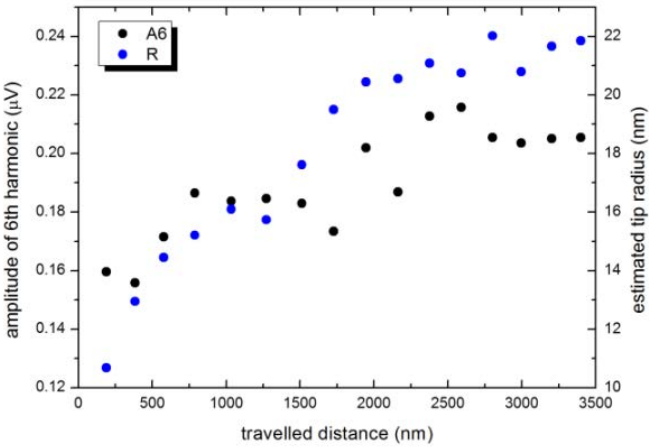

Figure 4.9: Evolution of the amplitude of the 6^{th} harmonic (full black circles) and of the estimated tip radius (full blue circles) as a function of the distance travelled by the tip.

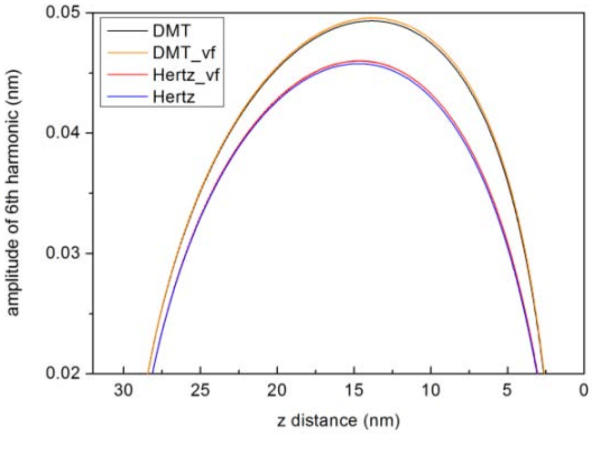

Figure 4.10: Simulated evolution of the amplitude of the 6^{th} harmonic as a function of the z distance. Both DMT and Hertz models have been used with no viscoelastic forces (continuous black and blue lines, respectively) and including viscoelastic forces (continuous orange and red lines, respectively). We have used the three element model to account for the viscoelastic forces: $E_1 = 3\,\mathrm{GPa}$, $E_2 = 11.5\,\mathrm{GPa}$ and $\eta = 58\,\mathrm{GPa\,s}$, where E_1, E_2 and η stand for the PS Young's modulus, delayed Young's modulus and viscosity, respectively [Cheng, L.; Xia, X.; Scriven, L. E.; Gerberich, W. W. Spherical-tip indentation of viscoelastic material, Mechanics of Materials 2005, 37, 213-226].

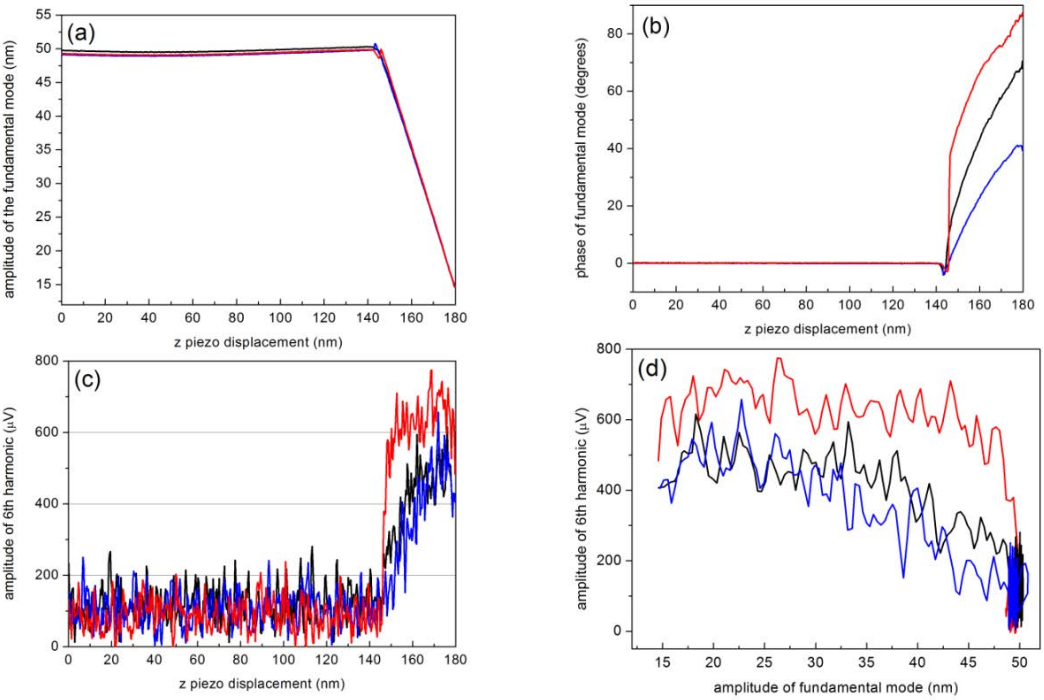

Figure 4.11: Experimental approach curves: (a) amplitude and (b) phase of the fundamental mode and (c) amplitude of the 6^{th} harmonic as a function of the z piezo displacement using cantilevers force constant around 25 GPa with resonance frequencies of about 246 kHz and clean silicon samples. The approach curves were taken when the excitation requency corresponds to the frequency of the first eigenmode (continuous black lines), and off-resonance at frequencies corresponding to 90% of the maximum of amplitude, at both sides, below (continuous blue line) and above (continuous red line) resonance, respectively. The individual phase curves have been shifted to 0° (free oscillation) for the sake of comparison. The amplitude of the 6^{th} harmonic as a function of their corresponding amplitudes of the fundamental modes is shown in (d).

Chapter 5

Quantification of nanomechanical properties of surfaces by higher harmonic monitoring in amplitude modulated AFM imaging

Federico Gramazio[a], Matteo Lorenzoni[b], Francesc Pérez-Murano[b], Laura Evangelio[a,b], Jordi Fraxedas[a]

a Catalan Institute of Nanoscience and Nanotechnology (ICN2), CSIC and BIST, Campus UAB, Bellaterra, Barcelona 08193, Spain **b** Instituto de Microelectrónica de Barcelona (IMB-CNM, CSIC), Campus UAB, Bellaterra, Barcelona 08193, Spain

5.1 Abstract

The determination of nanomechanical properties is an intensive topic of study in several fields of nanophysics, from surface and materials science to biology. At the same time, amplitude modulation force microscopy is one of the most established techniques for nanoscale characterization. In this work, we combine these two topics and propose a method able to extract quantitative nanomechanical information from higher harmonic amplitude imaging in atomic force microscopy. With this method it is possible to discriminate between different materials in the stiffness range of 1 GPa to 3 GPa, in our case thin films of PS-PMMA based block copolymers. We were able to obtain a critical lateral resolution of less than 20 nm and discriminate between materials with less than a 1 GPa difference in modulus. We show that within this stiffness range, reliable values of the Young's moduli can be

obtained under usual imaging conditions and with standard dynamic AFM probes.

5.2 Introduction

The investigation of interactions between surfaces allows the understanding of a wide range of phenomena from friction to stability of colloidal particles in liquid media [Israelachvili, 2011]. A theoretical understanding of surface forces was developed by Hertz [Hertz, 1882], Derjaguin and Landau [Derjaguin and Landau, 1993], Johnson, Kendall and Roberts [Johnson et al., 1971] and Derjaguin, Muller and Toporov [Derjaguin et al., 1975], to mention the most widely referred. From the experimental point of view, the invention of the atomic force microscope (AFM) in 1986 [Binnig and Quate, 1986] allowed the study of near-surface mechanical properties at the nano-scale thanks to the possibility of measuring forces in the pN range, with a sensitivity and spatial resolution smaller than that provided by the dynamical mechanical analysis (DMA) apparatus [Menard, 2008]. Several operation modes have been developed in order to improve the performance of AFM in the measurement of mechanical properties [Passeri et al., 2013] including quasi-static (indentation [Fraxedas et al., 2002], force-volume mode [Kim et al., 2009], adhesion force mode [Van Der Werf et al., 1994]), dynamic in contact mode (force modulation [Maivald et al., 1991], contact resonance [Rabe et al., 2002], ultrasonic force microscopy [Yamanaka et al., 1999]) and dynamic in intermittent contact mode (phase imaging [Tamayo and Garcia, 1996], phase modulation [Fukuma et al., 2006], loss tangent imaging [Proksch and Yablon, 2012], pulsed-force [Rezende et al., 2009] and multifrequency including bimodal [Garcia and Proksch, 2013, Eslami et al., 2014] and multiharmonic [Raman et al., 2011]). Despite this variety of techniques, the extraction of elastic moduli and viscoelastic constants remains problematic due to the difficulty of correctly describing the tip-surface contact area and the lack of accurate models which can describe the contact mechanics appropriately [Raman et al., 2008]. Within the panorama of intermittent contact techniques, one of the most widely used is the amplitude modulation (AM-AFM) in repulsive mode, where the tip is periodically in contact with the sample surface. When the tip interacts with the sample surface, harmonic signal components are induced to the cantilever motion due to the non-linear character of the interaction [Stark and Heckl, 2000]. These components and the force acting on the cantilever can be expressed in terms of Fourier series, as exhaustively described in theoretical works [Stark and Heckl, 2000, Dürig, 2000, Sahin et al., 2004a]. Although the higher harmonic amplitudes are well below 1 nm, such amplitudes can be monitored with a reasonable signal-to-noise ratio when they are amplified by a flexural eigenmode. In our case, we chose to detect the 6th harmonic oscillation amplitude because it is in close proximity with the 2^{nd} flexural eigenmodes. Considerable theoretical effort has been made in the last few years to describe and understand the potential use of higher harmonics [Stark and Heckl, 2003, Giessibl, 2006, Santos et al., 2014] and its functional dependence on relevant parameters such as cantilever force constant (k_c), tip radius (R), free oscillation amplitudes (A_0) and sample stiffness (E) [Fraxedas et al., 2015, Gramazio et al., 2017]. It is well known that only a few amplitude signals are detectable when the tip-sample interaction is kept gentle i.e. 100 pN [Gadelrab et al., 2013]. To overcome this limitation, we extrapolated the most suitable experimental conditions in order to enhance the higher harmonic signal by carrying out simulations with the Virtual Environment for Dynamic AFM (VEDA) software [Kiracofe et al., 2012]. The focus was on the experimental quantification of sample surface Young modulus (E) analysing the amplitude of the 6^{th} higher harmonic and comparing it with the simulations. This is the first time that experiments have been conducted to estimate surface mechanical properties in the optimum conditions for this method. The samples chosen for the E quantification were block copolymers (BCPs) thin films [Chou et al., 1996, Mansky et al., 1995].

5.3 Materials and Methods

5.3.1 Simulations

Simulations were performed using the VEDA open code, which takes into account the dynamics of oscillating rectangular cantilevers with multiple eigenmodes [Kiracofe et al., 2012]. The frequencies, stiffness and quality factors of the 2^{nd} flexural eigenmode have been approximated by the known relationships $6.27 f_0$, $6.272 k_c$ and $6.27 Q$, respectively, corresponding to a massless tip, where f_0 and Q stand for the resonance frequency (fundamental mode or first eigenmode) and the quality factor, respectively [Garcia and Herruzo, 2012]. We have used the Derjaguin-Muller-Toporov (DMT) model to describe the tip–surface interaction [Derjaguin et al., 1975] and the tip was approximated by a hemisphere with a well-defined radius $R = 5\,\mathrm{nm}$. For simplicity, neither capillary nor viscoelastic forces were considered. This is justified by the low humidity used in the experiments (see below) and by the negligible contribution of viscoelastic forces to the 6^{th} harmonic according to VEDA simulations (see Figure 4.10 from chapter 4).

5.3.2 Experimental

AFM imaging of topography, fundamental mode phase and 6th higher harmonic were performed in the repulsive mode in order to enhance the 6^{th} higher harmonic amplitude (A_6) signal well above the noise level of the employed electronic. A commercial AFM was employed, hosted in a homemade controlled humidity environment. Commercial TESP SS (Bruker) rectangular microfabricated silicon cantilevers with ultrasharp silicon tip ($2 < R < 5 nm$) were used with the nominal values $k_c \approx 42\,\mathrm{N\,m^{-1}}$ and $f_0 \approx 300\,\mathrm{kHz}$. The amplitude of the higher harmonics was registered using a digital signal processing (DSP) dual phase, wide bandwidth external lock-in amplifier. The use of an external lock-in allowed us to improve the signal-to-noise ratio and the lowest limit of detectable values within the range of 70 µV to 600 µV as evidenced by a resulting higher resolution at lower free amplitude values as compared to those achievable with an internal lock-in. The laser spot was positioned at its revealed maximum intensity, coinciding with the position of the tip along the cantilever, and the dynamical k_c was calibrated performing thermal tune measurement applying Sader's corrections [Schäffer, 2005, Sader et al., 2014]. In order to convert the 6^{th} higher harmonic amplitude values from µV to nm, the laser-detector deflection sensitivity was calibrated by performing a ramp in tapping mode on a sapphire calibration sample. AFM measurements were always performed at relative humidity below 10%, in order to reduce the capillarity condensation at the tip-surface interaction as much as possible.

5.3.3 Self-assembled Block Copolymers samples

BCPs are macromolecules built from more than one species of monomers with inter-monomer covalent bonding which tend to segregate due to the repulsion between different blocks and undergo a separation phase with controllable dimensions and functionalities [Seul and Andelman, 1995, Bates and Fredrickson, 1990]. These materials show periodic structures with a characteristic width or pitch and have been found interesting for high volume manufacturing in the semiconductor industry [Liu et al., 2010a, Rathsack et al., 2013]. The fact that low cost and nanometer scale features at high throughput are obtainable by directed self-assembly (DSA) is attracting interest in the whole fields of lithography and surface patterning. The samples employed in the present work were made using poly(styrene-b-methylmethacrylate) ($PS - b - PMMA50 : 50$, $Mn = 79\,\mathrm{kg\,mol^{-1}}$, $PDI = 1.13$) provided by Arkema and assembled on a polystyrene based (PS-OH) brush layer. BCP was dissolved in a 1.5% (w/w) solution of propylene glycol methyl ether acetate (PGMEA). Thin films made of this BCP form lamellae with a nominal pitch of 37 nm. In order to graft the brush layer, the prepared surfaces were annealed for 5 min at 230 °C in nitrogen atmosphere. The remaining ungrafted brush was removed with PGMEA rinsing. Above this brush layer, the L37 solution was spin-coated and annealed a second time for 10 min at 230 °C in nitrogen atmosphere, to induce the lamellae selfassembly with a nominal pitch of 37 nm. In order to selectively modify the stiffness of one of the phases of the block co-polymer samples, a Sequential Infiltration Synthesis (SIS) process was applied [Lorenzoni et al., 2017]. Alumina, obtained from binary reactions of trimethylaluminium (TMA) and water at 135 °C, was obtained at the end of the infiltration process which took place in two steps: first, TMA was placed in a vacuum chamber for 60 s and then, once purged, water was introduced. This entire sequence was repeated for 5 times, and each time the infiltration process not only covered the top domain but the whole polymer domains, resulting in a global improvement of resistant hardness, leading to high-aspect-ratio features in a substrate [Peng et al., 2010,Biswas et al., 2014,Biswas et al., 2015,Ruiz et al., 2012].

5.4 Results and Discussion

In a previous work we have explored the functional dependence of A_6 as a function of R, A_0, E and k_c and shown that A_6 follows a universal gun-shape curve, with coefficients that depend on the values of the mentioned parameters [Fraxedas et al., 2015,Gramazio et al., 2017]. The functional dependence can help to determine the best experimental conditions to quantify, e.g., E. The simulations shown in Figure 5.1 indicate the evolution of A_6 as a function of the mentioned parameters and are useful to select the experimental conditions aimed to maximize the signal and the sensitivity in order to extract experimental values of the Young's modulus. Figure 5.1a shows the dependence of A_6 as a function of the z distance (the distance between the cantilever base and the sample surface). $A_6(z)$ increases upon entering the repulsive region (dashed vertical green line) and reaches its maximum (blue vertical line) around $A_0/4$. Most of the experiments presented in this work have been performed with an amplitude set point (A_{sp}) of 50% of A_0 (dashed red line), and under this condition A_6 is close to its maximum value. The evolution of A_6 as a function of selected values of k_c is shown in Figure 5.1b. Note that the amplitude decreases for increasing cantilever spring constant values, approximately following a $1/k_c$ dependence [Giessibl, 2006,Gramazio et al., 2017]. From the figure we observe that the value of A_6 is not very much dependent on the values of k_c for $kc > 20\,\mathrm{N\,m^{-1}}$. Figures 5.1c and d show the dependence of A_6 as a function of E for $k_c = 0.1\,\mathrm{N\,m^{-1}}$ (Figure 5.1c) and $k_c = 26\,\mathrm{N\,m^{-1}}$ and $k_c = 42\,\mathrm{N\,m^{-1}}$, respectively (Figure 5.1d), to cover a wide range of k_c values. From the curves it becomes evident that the sensitivity (expressed in terms of the slope of the curve and represented in Figures 5.1e and f, respectively) is highest for $E < 5\,\mathrm{GPa}$, which is the region of interest for the polymers selected in this work. Above $E \approx 10\,\mathrm{GPa}$ the slope becomes increasingly smaller which indicates that standard dynamic mode cantilevers would be not indicated for the quantitative determination of the E values. From Figure 5.1b one would be tempted to choose the softest cantilevers, since the predicted A_6 signal is larger. However, very soft cantilevers are unstable in the repulsive mode due to torsional deformations and exhibit lower Q values. In our case we have selected the $46\,\mathrm{N\,m^{-1}}$ cantilevers because of their mechanical stability, larger Q values and since the predicted A_6 signals are not significantly smaller than those corresponding to the intermediate cantilevers (ca. $20\,\mathrm{N\,m^{-1}}$). Although a clear disadvantage when using stiffer cantilevers is the associated lower accuracy in the estimation of the actual k_c value using thermal tune calibration methods and

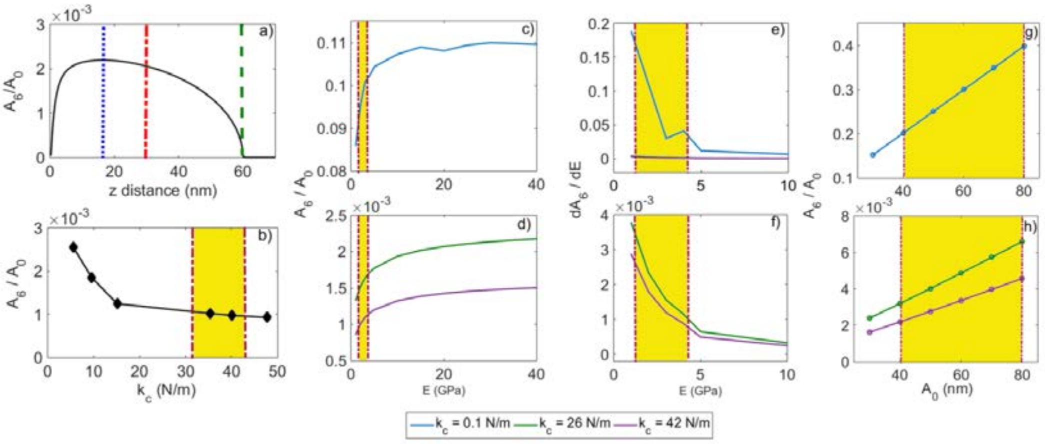

Figure 5.1: (a) Simulated dependence of A_6 normalized to A_0 as a function of the distance (z) between the cantilever base and the surface of the sample at $A_0 = 60\,\mathrm{nm}$: the discontinuous green vertical line shows the threshold of the repulsive regime, the discontinuous red line represents the z distance at $A_{sp} = 0.5A_0$ and the blue line represents the z distance at which A_6 reaches its maximum. (b) Simulation of the dependence of A_6 normalized to A_0 as a function of k_c, using selected nominal values (see chapter 4 for details). Evolution of A_6 normalized to A_0 as a function of E for (c) $k_c = 0.1\,\mathrm{N\,m^{-1}}$(continuous blue line) and (d) $k_c = 26\,\mathrm{N\,m^{-1}}$ (continuous green line) and $kc = 42\,\mathrm{N\,m^{-1}}$ (continuous magenta line). The derivative of curves in (c) and (d) are shown in (e) and (f), respectively, in order to highlight the slopes. Evolution of A_6 normalized to A_0 as a function of A_0 for (c) $k_c = 0.1\,\mathrm{N\,m^{-1}}$ (blue dots) and (d) $k_c = 26\,\mathrm{N\,m^{-1}}$ (green dots) and $k_c = 42\,\mathrm{N\,m^{-1}}$ (magenta dots). The yellow highlighted areas represent the working range: $E = 0.1\,\mathrm{MPa}$ - $4.7\,\mathrm{GPa}$, $k_c = 30\,\mathrm{N\,m^{-1}}$ to $43\,\mathrm{N\,m^{-1}}$. All A_6 values have been calculated at 50% of A_0.

the resulting lower oscillation amplitudes, the fact that the dependence of k_c on the value of E is low mitigates the uncertainty on its quantification. However, and as will be shown next, the lower values obtained from using a stiffer cantilever can be compensated by increasing the free oscillation amplitude A_0. This is shown in Figures 5.1g ($k_c = 0.1\,\mathrm{N\,m^{-1}}$) and h ($k_c = 26\,\mathrm{N\,m^{-1}}$ and $k_c = 42\,\mathrm{N\,m^{-1}}$), where it is observed that A_6 increases linearly with A_0 in the 40 nm to 80 nm range. A_0 appears to be a crucial working parameter directly linked to the peak force exerted on the sample: higher harmonics increase monotonically with A_0 and, in this range of values, are excited above the noise level without plastic deformation, despite the observation of large deformations as a free amplitude of 80 nmis approached. As the free amplitude was increased the dynamic excitation of the cantilever changed. To have an idea of how tip-sample interaction changes, an experiment under repulsive regime was considered, at a constant set-point value (50%). Higher peak interaction force was exerted as A_0 increased. The peak interaction force, Fpeak , can be expressed as [Hu and Raman, 2007]:

$$F_{peak} = 1.4/[(E^*\sqrt{R}^{-1/4})(Q/k_c)^{3/4}A_0^{-9/8}], \tag{5.1}$$

where E^* is the effective tip-sample elastic modulus. Equation5.1 predicts Fpeak ranging from 3.4 nN ($A_0 = 40\,\mathrm{nm}$) to 6.3 nN ($A_0 = 70\,\mathrm{nm}$) using $R = 5\,\mathrm{nm}$, $k_c = 42\,\mathrm{N\,m^{-1}}$, $Q = 600$ and $E^* \approx 2\,\mathrm{GPa}$, since the Young's modulus corresponding to silicon is much larger than the value corresponding to the PS and PMMA polymers. Within this range of forces, the DMT model predicts a deformation in the range of 3 nm to 8 nm, as found experimentally (see Figure 5.2a). This range of free amplitude values is higher than those usually employed in force reconstruction experiments [Payam et al., 2015,Herruzo et al., 2014]. In our case, working at higher amplitudes allowed us to obtain a clearer detectable signal and compare the resulting trends with the simulations.

5.4.1 PS - LDPE

As a first step, the 6^{th} higher harmonic signal was studied on a Bruker's calibration sample of PS and low density polyethylene (LDPE), having nominal E values of 2.0 GPa and 0.1 GPa, respectively. The morphology of the surface consisted of a PS surface with LDPE semispherical micro-droplets. This kind of sample is a good starting point because the two phases are easily distinguishable in the topography (Figure 5.2a), the phase channel (Figure 5.2b) and also from the 6^{th} higher harmonic amplitude image (Figure 5.2c) because of the large difference in Young's moduli (about 2 GPa) between the two phases. We were also able to verify that increasing A_0 exerts higher forces inducing an increased deformation, as can be seen in the topography (Figure 5.2a). It can be clearly observed that the droplet of LDPE at $A_0 = 70\,\mathrm{nm}$ (right half) shows a higher deformation than the one at $A_0 = 40\,\mathrm{nm}$ (left half). Despite the deformation, the theoretical values agreed with the experimental ones, as shown in Figure 5.2e, confirming that the DMT model [Derjaguin et al., 1975,Cappella, 2016] was also still valid at these amplitudes ranges. The images were analyzed with the Gwyddion software [Necas and Klapetek, 2012] applying a threshold masking of the 6th higher harmonic image according to the Otsu method [Otsu, 1979], in order to discriminate the signal value from the two materials (Figure 5.2d). The trend of A_6 mean values, taken from the different phases at different A_0, allows a clearer comparison with the simulations (Figure 5.1h). The experimental results for PS lay between the two simulations performed for $E = 2\,\mathrm{GPa}$ and $E = 1.8\,\mathrm{GPa}$, while those for the LDPE lay between the simulations for $E = 0.1\,\mathrm{GPa}$ and $E = 0.2\,\mathrm{GPa}$. The obtained results and their indetermination were perfectly compatible with other works that have performed analogous measurements on the same kind of sample using other methods such as Force reconstruction [Payam et al., 2015] and nanomechanical spectroscopy [Herruzo et al., 2014].

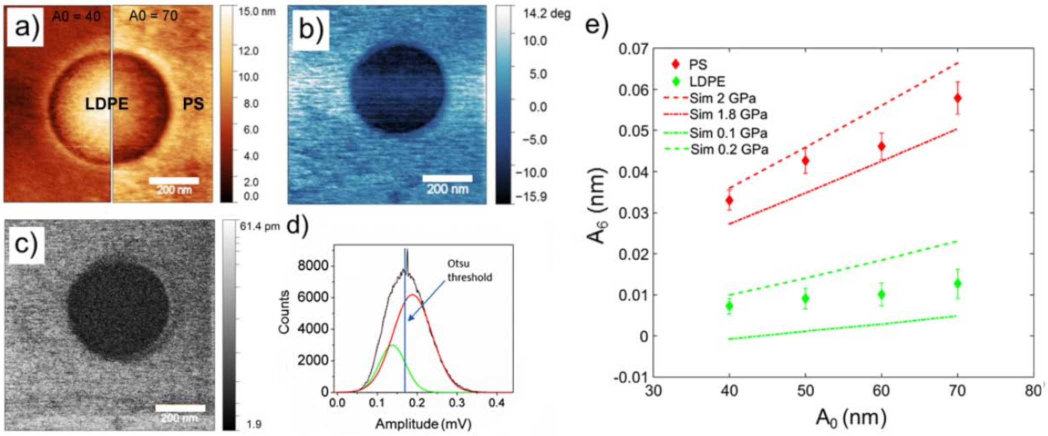

Figure 5.2: PS-LDPE sample: (a) topography at $A_0 = 40\,\mathrm{nm}$ (left) and $A_0 = 470\,\mathrm{nm}$ (right), (b) phase of the fundamental mode and (c) A_6 channel images at $A_0 = 70\,\mathrm{nm}$. As A_0 increases, the force exerted induces an increased deformation in the sample, as visible in the comparison of the two topographies. (d) Example of distribution of the A6 channel with a Gaussian fit for both LDPE (continuos green line) and PS (continuos red line) contributions, the vertical blue line representing the Otsu mask threshold value [Otsu, 1979] (see text for details). (e) Plot of experimentally determined A_6 values for different A_0 values (green diamonds for LDPE and red diamonds for PS) and corresponding simulations for LDPE (discontinuous green lines) and PS (continuous red lines). The experimental values lie in the given indetermination interval of sample Young's modulus.

5.4.2 PS-b-PMMA

The second type of sample investigated was a PS-b-PMMA self-assembled film with vertical lamellae and with a 37 nm pitch. The topography and phase images of this sample, measured at $A_0 = 70\,\mathrm{nm}$, are shown in Figureure 5.3a and b, respectively, showing a characteristic fingerprint distribution. In the topography image the two phases are distinguishable: PS and PMMA correspond to the darker and brighter parts, respectively, due to the different stiffness. The good contrast observed in Figure 5.3a and b is also visible in the A_6 channel (Figure 5.3c), which reliably replicates the topography and phase images. The E values of the two phases of this sample had been measured previously [Lorenzoni et al., 2015b] by PeakForce quantitative nanomechanical mapping (QNM), enabling a comparison of the two methods. The E values obtained here for PS and PMMA are $1.97 \pm 0.21\,\mathrm{GPa}$ and $3.10 \pm 0.73\,\mathrm{GPa}$, respectively. The simulation shown in Figure 5.3d shows a good agreement between the experimental values matching the results previously obtained with QNM technique [Lorenzoni et al., 2015b]. The experimental results lay between the simulations performed for $E = 1.6\,\mathrm{GPa}$ and $2\,\mathrm{GPa}$ for PS and $2.4\,\mathrm{GPa}$ and $3\,\mathrm{GPa}$ for the PMMA, respectively, within the indetermination on the QNM results. However, the A_6 values at $A0 = 80\,\mathrm{nm}$ become less reliable; at this free amplitude the surface of the sample started to deform plastically. Notwithstanding the lower difference of Young modulus ($\Delta E \approx 1\,\mathrm{GPa}$) and the small dimensions of

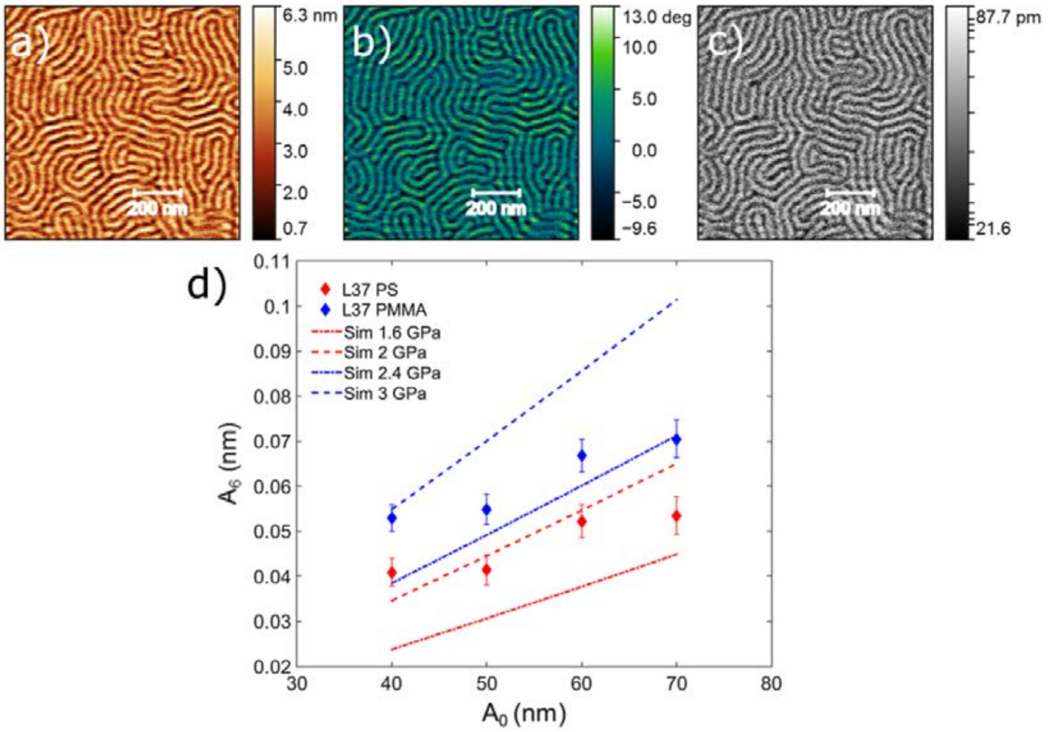

Figure 5.3: PS-b-PMMA sample: (a) topography, (b) phase and (c) A_6 channel images taken at A_0 =70 nm. (d) Plot of experimentally determined A_6 values for different A_0 values (red diamonds for PS and blue diamonds for PMMA) and corresponding simulations for PS (discontinuous red lines) and PMMA (continuous blue lines). The experimental values lie in the given indetermination interval of sample Young's modulus.

the block copolymers phases (18 nm), we obtained a good contrast that allows both the discrimination of both phases and a quantitative estimation of the corresponding E values. Another parameter that has an important effect on evolution of A_6 is the tip radius, as has been previously discussed [Fraxedas et al., 2015, Gramazio et al., 2017]. In this case A_6 increases monotonically for increasing R values, hence it becomes mandatory the monitoring of the evolution of R. In our case we have compared the topographies of the first image of the experiments ($A_0 = 40$ nm) with the last one, after 5 images ($A_0 = 70$ nm). Figure 5.4 shows the comparison of the corresponding cross sections where no significant change is observed. We can thus conclude that in this case the tip radius was constant so that the increase of A_6 can be safely attributed to the increase in A_0 and not to changes in R.

5.4.3 PS-b-PMMA with modified PMMA by SIS

The third kind of sample was a PS-b-PMMA self-assembled film with vertical lamellae and pitch of 37 nm, exposed to SIS treatment in order to induce an increase of the stiffness of the PMMA phase. The use of SIS process is very interesting for pattern transfer: the infiltered phase becomes more resistant to etching, and in par-

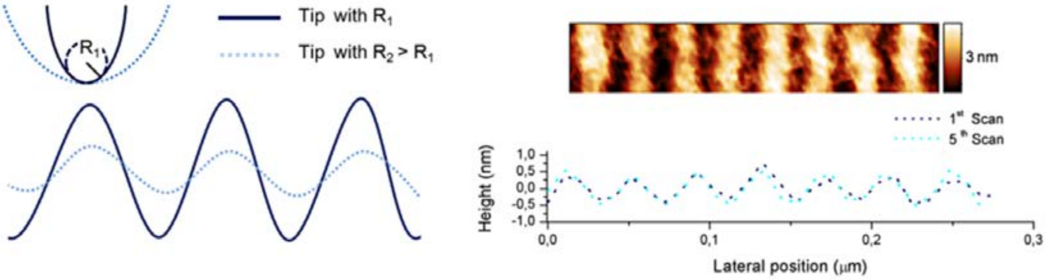

Figure 5.4: (Left) expected influence of tip blunting on AFM height profile. Scanning at constant load vertical lamellar BCPs produces a certain topographical contrast between the two blocks. As the tip radius increases convolution effects tend to mask such height difference. (Right) in the case of 5 consequent scans at A_0 =40 nm to 70 nm and A_{sp} = 50% of A_0, no relevant change in the averaged profile of parallel lamellas is observed, thus deducting no significant tip blunting has occurred.

ticular, the etching selectivity with silicon increases, allowing to increase the final aspect ratio of the transferred features. However, it is also important to ensure that the infiltered blocks have good mechanical properties, to avoid collapsing of the infiltered features when the non infiltered block is removed. Previous measurements of the E value of infiltered PS-b-PMMA was measured by QNM [Lorenzoni et al., 2015b], obtaining a value of 3.6 ± 0.4 GPa for the PMMA phase. Using higher harmonic detection, we obtain the same information but with standard dynamic mode AFM imaging conditions and at lower surface deformation. The morphology of the fingerprint patterns does not change after the SIS cycles (Figures 5.5a and b). Images of the A_6 channel (Figures 5.5c and d) show that the resolution and the contrast are good and allow the two phases to be distinguished. The analysis using VEDA simulations (Figure 5.5e) indicates that the E values for the PMMA lay between 3 GPa and 3.6 GPa, while those for the PS increases compared with the pristine PS-b-PMMA sample and lay above the simulation with $E = 2$ GPa, in accordance with the results obtained with QNM. It is then confirmed that the A_6 detection method presents sufficient sensitivity to detect changes of Young's modulus of around 0.5 GPa.

5.5 Conclusions

We have developed a method to determine the Young's moduli of nanostructured materials based on standard AFM tapping mode cantilever and easily available electronics. Under the same imaging conditions usually employed in dynamic AFM mode, we were able to reliably measure the amplitude of 6^{th} higher harmonic of the first resonance mode at free oscillation amplitudes of 40 nm to 80 nm. VEDA simulations were used to analyse the dependence of imaging parameters on the values of the higher harmonics and surface properties, paving the way to select the

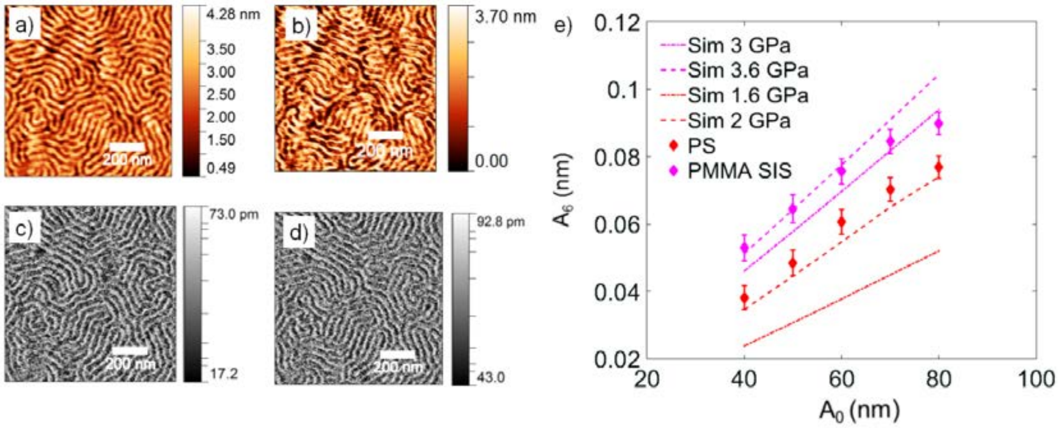

Figure 5.5: PS-b-PMMA sample with modified PMMA by SIS: topography at (a) $A_0 = 40\,\text{nm}$ and (b) $A_0 = 70\,\text{nm}$ and A_6 channel images at (c) $A_0 = 40\,\text{nm}$ and (d) at $A_0 = 70\,\text{nm}$. (e) Plot of experimentally determined A_6 values for different A_0 values (red diamonds for PS and magenta diamonds for infiltrated PMMA) and corresponding simulations for PS (discontinuous red lines) and infiltrated PMMA (continuous magenta lines). Infiltrated phase experimental values match with simulation while non-infiltrated PS phase shows an offset, indicating an apparent higher modulus of PS.

proper conditions to optimize the measurements. We have obtained a good match between simulations and experimental values for polymeric samples in the low GPa range (2 GPa to 4 GPa) scanned at high resolution, resolving features down to 17 nm width. Specifically, lamellar block copolymers with nominal pitch of 37 nm were characterized using the 6th higher harmonic detection method. The results are in accordance with those reported by other methods such as PeakForce QNM, force reconstruction or nanomechanical spectroscopy, and with a comparable uncertainty. Moreover, simulations indicate that there is no need to use different tips for different ranges of Young modulus as required with PeakForce and Force volume techniques. Using a standard set-up has the advantage of analyzing the direct signal of the photodiode (amplitude of 6^{th} higher harmonic) and all the characteristics mentioned above, thus making it a possible alternative or a valid complement to other nanomechanical measuring approaches. Future improvements of our method should include more realistic approximations of the cantilever dynamics and of the viscoelastic response of the surface [López-Guerra and Solares, 2014].

5.6 Acknowledgements

This work was performed within the aim4np project, which was supported by the EC through a grant (contract Nr. 309558) within the 7th Frame-work Program and within the framework of the PhD program in Physics of the Autonomous University of Barcelona. The ICN2 is funded by the CERCA programme/Generalitat de

Catalunya. The ICN2 is supported by the Severo Ochoa programme of the Spanish Ministry of Economy, Industry and Competitiveness (MINECO, grant no. SEV-2013-0295). Laura Evangelio acknowledges the Ministry of Education of Spain for her FPU grant (FPU 13/03746). All polymeric materials have been supplied by Arkema. Additional financial support from Nanointegra project (TEC2015- 69864-R) is also acknowledged.

Chapter 6

Conclusions

In summary, during this thesis we have explored the possibility of employing the dependence of higher harmonics amplitude signal on several experimental parameters in the developing of a fast and easy AFM-based method for the monitoring of the tip radius and the quantification of Young's modulus.

First, we have observed both experimentally and by means of simulations that the amplitude of the 6^{th} harmonic (A_6) increases for increasing R values following a power law function and that this increase becomes more patent for smaller tip radii (below 20 nm). This allows the simultaneous acquisition of topographic and higher harmonic images thus continuously controlling the state of the tip. Unfortunately, the monitoring of the state of the tip is still qualitative at this stage. In order to obtain quantitative results, it was necessary a deeper knowledge of the 6^{th} higher harmonic amplitude behaviour depending on the several experimental parameters that it has to take into account during AFM experiments of this kind.

The first results convinced us to start a systematic study of the dependence of the 6^{th} harmonic of rectangular cantilevers on the tip radius, sample's Young's modulus, free oscillation amplitude and cantilever force constant. The 6^{th} harmonic has been chosen because it is in close resonance with the 2^{nd} flexural mode, leading to observable signals, and because its frequency is within the reach of the control electronics used in the experiments. The study was managed comparing numerical simulations, using the VEDA code, with the experimental results obtained in the same conditions used in the simulations. The outcome of the simulations is that the 6^{th} harmonic can be analytically expressed by the product of four identical decoupled gun-shaped functions, each one associated with a specific parameter and with its own coefficients. Thus, the partial evolution for a particular parameter can be traced using this universal behaviour. The simulations have been validated with AFM experiments using rectangular cantilevers in the $3\,\mathrm{N\,m^{-1}}$ to $45\,\mathrm{N\,m^{-1}}$ range and different samples in the 2 GPa to 345 GPa range. The predicted trends are well reproduced by the experiments. As we can notice from the different trends, the 6^{th} harmonic is most sensitive to changes in tip radius for values of tip radius below ca. 10 nm and Young modulus below ca. 20 GPa. If we consider the method for implementing tip radius real time monitoring, this will be more effective when sharp (new) tips are imaging stiff samples. Instead, in order to measure the surface Young modulus the modelling shows that the best results will be obtained using larger tip radius (10 nm to 15 nm) in order to have an almost constant radius-dependent contribution. In order to obtain trustworthy predictions, a more precise and more accurate calibration of the cantilever is still necessary. The performed simulations might also be improved including parameters which could be varied and measured experimentally in order to refine the method and make the results of the simulations more comparable to the experimental ones. The mathematical tool that we have presented based on gun-shaped functions allows to identify the optimal conditions to obtain information about the properties of materials from the harmonic response in non-contact dynamic modes.

The next step, and a goal of this work was to obtain quantitative information. Under the same imaging conditions usually employed in dynamic AFM mode, we have been able to reliably measure the amplitude of 6^{th} higher harmonic of the first resonance mode at free oscillation amplitudes of 40 nm to 80 nm. VEDA simulations were used to analyse the dependence of imaging parameters on the values of the higher harmonics and surface properties, paving the way to select the proper conditions to optimize the measurements. We have obtained a good match between simulations and experimental values for polymeric samples in the low GPa range (2 GPa to 4 GPa) scanned at high resolution, resolving features down to 17 nm width. Specifically, lamellar block copolymers with nominal pitch of 37 nm were characterized using the 6th higher harmonic detection method. The results are in accordance with those reported by other methods such as PeakForce QNM, force reconstruction or nanomechanical spectroscopy, and with a comparable uncertainty. Moreover, simulations indicate that there is no need to use different tips for different ranges of Young modulus as required with PeakForce and Force volume techniques. Using a standard set-up has the advantage of analysing the direct signal of the photodiode (amplitude of 6^{th} higher harmonic) and all the characteristics mentioned above, thus making it a possible alternative or a valid complement to other nanomechanical measuring approaches.

Definitively, this work of thesis can be considered a preliminary study about a better comprehension of the higher harmonic amplitude signal and about the development of a quantitative technique employing a simple and commercial set-up. Future improvements of our method should include a preciser calibration of the cantilever parameters and more realistic approximations of the cantilever dynamics and of the viscoelastic response of the surface.

Bibliography

[Abraham, 1978] Abraham, F. F. (1978). The interfacial density profile of a Lennard-Jones fluid in contact with a (100) Lennard-Jones wall and its relationship to idealized fluid/wall systems: A Monte Carlo simulation. *The Journal of Chemical Physics*, 68(8):3713–3716.

[Albrecht et al., 1990] Albrecht, T. R., Akamine, S., Carver, T. E., and Quate, C. F. (1990). Microfabrication of cantilever styli for the atomic force microscope. *Journal of Vacuum Science & Technology A: Vacuum, Surfaces, and Films*, 8(4):3386–3396.

[Ando, 2000] Ando, Y. (2000). Y. Ando - 2000 - The effect of relative humidity on friction and pull-off forces measured on submicron-size asperity arrays.pdf. *Wear*, 238:12–19.

[Ata et al., 2002] Ata, A., Rabinovich, Y. I., and Singh, R. (2002). Role of surface roughness in capillary adhesion. *Journal of adhesion science and technology*, 16(4):337–346.

[Atamny and Baiker, 1995] Atamny, F. and Baiker, A. (1995). Direct imaging of the tip shape by AFM. *Surface Science*, 323(3).

[Balantekin and Atalar, 2005] Balantekin, M. and Atalar, A. (2005). Enhancing higher harmonics of a tapping cantilever by excitation at a submultiple of its resonance frequency. *Physical Review B - Condensed Matter and Materials Physics*, 71(12):1–6.

[Balooch et al., 2005] Balooch, G., Balooch, M., Nalla, R. K., Schilling, S., Filvaroff, E. H., Marshall, G. W., Marshall, S. J., Ritchie, R. O., Derynck, R., and Alliston, T. (2005). TGF-beta regulates the mechanical properties and composition of bone matrix. *Proceedings of the National Academy of Sciences of the United States of America*, 102(52):18813–18818.

[Balooch et al., 2004] Balooch, G., Marshall, G. W., Marshall, S. J., Warren, O. L., Asif, S. A. S., and Balooch, M. (2004). Evaluation of a new modulus mapping technique to investigate microstructural features of human teeth. *Journal of Biomechanics*, 37(8):1223–1232.

[Banks et al., 2011] Banks, H. T., Hu, S., and Kenz, Z. R. (2011). A brief review of elasticity and viscoelasticity for solids. *Advances in Applied Mathematics and Mechanics*, 3(1):1–51.

[Bar et al., 1997] Bar, G., Thomann, Y., Brandsch, R., Cantow, H. J., and Whangbo, M. H. (1997). Factors Affecting the Height and Phase Images in Tapping Mode Atomic Force Microscopy. Study of Phase Separated Polymer Blends of Poly(ethene-co-styrene) and Poly(2,6-dimethyl-1,4-phenylene oxide). *Langmuir*, 13(3):3807–3812.

[Barthel, 2008] Barthel, E. (2008). Adhesive elastic contacts: JKR and more. *Journal of Physics D: Applied Physics*, 41(16).

[Bassani and D'Acunto, 2000] Bassani, R. and D'Acunto, M. (2000). Nanotribology: Tip-sample wear under adhesive contact. *Tribology International*, 33(7):443–452.

[Bates and Fredrickson, 1990] Bates, F. S. and Fredrickson, G. H. (1990). Block Copolymer Thermodynamics: Theory and Experiment. *Annual Review of Physical Chemistry*, 41:525–557.

[Beach et al., 2002] Beach, E. R., Tormoen, G. W., Drelich, J., and Han, R. (2002). Pull-off force measurements between rough surfaces by atomic force microscopy. *Journal of Colloid and Interface Science*, 247(1):84–99.

[Berg and Briggs, 1997] Berg, J. and Briggs, G. A. D. (1997). Nonlinear dynamics of intermittent-contact mode atomic force microscopy. *Physical Review B*, 55(22):14899–14908.

[Bhushan and Dandavate, 2000] Bhushan, B. and Dandavate, C. (2000). Thin-film friction and adhesion studies using atomic force microscopy. *Journal of Applied Physics*, 87(3):1201–1210.

[Bhushan and Koinkar, 1994] Bhushan, B. and Koinkar, V. N. (1994). Nanoindentation hardness measurements using atomic force microscopy. *Applied Physics Letters*, 64(13):1653–1655.

[Binnig and Quate, 1986] Binnig, G. and Quate, C. F. (1986). Atomic Force Microscope. *Physical Review Letters*, 56(9):930–933.

[Biswas et al., 2014] Biswas, M., Libera, J. A., and Darling, S. B. (2014). New Insight into the Mechanism of Sequential Infiltration Synthesis from Infrared Spectroscopy. *Chemistry of Materials*, 26:6135–6141.

[Biswas et al., 2015] Biswas, M., Libera, J. A., and Darling, S. B. (2015). Kinetics for the Sequential Infiltration Synthesis of Alumina in Poly(methyl methacrylate):

An Infrared Spectroscopic Study. *The Journal of Physical Chemistry C*, 119:14585–14592.

[Bocquet and Barrat, 1993] Bocquet, L. and Barrat, J. L. (1993). Hydrodynamic boundary conditions and correlation functions of confined fluids. *Physical Review Letters*, 70(18):2726–2729.

[Burgo et al., 2012] Burgo, T. A., Ducati, T. R., Francisco, K. R., Clinckspoor, K. J., Galembeck, F., and Galembeck, S. E. (2012). Triboelectricity: Macroscopic charge patterns formed by self-arraying ions on polymer surfaces. *Langmuir*, 28(19):7407–7416.

[Burgo et al., 2013] Burgo, T. A. L., Silva, C. A., Balestrin, L. B. S., and Galembeck, F. (2013). Friction coefficient dependence on electrostatic tribocharging. *Scientific Reports*, 3:1–8.

[Burnham and Colton, 1989] Burnham, N. A. and Colton, R. J. (1989). Measuring the nanomechanical properties and surface forces of materials using an atomic force microscope. *Journal of Vacuum Science & Technology A: Vacuum, Surfaces, and Films*, 7(4):2906–2913.

[Burnham et al., 1993] Burnham, N. A., Colton, R. J., and Pollock, H. M. (1993). Interpretation of force curves in force microscopy. *Nanotechnology*, 4(2):64–80.

[Burnham and Kulik, 1999] Burnham, N. A. and Kulik, A. J. (1999). Handbook of Micro Nanotribology. chapter Surface fo. CRC Press.

[Bushell et al., 2011] Bushell, G. R., Watson, G. S., Holt, S. A., and Myhra, S. (2011). Imaging and nano-dissection of tobacco mosaic virus by atomic force microscopy. *Journal of Microscopy*, 180(2):174–181.

[Bustamante et al., 1992] Bustamante, C., Vesenka, J., Tang, C. L., Rees, W., Guthold, M., and Keller, R. (1992). Circular DNA molecules imaged in air by scanning force microscopy. *Biochemistry*, 31(1):22–26.

[Butt et al., 1992] Butt, H., Siedle, P., Seifert, K., Fendler, K., Seeger, T., Bamberg, E., and Weisenhorn, A. L. (1992). Scan speed limit in atomic force microscopy. *Journal of Micro*, 169:75–84.

[Butt et al., 2005] Butt, H. J., Cappella, B., and Kappl, M. (2005). Force measurements with the atomic force microscope: Technique, interpretation and applications. *Surface Science Reports*, 59(1-6):1–152.

[Butt and Jaschke, 1995] Butt, H. J. and Jaschke, M. (1995). Calculation of thermal noise in atomic force microscopy. *Nanotechnology*, 6(1):1.

[Calabri et al., 2008] Calabri, L., Pugno, N., Menozzi, C., and Valeri, S. (2008). AFM nanoindentation: Tip shape and tip radius of curvature effect on the hardness measurement. *Journal of Physics Condensed Matter*, 20(47).

[Cappella, 2016] Cappella, B. (2016). *Mechanical Properties of Polymers Measured through AFM Force-Distance Curves*.

[Cappella and Dietler, 1999] Cappella, B. and Dietler, G. (1999). Force-distance curves by atomic force microscopy. *Surface Science Reports*, 34(1-3):1–104.

[Carpick and Salmeron, 1997] Carpick, R. W. and Salmeron, M. (1997). Scratching the surface: Fundamental investigations of tribology with atomic force microscopy. *Chemical Reviews*, 97(4):1163–1194.

[Cheng et al., 2010] Cheng, S., Luan, B., and Robbins, M. O. (2010). Contact and friction of nanoasperities: Effects of adsorbed monolayers. *Physical Review E - Statistical, Nonlinear, and Soft Matter Physics*, 81(1):1–17.

[Choi et al., 2004] Choi, Y., Lee, H. S., and Kwon, D. (2004). Analysis of sharp-tip-indentation load-depth curve for contact area determination taking into account pile-up and sink-in effects. *Journal of Materials Research*, 19(11):3307–3315.

[Chon et al., 2000] Chon, J. W. M., Mulvaney, P., and Sader, J. E. (2000). Experimental validation of theoretical models for the frequency response of atomic force microscope cantilever beams immersed in fluids. *Journal of Applied Physics*, 87(8):3978–3988.

[Chou et al., 1996] Chou, S. Y., Krauss, P. R., and Renstrom, P. J. (1996). Imprint Lithography Nanometer Resolution. *Science*, 272(5258):85–87.

[Chyasnavichyus et al., 2015] Chyasnavichyus, M., Young, S. L., and Tsukruk, V. (2015). Recent advances in micromechanical characterization of polymer, biomaterial, and cell surfaces with atomic force microscopy. *Japanese Journal of Applied Physics*, 54(8).

[Cleveland et al., 1998] Cleveland, J. P., Anczykowski, B., Schmid, a. E., and Elings, V. B. (1998). Energy dissipation in tapping-mode atomic force microscopy. *Applied Physics Letters*, 72(20):2613.

[Cleveland and Bocek, 1993] Cleveland, J. P. and Bocek, D. (1993). A nondestructive method for determining the spring constant of cantilevers for scanning force microscopy. *Review of Scientific Instruments*, 64(2):403–405.

[Cooper et al., 2000] Cooper, K., Ohler, N., Gupta, A., and Beaudoin, S. (2000). Analysis of contact interactions between a rough deformable colloid and a smooth substrate. *Journal of Colloid and Interface Science*, 222(1):63–74.

[Costa and Yin, 1999] Costa, K. D. and Yin, F. C. P. (1999). Analysis of Indentation: Implications for Measuring Mechanical Properties With Atomic Force Microscopy. *Journal of Biomechanical Engineering*, 121(5):462.

[de Lazzer et al., 1999] de Lazzer, A., Dreyer, M., and Rath, H. J. (1999). Particle-Surface Capillary Forces. *Langmuir*, 15(13):4551–4559.

[Derjaguin, 1934] Derjaguin, B. V. (1934). Untersuchungen über die Reibung und Adhäsion, IV - Theorie des Anhaftens kleiner Teilchen. *Kolloid-Zeitschrift*, 69(2):155–164.

[Derjaguin and Landau, 1993] Derjaguin, B. V. and Landau, L. (1993). Theory of the stability of strongly charged lyophobic sols and of the adhesion of strongly charged particles in solutions of electrolytes. *Progress in Surface Science*, 43(1-4):30–59.

[Derjaguin et al., 1975] Derjaguin, B. V., Muller, V. M., and Toporov, Y. P. (1975). Effect of Contact Deformations on the Adhesion of Particles. *Journal of Colloid and Interface Science*, 53(2):314 – 326.

[Dong et al., 2009] Dong, M., Husale, S., and Sahin, O. (2009). Determination of protein structural flexibility by microsecond force spectroscopy. *Nature Nanotechnology*, 4(8):514–517.

[Ducker et al., 1991] Ducker, W. A., Senden, T. J., and Pashley, R. M. (1991). Direct measurement of colloidal forces using an atomic force microscope. *Nature*, 353(6341):239–241.

[Dürig, 2000] Dürig, U. (2000). Interaction sensing in dynamic force microscopy. *New Journal of Physics*, 2(5):1 – 12.

[Dzyaloshinskii et al., 1961] Dzyaloshinskii, I. E., Lifshitz, E. M., and Pitaevskii, L. P. (1961). The general theory of van der Waals forces. *Advances in Physics*, 10(38):165–209.

[Ebenstein and Wahl, 2006] Ebenstein, D. M. and Wahl, K. J. (2006). Anisotropic nanomechanical properties of Nephila clavipes dragline silk. *Journal of Materials Research*, 21(8):2035–2044.

[Eichenlaub et al., 2004] Eichenlaub, S., Gelb, A., and Beaudoin, S. (2004). Roughness models for particle adhesion. *Journal of Colloid and Interface Science*, 280(2):289–298.

[Eslami et al., 2014] Eslami, B., Ebeling, D., and Solares, S. D. (2014). Trade-offs in sensitivity and sampling depth in bimodal atomic force microscopy and comparison to the trimodal case. *Beilstein Journal of Nanotechnology*, 5(1):1144–1151.

[Evans and Parry, 1990] Evans, R. and Parry, A. O. (1990). Liquids at interfaces: What can a theorist contribute? *Journal of Physics: Condensed Matter*, 2:SA15–SA32.

[Fernandez-Regulez et al., 2014] Fernandez-Regulez, M., Evangelio, L., Lorenzoni, M., Fraxedas, J., and Perez-Murano, F. (2014). Sub-10 nm resistless nanolithography for directed self-assembly of block copolymers. *ACS Applied Materials & Interfaces*, 6(23):21596–21602.

[Fraxedas et al., 2002] Fraxedas, J., Garcia-Manyes, S., Gorostiza, P., and Sanz, F. (2002). Nanoindentation: Toward the sensing of atomic interactions. *Proceedings of the National Academy of Sciences*, 99(8):5228–5232.

[Fraxedas et al., 2015] Fraxedas, J., Pérez-Murano, F., Gramazio, F., Lorenzoni, M., Rull Trinidad, E., and Staufer, U. (2015). Continuous monitoring of tip radius during atomic force microscopy imaging. In *Scanning Microscopies*, volume 9636, pages 96360O–1.

[Fraxedas et al.,] Fraxedas, J., Perez-Murano, F., Rull Trinidad, E., and Staufer, U. Patent pending.

[Fuji et al., 1998] Fuji, M., Machida, K., Takei, T., Watanabe, T., and Chikazawa, M. (1998). Effect of Surface Geometric Structure on the Adhesion Force between Silica Particles. *The Journal of Physical Chemistry B*, 102(44):8782–8787.

[Fuji et al., 1999] Fuji, M., Machida, K., Takei, T., Watanabe, T., and Chikazawa, M. (1999). Effect of wettability on adhesion force between silica particles evaluated by atomic force microscopy measurement as a function of relative humidity. *Langmuir*, 15(13):4584–4589.

[Fukuma et al., 2006] Fukuma, T., Kilpatrick, J. I., and Jarvis, S. P. (2006). Phase modulation atomic force microscope with true atomic resolution. *Review of Scientific Instruments*, 77(12).

[Gadelrab et al., 2013] Gadelrab, K., Santos, S., Font, J., and Chiesa, M. (2013). Single cycle and transient force measurements in dynamic atomic force microscopy. *Nanoscale*, 5(22):10776.

[Gady et al., 1997] Gady, B., Reifenberger, R., Rimai, D. S., and DeMejo, L. P. (1997). Contact Electrification and the Interaction Force between a Micrometer-Size Polystyrene Sphere and a Graphite Surface. *Langmuir*, 13(9):2533–2537.

[Galileo, 1952] Galileo, G. (1952). *Dialogues Concerning Two New Sciences*. William Andrew Publishing.

[Ganor and Shilo, 2006] Ganor, Y. and Shilo, D. (2006). High sensitivity nanoscale mapping of elastic moduli. *Applied Physics Letters*, 88(23):23–26.

[Garcia, 2002] Garcia, R. (2002). Dynamic atomic force microscopy methods. *Surface Science Reports*, 47(6-8):197–301.

[Garcia, 2010] Garcia, R. (2010). *Amplitude Modulation Atomic Force Microscopy*. Wiley-VCH.

[Garcia and Herruzo, 2012] Garcia, R. and Herruzo, E. T. (2012). The emergence of multifrequency force microscopy. *Nature Nanotechnology*, 7(4):217–226.

[Garcia and Proksch, 2013] Garcia, R. and Proksch, R. (2013). Nanomechanical mapping of soft matter by bimodal force microscopy. *European Polymer Journal*, 49(8):1897–1906.

[Garcia and San Paulo, 1999] Garcia, R. and San Paulo, A. (1999). Attractive and repulsive tip-sample interaction regimes in tapping-mode atomic force microscopy. *Physical Review B*, 60(7):4961–4967.

[Giessibl, 2003] Giessibl, F. J. (2003). Advances in atomic force microscopy. *Reviews of Modern Physics*, 75(3):949–983.

[Giessibl, 2006] Giessibl, F. J. (2006). Higher-Harmonic atomic force microscopy. *Surface and Interface Analysis*, 38:1696 – 1701.

[Glasbey et al., 1994] Glasbey, T. O., Batts, G. N., Davies, M. C., Jackson, D. E., Nicholas, C. V., Purbrick, M. D., Roberts, C. J., Tendler, S. J. B., and Williams, P. M. (1994). The use of a polymer film to estimate AFM probe profile. *Surface Science*, 318(3).

[Gómez-Monivas et al., 2001] Gómez-Monivas, S., Froufe-Pérez, L. S., Caamaño, A. J., and Sáenz, J. J. (2001). Electrostatic forces between sharp tips and metallic and dielectric samples. *Applied Physics Letters*, 79(24):4048–4050.

[Gotsmann and Lantz, 2008] Gotsmann, B. and Lantz, M. A. (2008). Atomistic wear in a single asperity sliding contact. *Physical Review Letters*, 101(12):1–4.

[Gramazio et al., 2018] Gramazio, F., Lorenzoni, M., Pérez-Murano, F., Evangelio, L., and Fraxedas, J. (2018). Quantification of nanomechanical properties of surfaces by higher harmonic monitoring in amplitude modulated AFM imaging. *Ultramicroscopy*, 187:20–25.

[Gramazio et al., 2017] Gramazio, F., Lorenzoni, M., Pérez-Murano, F., Rull Trinidad, E., Staufer, U., and Fraxedas, J. (2017). Functional dependence of resonant harmonics on nanomechanical parameters in dynamic mode atomic force microscopy. *Beilstein Journal of Nanotechnology*, 8:883–891.

[Greenwood and Johnson, 1981] Greenwood, J. A. and Johnson, K. L. (1981). The mechanics of adhesion of viscoelastic solids. *Philosophical Magazine A: Physics of Condensed Matter, Structure, Defects and Mechanical Properties*, 43(3):697–711.

[Griffith et al., 1991] Griffith, J. E., Grigg, D. A., Vasile, M. J., Russell, P. E., and Fitzgerald, E. A. (1991). Characterization of scanning probe microscope tips for linewidth measurement. *Journal of Vacuum ...*, 9(6):3586.

[Hamaker, 1937] Hamaker, H. C. (1937). The London-Van der Waals attraction between spherical particles. *Physica IV*, 10:1058–1072.

[Hao et al., 1991] Hao, H. W., Baro, A. M., and Saenz, J. J. (1991). Electrostatic and contact forces inforce microscopy. *Journal of Vacuum Science & Technology B Microelectronics and Nanometer Structures Processing, Measurement, and Phenomena*, 9(2):1323–1328.

[Hartmann, 1990] Hartmann, U. (1990). Manifestation of zero-point quantum fluctuations in atomic froce microscopy. *Physical Review B*, 42(3):1541–1546.

[Heim et al., 2004] Heim, L., Kappl, M., and Butt, H. J. (2004). Tilt of Atomic Force Microscope Cantilevers: Effect on Friction Measurements. *Langmuir*, 20:2760–2764.

[Hembacher et al., 2004] Hembacher, S., Giessibl, F. J., and Mannhart, J. (2004). Force Microscopy with Light Atom Probes. *Science*, 305(2004):380–383.

[Herruzo et al., 2014] Herruzo, E. T., Perrino, A. P., and Garcia, R. (2014). Fast nanomechanical spectroscopy of soft matter. *Nature communications*, 5:3126.

[Hertz, 1882] Hertz, H. (1882). lieber die Berührung fester elastischer Körper. *J. Reine Angew. Math*, 92:156–171.

[Hinsberg et al., 2010] Hinsberg, W., Cheng, J., Kim, H. C., and Sanders, D. P. (2010). Self-assembling materials for lithographic patterning: overview, status, and moving forward. *Spie*, 7637:76370G–11.

[Horn and Israelachvili, 1981] Horn, R. G. and Israelachvili, J. N. (1981). Direct measurement of structural forces between two surfaces in a nonpolar liquid. *The Journal of Chemical Physics*, 75(3):1400–1411.

[Hu and Raman, 2007] Hu, S. and Raman, A. (2007). Analytical formulas and scaling laws for peak interaction forces in dynamic atomic force microscopy. *Applied Physics Letters*, 91(12):2005–2008.

[Hussain et al., 2017] Hussain, D., Ahmad, K., Song, J., and Xie, H. (2017). Advances in the atomic force microscopy for critical dimension metrology. *Measurement Science and Technology*, 28(1):12001.

[Hutter, 2005] Hutter, J. L. (2005). Comment on Tilt of Atomic Force Microscopy Cantilevers. *Langmuir*, 21:2630–2632.

[Hutter and Bechhoefer, 1993] Hutter, J. L. and Bechhoefer, J. (1993). Calibration of Atomic-Force Microscope Tips. *Review of Scientific Instruments*, 64(11):3342.

[Israelachvili, 2011] Israelachvili, J. N. (2011). *Intermolecular and Surface Forces*. Elsevier, 3rd edition.

[Israelachvili and Pashley, 1983] Israelachvili, J. N. and Pashley, R. M. (1983). Molecular layering of water at surfaces and origin of repulsive hydration forces.

[Israelachvili and Ruths, 2013] Israelachvili, J. N. and Ruths, M. (2013). Brief history of intermolecular and intersurface forces in complex fluid systems. *Langmuir*, 29(31):9605–9619.

[Israelachvili and Tabor, 1972] Israelachvili, J. N. and Tabor, D. (1972). The Measurement of Van Der Waals Dispersion Forces in the Range 1.5 to 130 nm. *Proceedings of the Royal Society A: Mathematical, Physical and Engineering Sciences*, 331(1584):19–38.

[Jammer, 1957] Jammer, M. (1957). *Concepts of Force: A Study in the Foundations of Dynamics*. Harvard University Press.

[Jensen, 1993] Jensen, F. (1993). Z Calibration of the Atomic Force Microscope By Means of a Pyramidal Tip. *Review of Scientific Instruments*, 64(9):2595–2597.

[Johnson, 1985] Johnson, K. L. (1985). *Contact mechanics*. Cambridge University Press.

[Johnson and Greenwood, 1997] Johnson, K. L. and Greenwood, J. A. (1997). An Adhesion Map for the Contact of Elastic Spheres. *Journal of Colloid and Interface Science*, 333(192):326–333.

[Johnson et al., 1971] Johnson, K. L., Kendall, K., and Roberts, A. D. (1971). Surface Energy and the Contact of Elastic Solids. *Proceedings of the Royal Society A: Mathematical, Physical and Engineering Sciences*, 324(1558):301–313.

[Jones et al., 2002] Jones, R., Pollock, H. M., Cleaver, J. A. S., and Hodgest, C. S. (2002). Adhesion Forces between Glass and Silicon Surfaces in Air Studied by AFM : Effects of Relative Hunidity , Particle Size, Roughness, and Surface Treatment. *Langmuir*, 18:8045–8055.

[Killgore et al., 2011] Killgore, J. P., Geiss, R. H., and Hurley, D. C. (2011). Continuous measurement of atomic force microscope tip wear by contact resonance force microscopy. *Small*, 7(8):1018–1022.

[Kim et al., 2009] Kim, K.-S., Wang, H., and Zou, Q. (2009). High speed force-volume mapping using atomic force microscope. *2009 American Control Conference*, m:991–996.

[Kiracofe et al., 2012] Kiracofe, D., Melcher, J., and Raman, A. (2012). Gaining insight into the physics of dynamic atomic force microscopy in complex environments using the VEDA simulator. *Review of Scientific Instruments*, 83(83):013702.

[Kiracofe and Raman, 2010] Kiracofe, D. and Raman, A. (2010). On eigenmodes, stiffness, and sensitivity of atomic force microscope cantilevers in air versus liquids. *Journal of Applied Physics*, 107(3):033506.

[Kiracofe and Raman, 2011] Kiracofe, D. and Raman, A. (2011). Quantitative force and dissipation measurements in liquids using piezo-excited atomic force microscopy: a unifying theory. *Nanotechnology*, 22(48):485502.

[Klein and McEuen, 1995] Klein, D. L. and McEuen, P. L. (1995). Conducting atomic force microscopy of alkane layers on graphite. *Applied Physics Letters*, 66(19):2478.

[Knoop et al., 1939] Knoop, F., Peters, C., and Emerson, W. (1939). A sensitive pyramidal-diamond tool for indentation measurements. *Journal of Research of the National Bureau of Standards*, 23(1):39.

[Koops et al., 2015] Koops, R., Van Veghel, M., and Van De Nes, A. (2015). A dedicated calibration standard for nanoscale areal surface texture measurements. *Microelectronic Engineering*, 141:250–255.

[Lambert and Regnier, 2010] Lambert, P. and Regnier, S. (2010). *Microworld Modeling in Vacuum and Gaseous Environments*. John Wiley & Sons.

[Langbein, 1973] Langbein, D. (1973). The macroscopic theory of van der Waals attraction. *Solid State Communications*, 12(9):853–855.

[Lantz et al., 1997] Lantz, M. A., O'Shea, S. J., Welland, M. E., and Johnson, K. L. (1997). Atomic-force-microscope study of contact area and friction on NbSe2. *Physical Review B*, 55(16):10776–10785.

[Lee et al., 2002] Lee, S. I., Howell, S. W., Raman, A., and Reifenberger, R. (2002). Nonlinear dynamics of microcantilevers in tapping mode atomic force microscopy: A comparison between theory and experiment. *Physical Review B*, 66:115409.

[Leite and Herrmann, 2005] Leite, F. L. and Herrmann, P. S. P. (2005). Application of atomic force spectroscopy (AFS) to studies of adhesion phenomena: a review. *Journal of Adhesion Science and Technology*, 19(3-5):365–405.

[Lennard-Jones, 1924] Lennard-Jones, J. (1924). On the Determination o f Molecular Fields. *Procedures Royal Society London A*, 4(71).

[Li et al., 2009] Li, J. W., Cleveland, J. P., and Proksch, R. (2009). Bimodal magnetic force microscopy: Separation of short and long range forces. *Applied Physics Letters*, 94(16).

[Lifshitz, 1956] Lifshitz, E. M. (1956). The Theory of Molecular Attractive Forces between Solids. *Soviet Physics*, 2(1):73–83.

[Liu et al., 2010a] Liu, B. G., Thomas, C. S., Craig, G. S. W., and Nealey, P. F. (2010a). Integration of Density Multiplication in the Formation of Device-Oriented Structures by Directed Assembly of Block Copolymer – Homopolymer Blends. *Advanced Functional Materials*, 20:1251–1257.

[Liu et al., 2010b] Liu, J., Grierson, D. S., Moldovan, N., Notbohm, J., Li, S., Jaroenapibal, P., O'Connor, S. D., Sumant, A. V., Neelakantan, N., Carlisle, J. A., Turner, K. T., and Carpick, R. W. (2010b). Preventing nanoscale wear of atomic force microscopy tips through the use of monolithic ultrananocrystalline diamond probes. *Small*, 6(10):1140–1149.

[London, 1937] London, F. (1937). The general theory o f molecular forces. *Trans. Faraday Soc.*, 33(8):8–26.

[López-Guerra and Solares, 2014] López-Guerra, E. A. and Solares, S. D. (2014). Modeling viscoelasticity through spring-dashpot models in intermittent-contact atomic force microscopy. *Beilstein Journal of Nanotechnology*, 5(1):2149–2163.

[Lorenzoni et al., 2017] Lorenzoni, M., Evangelio, L., and Ferna, M. (2017). Sequential In fi ltration of Self-Assembled Block Copolymers : A Study by Atomic Force Microscopy. *Journal of Physical Chemistry C*, 121:3078–3086.

[Lorenzoni et al., 2015a] Lorenzoni, M., Evangelio, L., Nicolet, C., Navarro, C., San Paulo, A., Rius, G., and Pérez-Murano, F. (2015a). Nanomechanical properties of solvent cast polystyrene and poly(methyl methacrylate) polymer blends and self-assembled block copolymers. *Journal of Micro/Nanolithography, MEMS, and MOEMS*, 14(3):033509.

[Lorenzoni et al., 2015b] Lorenzoni, M., Evangelio, L., Verhaeghe, S., Nicolet, C., Navarro, C., Pérez-Murano, F., and Pe, F. (2015b). Assessing the Local Nanomechanical Properties of Self-Assembled Block Copolymer Thin Films by Peak Force Tapping. *Langmuir*, 31(42):11630–11638.

[Lozano and Garcia, 2008] Lozano, J. R. and Garcia, R. (2008). Theory of multifrequency atomic force microscopy. *Physical Review Letters*, 100(7):8–11.

[Maivald et al., 1991] Maivald, P., Butt, H. J., Gould, S. A. C., Prater, C. B., Drake, B., Gurley, J. A., Elings, V. B., and Hansma, P. K. (1991). Using force modulation to image surface elasticities with the atomic force microscope. *Nanotechnology*, 2(2):103–106.

[Mansky et al., 1995] Mansky, P., Chaikin, P., and Thomas, E. L. (1995). Monolayer films of diblock copolymer microdomains for nanolithographic applications. *Journal of Materials Science*, 30:1987–1992.

[Maragliano et al., 2015] Maragliano, C., Glia, A., Stefancich, M., and Chiesa, M. (2015). Effective AFM cantilever tip size: Methods for in-situ determination. *Measurement Science and Technology*, 26(1).

[Martínez et al., 2008] Martínez, N. F., Lozano, J. R., Herruzo, E. T., Garcia, F., Richter, C., Sulzbach, T., and Garcia, R. (2008). Bimodal atomic force microscopy imaging of isolated antibodies in air and liquids. *Nanotechnology*, 19(38).

[Martinez et al., 2006] Martinez, N. F., Patil, S., Lozano, J. R., and Garcia, R. (2006). Enhanced compositional sensitivity in atomic force microscopy by the excitation of the first two flexural modes. *Applied Physics Letters*, 89(15):2–4.

[Maugis, 1992] Maugis, D. (1992). Adhesion of spheres: The JKR-DMT transition using a dugdale model. *Journal of Colloid And Interface Science*, 150(1):243–269.

[McConney et al., 2010] McConney, M. E., Singamaneni, S., and Tsukruk, V. V. (2010). Probing soft matter with the atomic force microscopies: Imaging and force spectroscopy. *Polymer Reviews*, 50(3):235–286.

[McGuiggan and Yarusso, 2004] McGuiggan, P. and Yarusso, D. (2004). Measurement of the loss tangent of a thin polymeric film using the atomic force microscope. *Journal of Materials Research*, 19(01):387–395.

[Meirovitch, 2001] Meirovitch, L. (2001). *Fundamentals of Vibrations*. McGraw-Hill.

[Melcher et al., 2007] Melcher, J., Hu, S., and Raman, A. (2007). Equivalent point-mass models of continuous atomic force microscope probes. *Applied Physics Letters*, 91(5):053101.

[Melcher et al., 2012] Melcher, J., Kiracofe, D., Hu, S., Johnson, S., and Raman, A. (2012). *Virtual Environment For Dynamic AFM - Comprehensive Manual*.

[Menard, 2008] Menard, K. P. (2008). *Dynamic Mechanical Analysis: A practical introduction*. CRC Press.

[Meyer and Amer, 1988] Meyer, G. and Amer, N. M. (1988). Novel optical approach to atomic force microscopy. *Applied Physics Letters*, 53(12):1045–1047.

[Mie, 1903] Mie, G. (1903). Zur kinetischen Theorie der einatomigen K??rper. *Annalen der Physik*, 316(8):657–697.

[Montelius and Tegenfeldt, 1993] Montelius, L. and Tegenfeldt, J. O. (1993). Direct observation of the tip shape in scanning probe microscopy. *Applied Physics Letters*, 62(21):2628–2630.

[Muller et al., 1983] Muller, V. M., Derjaguin, B. V., and Toporov, Y. P. (1983). On two methods of calculation of the force of sticking of an elastic sphere to a rigid plane. *Colloids and Surfaces*, 7(3):251–259.

[Muller et al., 1980] Muller, V. M., Yushchenko, V. S., and Derjaguin, B. V. (1980). On the influence of molecular forces on the deformation of an elastic sphere and its sticking to a rigid plane. *Journal of Colloid and Interface Science*, 77(1):91–101.

[Necas and Klapetek, 2012] Necas, D. and Klapetek, P. (2012). Gwyddion : an open-source software for SPM data analysis. *Central European Journal of Physics*, 10(1):181–188.

[O'Brien and Hermann, 1973] O'Brien, W. J. and Hermann, J. J. (1973). The Strength of Liquid Bridges Between Dissimilar Materials. *The Journal of Adhesion*, 5(2):91–103.

[Odin et al., 1994] Odin, J., Aime, Z. K., and Bouhacina, T. (1994). Tip's finite size effects on atomic force microscopy in the contact mode: simple geometrical consideration for rapid estimation of apex radius and tip angle based on the study of polystyrene latex balls. *Surface Science*, 317(94):321–340.

[Ohler, 2007] Ohler, B. (2007). Practical Advice on the Determination of Cantilever Spring Constants. AN94:1–12.

[Ohler and Kocun, 2013] Ohler, B. and Kocun, M. (2013). Exploring Nanoscale Viscoelastic Properties: Recent Advances in Contact Resonance Imaging with AFM. *GIT Imaging and Microscopy*, 15(November):22–4.

[Oliver and Pharr, 2004] Oliver, W. and Pharr, G. (2004). Measurement of hardness and elastic modulus by instrumented indentation: Advances in understanding and refinements to methodology. *Journal of Materials Research*, 19(01):3–20.

[Oliver and Pharr, 1992] Oliver, W. C. and Pharr, G. M. (1992). An improved technique for determining hardness and elastic modulus using load and displacement sensing indentation experiments. *Journal of Materials Research*, 7(6):1564–1583.

[Otsu, 1979] Otsu, N. (1979). A Threshold Selection Method from Gray-Level Histograms. *IEEE Transactions on Systems, Man, and Cybernetics*, SMC-9(1):62–66.

[Parker and Dick, 2012] Parker, E. R. and Dick, A. J. (2012). Response Measurement Accuracy for Off-Resonance Excitation in Atomic Force Microscopy. *Journal of Dynamic Systems, Measurement, and Control*, 134(1):011010.

[Pashley, 1984] Pashley, M. D. (1984). Further consideration of the DMT model for elastic contact. *Colloids and Surfaces*, 12(C):69–77.

[Passeri et al., 2013] Passeri, D., Rossi, M., Tamburri, E., and Terranova, M. L. (2013). Mechanical characterization of polymeric thin films by atomic force microscopy based techniques. *Analytical and Bioanalytical Chemistry*, 405(5):1463–1478.

[Patil and Dharmadhikari, 2002] Patil, S. and Dharmadhikari, C. V. (2002). Investigation of the electrostatic forces in scanning probe microscopy at low bias voltages. *Surface and Interface Analysis*, 33(2):155–158.

[Patil et al., 2000] Patil, S., Kulkarni, A. V., and Dharmadhikari, C. V. (2000). Study of the electrostatic force between a conducting tip in proximity with a metallic surface: Theory and experiment. *Journal of Applied Physics*, 88(11):6940.

[Payam et al., 2015] Payam, A. F., Martin-jimenez, D., and Garcia, R. (2015). Force reconstruction from tapping mode force microscopy experiments. *Nanotechnology*, 26(18):185706.

[Peng et al., 2010] Peng, B. Q., Tseng, Y., Darling, S. B., and Elam, J. W. (2010). Nanoscopic Patterned Materials with Tunable Dimensions via Atomic Layer Deposition on Block Copolymers. *Advanced Materials*, 22:5129–5133.

[Pharr, 1998] Pharr, G. M. (1998). Measurement of mechanical properties by ultra-low load indentation. *Materials Science and Engineering: A*, 253(1-2):151–159.

[Preiner et al., 2007] Preiner, J., Tang, J., Pastushenko, V., and Hinterdorfer, P. (2007). Higher harmonic atomic force microscopy: Imaging of biological membranes in liquid. *Physical Review Letters*, 99(4):1–4.

[Proksch, 2006] Proksch, R. (2006). Multifrequency, repulsive-mode amplitude-modulated atomic force microscopy. *Applied Physics Letters*, 89(11):129–132.

[Proksch et al., 2004] Proksch, R., Schäffer, T. E., Cleveland, J. P., Callahan, R. C., and Viani, M. B. (2004). Finite optical spot size and position corrections in thermal spring constant calibration. *Nanotechnology*, 15(9):1344–1350.

[Proksch and Yablon, 2012] Proksch, R. and Yablon, D. G. (2012). Loss tangent imaging: Theory and simulations of repulsive-mode tapping atomic force microscopy. *Applied Physics Letters*, 100(7):100–103.

[Rabe and Arnold, 1994] Rabe, U. and Arnold, W. (1994). Acoustic microscopy by atomic force microscopy. *Applied Physics Letters*, 64(12):1493–1495.

[Rabe et al., 1996] Rabe, U., Janser, K., and Arnold, W. (1996). Vibrations of free and surface-coupled atomic force microscope cantilevers: Theory and experiment. *Review of Scientific Instruments*, 67(9):3281–3293.

[Rabe et al., 2002] Rabe, U., Kopycinska, M., Hirsekorn, S., Muñoz-Saldaña, J., Schneider, G. A., and Arnold, W. (2002). High-resolution characterization of piezoelectric ceramics by ultrasonic scanning force microscopy techniques G A Schneider and W Arnold. *Journal of Physics D: Applied Physics*, 35:2621–2635.

[Rabinovich et al., 2000a] Rabinovich, Y. I., Adler, J. J., Ata, A., Singh, R. K., and Moudgil, B. M. (2000a). Adhesion between nanoscale rough surfaces. I. Role of asperity geometry. *Journal of Colloid and Interface Science*, 232(1):10–16.

[Rabinovich et al., 2000b] Rabinovich, Y. I., Adler, J. J., Ata, A., Singh, R. K., and Moudgil, B. M. (2000b). Adhesion between nanoscale rough surfaces: II. Measurement and comparison with theory. *Journal of Colloid and Interface Science*, 232(1):17–24.

[Rabinovich et al., 2002] Rabinovich, Y. I., Adler, J. J., Esayanur, M. S., Ata, A., Singh, R. K., and Moudgil, B. M. (2002). Capillary forces between surfaces with nanoscale roughness. *Advances in Colloid and Interface Science*, 96(1-3):213–230.

[Rabinovich and Yoon, 1994] Rabinovich, Y. I. and Yoon, R. H. (1994). Use of Atomic Force Microscope for the Measurements of Hydrophobic Forces between Silanated Silica Plate and Glass Sphere. *Langmuir*, 10(6):1903–1909.

[Raman et al., 2008] Raman, A., Melcher, J., and Tung, R. (2008). Cantilever dynamics in atomic force microscopy Dynamic atomic force microscopy , in essence , consists of a vibrating. *Review Literature And Arts Of The Americas*, 3(1):20–27.

[Raman et al., 2011] Raman, A., Trigueros, S., Cartagena, A., Stevenson, A. P. Z., Susilo, M., Nauman, E., and Contera, S. A. (2011). Mapping nanomechanical properties of live cells using multi-harmonic atomic force microscopy. *Nature Nanotechnology*, 6(12):809–814.

[Ramos, 2014] Ramos, J. R. (2014). Tip radius preservation for high resolution imaging in amplitude modulation atomic force microscopy. *Applied Physics Letters*, 105(4).

[Rao et al., 1979] Rao, M., Berne, B. J., Percus, J. K., and Kalos, M. H. (1979). Structure of a liquid-vapor interface in the presence of a hard wall in the transition region. *The Journal of Chemical Physics*, 71(9):3802–3806.

[Rathsack et al., 2013] Rathsack, B., Somervell, M., Muramatsu, M., Tanouchi, K., Kitano, T., Nishimura, E., Yatsuda, K., Nagahara, S., Iwaki, H., Akai, K., Ozawa, M., Negreira, A. R., Tahara, S., and Nafus, K. (2013). Advances in Directed Self Assembly Integration and Manufacturability at 300 mm. In *Advances in Resist Materials and Processing Technology*, volume 8682, pages 1–11.

[Rezende et al., 2009] Rezende, C. A., Lee, L.-T., and Galembeck, F. (2009). Surface Mechanical Properties of Thin Polymer Films Investigated by AFM in Pulsed Force Mode. *Langmuir*, 25(17):9938–9946.

[Rimai and DeMejo, 1996] Rimai, D. S. and DeMejo, L. P. (1996). Physical Interactions Affecting the Adhesion of Dry Particles. *Annual Review of Materials Science*, 26(1):21–41.

[Rodriguez and Garcia, 2002] Rodriguez, T. R. and Garcia, R. (2002). Tip motion in amplitude modulation (tapping-mode) atomic-force microscopy: Comparison between continuous and point-mass models. *Applied Physics Letters*, 80(9):1646–1648.

[Rodriguez and Garcia, 2004] Rodriguez, T. R. and Garcia, R. (2004). Compositional mapping of surfaces in atomic force microscopy by excitation of the second normal mode of the microcantilever. *Applied Physics Letters*, 84(3):449–451.

[Rosa-Zeiser et al., 1997] Rosa-Zeiser, A., Weilandt, E., Hild, S., and Marti, O. (1997). The simultaneous measurement of elastic, electrostatic and adhesive properties by scanning force microscopy: pulsed-force mode operation. *Measurement Science and Technology*, 8(11):1333–1338.

[Ruiz et al., 2012] Ruiz, R., Wan, L., Lille, J., Patel, K. C., Dobisz, E., Johnston, D. E., Kisslinger, K., and Black, C. T. (2012). Image quality and pattern transfer in directed self assembly with block-selective atomic layer deposition. *Journal of Vacuum Science & Technology B: Microelectronics and Nanometer Structures*, 30(6):1–6.

[Rumpf, 1990] Rumpf, H. (1990). *Particle Technology*. Chapman and Hall.

[Sader, 1998] Sader, J. E. (1998). Frequency response of cantilever beams immersed in viscous fluids with applications to the atomic force microscope. *Journal of Applied Physics*, 84(1):64–76.

[Sader et al., 2016] Sader, J. E., Borgani, R., Gibson, C. T., Haviland, D. B., Higgins, M. J., Kilpatrick, J. I., Lu, J., Mulvaney, P., Shearer, C. J., Slattery, A. D., Thorén, P. A., Tran, J., Zhang, H., Zhang, H., and Zheng, T. (2016). A virtual instrument to standardise the calibration of atomic force microscope cantilevers. *Review of Scientific Instruments*, 87(9).

[Sader et al., 1999] Sader, J. E., Chon, J. W. M., and Mulvaney, P. (1999). Calibration of rectangular atomic force microscope cantilevers. *Review of Scientific Instruments*, 70(10):3967–3969.

[Sader et al., 2014] Sader, J. E., Lu, J., and Mulvaney, P. (2014). Effect of cantilever geometry on the optical lever sensitivities and thermal noise method of the atomic force microscope. *Review of Scientific Instruments*, 113702:6–11.

[Sader and White, 1993] Sader, J. E. and White, L. (1993). Theoretical analysis of static deflection of plates for atomic force microscope applications. *Journal of Applied Physics*, 74(1):1–9.

[Sahin et al., 2007] Sahin, O., Magonov, S., Su, C., Quate, C. F., and Solgaard, O. (2007). An atomic force microscope tip designed to measure time-varying nanomechanical forces. *Nature Nanotechnology*, 2(8):507–514.

[Sahin et al., 2004a] Sahin, O., Quate, C. F., Solgaard, O., and Atalar, A. (2004a). Resonant harmonic response in tapping-mode atomic force microscopy. *Physical Review B - Condensed Matter and Materials Physics*, 69(16):1–9.

[Sahin et al., 2004b] Sahin, O., Yaralioglu, G., Grow, R., Zappe, S. F., Atalar, A., Quate, C., and Solgaard, O. (2004b). High-resolution imaging of elastic properties using harmonic cantilevers. *Sensors and Actuators, A: Physical*, 114(2-3):183–190.

[San Paulo and Garcia, 2001] San Paulo, A. and Garcia, R. (2001). Tip surface forces, amplitude, and energy dissipation in amplitude modulation (tapping mode) force microscopy. *Physical Review B*, 64(19):193411.

[San Paulo and Garcia, 2002] San Paulo, A. and Garcia, R. (2002). Unifying theory of tapping mode atomic force microscopy. *Physical Review B*, 66(4):041406.

[Santos et al., 2014] Santos, S., Barcons, V., Font, J., and Verdaguer, A. (2014). Unlocking higher harmonics in atomic force microscopy with gentle interactions. *Beilstein Journal of Nanotechnology*, 5(1):268–277.

[Santos et al., 2012] Santos, S., Souier, T., Gadelrab, K., Chiesa, M., and Thomson, N. H. (2012). A method to provide rapid in situ determination of tip radius in dynamic atomic force microscopy. *Review of Scientific Instruments*, 83(2012).

[Sarioglu and Solgaard, 2011] Sarioglu, A. F. and Solgaard, O. (2011). Modeling, design, and analysis of interferometric cantilevers for time-resolved force measurements in tapping-mode atomic force microscopy. *Journal of Applied Physics*, 109(6).

[Schaefer et al., 1995] Schaefer, D. M., Carpenter, M., Gady, B., Reifenberger, R., Demejo, L. P., and Rimai, D. S. (1995). Surface roughness and its influence on particle adhesion using atomic force techniques. *Journal of Adhesion Science and Technology*, 9(8):1049–1062.

[Schaefer et al., 1994] Schaefer, D. M., Carpenter, M., Reifenberger, R., Demejo, L. P., and Rimai, D. S. (1994). Surface force interactions between micrometer-size polystyrene spheres and silicon substrates using atomic force techniques. *Journal of Adhesion Science and Technology*, 8(3):197–210.

[Schäffer, 2005] Schäffer, T. E. (2005). Calculation of thermal noise in an atomic force microscope with a finite optical spot size. *Nanotechnology*, 16(6):664–670.

[Segeren et al., 2002] Segeren, L. H. G. J., Siebum, B., Karssenberg, F. G., Van Den Berg, J. W. A., and Vancso, G. J. (2002). Microparticle adhesion studies by atomic force microscopy. *Journal of Adhesion Science and Technology*, 16(7):793–828.

[Senden and Ducker, 1994] Senden, T. J. and Ducker, W. A. (1994). Experimental Determination of Spring Constants in Atomic Force Microscopy. *Langmuir*, 10(4):1003–1004.

[Seul and Andelman, 1995] Seul, M. and Andelman, D. (1995). Domain shapes and patterns: the phenomenology of modulated phases. *Science*, 267:476–483.

[Shore and Hadfield, 1918] Shore, A. and Hadfield, R. (1918). No Title. *Journal of iron and Steel Institute, London*, 59.

[Sirghi et al., 2000] Sirghi, L., Nakagiri, N., Sugisaki, K., Sugimura, H., and Takai, O. (2000). Effect of sample topography on adhesive force in atomic force spectroscopy measurements in air. *Langmuir*, 16(20):7796–7800.

[Smith and Sandland, 1922] Smith, R. L. and Sandland, G. E. (1922). An Accurate Method of Determining the Hardness of Metals. *Proceedings of the Institution of Mechanical Engineers*, (May):623–641.

[Song et al., 2015] Song, Y., Wu, S., Xu, L., and Fu, X. (2015). Accurate calibration and uncertainty estimation of the normal spring constant of various AFM cantilevers. *Sensors (Switzerland)*, 15(3):5865–5883.

[Stark et al., 2000] Stark, M., Stark, R. W., Heckl, W. M., and Guckenberger, R. (2000). Spectroscopy of the anharmonic cantilever oscillations in tapping-mode atomic-force microscopy. *Applied Physics Letters*, 77(20):3293–3295.

[Stark, 2010] Stark, R. W. (2010). Bistability, higher harmonics, and chaos in AFM. *Materials Today*, 13(9):24–32.

[Stark and Heckl, 2000] Stark, R. W. and Heckl, W. M. (2000). Fourier transformed atomic force microscopy: tapping mode atomic force microscopy beyond the Hookian approximation. *Surface Science*, 457(1-2):219–228.

[Stark and Heckl, 2003] Stark, R. W. and Heckl, W. M. (2003). Higher harmonics imaging in tapping-mode atomic-force microscopy. *Review of Scientific Instruments*, 74(2003):5111–5114.

[Stark et al., 2007] Stark, R. W., Naujoks, N., and Stemmer, A. (2007). Multifrequency electrostatic force microscopy in the repulsive regime. *Nanotechnology*, 18(6).

[Stark et al., 2004] Stark, R. W., Schitter, G., Stark, M., Guckenberger, R., and Stemmer, A. (2004). State-space model of freely vibrating and surface-coupled cantilever dynamics in atomic force microscopy. *Physical Review B*, 69(8):085412.

[Stifter et al., 2000] Stifter, T., Marti, O., and Bhushan, B. (2000). Theoretical investigation of the distance dependence of capillary and van der Waals forces in scanning force microscopy. *Physical Review B*, 62(20):13667–13673.

[Syed Asif et al., 2001] Syed Asif, S. A., Wahl, K. J., Colton, R. J., and Warren, O. L. (2001). Quantitative imaging of nanoscale mechanical properties using hybrid nanoindentation and force modulation. *Journal of Applied Physics*, 90(3):1192–1200.

[Tabor, 1977] Tabor, D. (1977). Surface forces and surface interactions. *Journal of Colloid And Interface Science*, 58(1):2–13.

[Tamayo and Garcia, 1996] Tamayo, J. and Garcia, R. (1996). Deformation, Contact Time, and Phase Contrast in Tapping Mode Scanning Force Microscopy - Langmuir (ACS Publications). *Langmuir*, 7463(13):4430–4435.

[Tortonese, 1997] Tortonese, M. (1997). Cantievers and tips for atomic force microscopy. *IEEE engineering in medicine and biology*, (April):28–33.

[Tung et al., 2008] Tung, R. C., Jana, A., and Raman, A. (2008). Hydrodynamic loading of microcantilevers oscillating near rigid walls. *Journal of Applied Physics*, 104(11):1–9.

[Turner et al., 2009] Turner, R. D., Kirkham, J., Devine, D., and Thomson, N. H. (2009). Second harmonic atomic force microscopy of living Staphylococcus aureus bacteria. *Applied Physics Letters*, 94(4):1–4.

[Vahdat and Carpick, 2013] Vahdat, V. and Carpick, R. W. (2013). Practical Method to Limit Tip-Sample Contact Stress and Prevent Wear in Amplitude Modulation Atomic Force Microscopy. *ACS Nano*, 7:9836–9850.

[Van Der Werf et al., 1994] Van Der Werf, K. O., Putman, C. A. J., De Grooth, B. G., and Greve, J. (1994). Adhesion force imaging in air and liquid by adhesion mode atomic force microscopy. *Applied Physics Letters*, 65(9):1195–1197.

[Vanlandingham et al., 1997] Vanlandingham, M. R., McKnight, S. H., Palmese, G. R., Elings, J. R., Huang, X., Bogetti, T. A., Eduljee, R. F., and Gillespie, J. W. (1997). Nanoscale Indentation of Polymer Systems Using the Atomic Force Microscope. *The Journal of Adhesion*, 64(1-4):31–59.

[Verdaguer et al., 2012] Verdaguer, A., Santos, S., Sauthier, G., Segura, J. J., Chiesa, M., and Fraxedas, J. (2012). Water-mediated height artifacts in dynamic atomic force microscopy. *Physical Chemistry Chemical Physics*, 14(46):16080.

[Verschuur, 1993] Verschuur, G. L. (1993). *Hidden attraction: The mystery and History of Magnetism*. Oxford University Press, 1st edition.

[Vesenka et al., 1993] Vesenka, J., Manne, S., Giberson, R., Marsh, T., and Henderson, E. (1993). Colloidal gold particles as an incompressible atomic force microscope imaging standard for assessing the compressibility of biomolecules. *Biophysical journal*, 65(3):992–997.

[Wei and Zhao, 2004] Wei, Z. and Zhao, Y. P. (2004). Experimental Investigation of the Velocity Effect on Adhesion Forces with an Atomic Force Microscope. *Chinese Physics Letters*, 21(4):616–619.

[Weisenhorn et al., 1993] Weisenhorn, A. L., Khorsandi, M., Kasas, S., Gotzos, V., and Butt, H. J. (1993). Deformation and height anomaly of soft surfaces studied with an AFM. *Nanotechnology*, 4(2):106–113.

[Wright and Solares, 2011] Wright, C. A. and Solares, S. D. (2011). On mapping subangstrom electron clouds with force microscopy. *Nano Letters*, 11(11):5026–5033.

[Xiao and Qian, 2000] Xiao, X. and Qian, L. (2000). Investigation of humidity-dependent capillary force. *Langmuir*, 16(21):8153–8158.

[Yamanaka et al., 1999] Yamanaka, K., Noguchi, A., Tsuji, T., Koike, T., and Goto, T. (1999). Quantitative Material Characterization by Ultrasonic AFM. *Surface and Interface Analysis*, 27(24):600–606.

[Yamanaka et al., 1994] Yamanaka, K., Ogiso, H., and Kolosov, O. (1994). Ultrasonic force microscopy for nanometer resolution subsurface imaging. *Applied Physics Letters*, 64(2):178–180.

[Yan et al., 2016] Yan, Y., Xue, B., Hu, Z., and Zhao, X. (2016). AFM tip characterization by using FFT filtered images of step structures. *Ultramicroscopy*, 160:155–162.

[Young, 1845] Young, T. (1845). *A course of lectures on natural philosophy and the mechanical arts*. Taylor and Walton.

[Young et al., 2011] Young, T. J., Monclus, M. A., Burnett, T. L., Broughton, W. R., Ogin, S. L., and Smith, P. A. (2011). The use of the PeakForceTMquantitative nanomechanical mapping AFM-based method for high-resolution Young's modulus measurement of polymers. *Measurement Science and Technology*, 22(12).

[Zanette et al., 2000] Zanette, S., Caride, A., Nunes, V., Klimchitskaya, G., Freire, F., and Prioli, R. (2000). Theoretical and experimental investigation of the force–distance relation for an atomic force microscope with a pyramidal tip. *Surface Science*, 453(1-3):75–82.

[Zlotnikov et al., 2014] Zlotnikov, I., Fratzl, P., and Zolotoyabko, E. (2014). Nanoscale elastic modulus mapping revisited: The concept of effective mass. *Journal of Applied Physics*, 116(11):114308.

[Zlotnikov et al., 2017] Zlotnikov, I., Zolotoyabko, E., and Fratzl, P. (2017). Nanoscale modulus mapping of biological composite materials: Theory and practice. *Progress in Materials Science*, 87:292–320.

Appendices

Appendix A

Continuous monitoring of tip radius during AFM imaging

J. Fraxedas[a,b], F. Perez-Murano[c], F. Gramazio[a,b], M. Lorenzoni[c], E. Rull Trinidad[d], U. Staufer[d]
a) Institut Catala de Nanociencia i Nanotecnologia (ICN2), Campus UAB, 08193 Bellaterra, Barcelona, Spain; **b**) Consejo Superior de Investigaciones Cientificas (CSIC), Campus UAB, ICN2 Building, 08193 Bellaterra, Barcelona, Spain; **c**) Instituto de Microelectrónica de Barcelona (IMBCNM, CSIC), Campus UAB, 08193 Bellaterra, Barcelona, Spain; **d**) Technical University of Delft, Mekelweg 2, 2628CD Delft, The Netherlands.

Keywords: atomic force microscopy, amplitude modulation, tip monitoring, higher harmonics, computer simulations, polymers

Abstract

We present a continuous tip monitoring method during atomic force microscopy imaging based on the use of higher harmonics, which are generated in the repulsive regime as a result of the nonlinear interactions between the cantilever tip and the surface under study. We have applied this method to commercial rectangular micro-fabricated silicon cantilevers with force constants in the 45 $\mathrm{N\,m^{-1}}$ range and fundamental frequencies in the 300 kHz to 400 kHz range and with tip radii below 10 nm. We have focused in the resonance of the 2^{nd} flexural mode and the 6^{th} harmonic using polystyrene surfaces. The simultaneous acquisition of topographic and higher harmonic images allows a continuous control of the state of the tip. The experimental results have been rationalized with computer simulations taking into account both the cantilever dynamics and the tip-surface interactions. **Keywords**: atomic force microscopy, amplitude modulation, tip monitoring, higher harmonics, computer simulations, polymers

Introduction

The irreversible deterioration of cantilever tips and of the surfaces under characterization during atomic force microscopy (AFM) operation is a concern as old as AFM itself and several strategies have been undertaken since its discovery [Binnig and Quate, 1986] in order to monitor the physical condition of the tip [Carpick and Salmeron, 1997]. The amplitude modulation (AM)-AFM operation mode was implemented with the aim to strongly reduce tip wear through intermittent contact, eliminating shear stresses due to sliding [Garcia, 2002]. However, such reduction is not complete because of the high frequency oscillations involved, within the few hundreds of kHz. Thus, tip wear can still be a drawback even in the less invasive AM-AFM mode. This is an important issue not only for the routinely characterization of surfaces but also for tip-based manufacturing technologies and metrology involving AM-AFM operation since wear must be avoided in order to provide viable processes [Fernandez-Regulez et al., 2014]. A first choice directed towards longer tip lifetimes, and already pointed out for the more stringent contact operation mode, is to use wear-resistant carbon-based (diamond-like) tips [Liu et al., 2010b]. Wear can be modelled as an irreversible thermally activated atom-by-atom mass transfer process from the sample to the tip as a result of adhesive interactions [Bassani and D'Acunto, 2000]. Recently, a methodology has been developed in order to prevent tip wear by the careful selection of the experimental conditions (probe and free oscillation amplitude) prior to AM-AFM experiments [Vahdat and Carpick, 2013]. In this case, stress maps, calculated from the maximum repulsive forces and contact stresses, are used as a guide to select appropriate cantilevers and free oscillation amplitudes (A_0). A second choice consists in the monitoring of the tip state as a function of time. An example of such strategy is given by the in situ characterization of the abrasive wear of sharp silicon tips sliding over polymeric surfaces [Gotsmann and Lantz, 2008]. In this case the value of the tip radius (R) is obtained after taking adhesion curves. Thus, this method has to be considered as quasi-continuous since scanning of the tip on the surface has to be interrupted. Another reported in situ quasi-continuous method allows the determination of R based on the concept that the value of the critical amplitude (A_c) strongly depends on R, closely following a power law ($A_c \propto R_b$). Ac accounts for the free amplitude for which transitions from the attractive to the repulsive force regimes are observed in ambient conditions and the real number b depends on the particular cantilever used [Santos et al., 2012]. To our knowledge, the only reported continuous tip monitoring method has been achieved using contact resonance force microscopy, where the tip is brought into mechanical contact with a surface and either the cantilever or the surface is vibrated over a frequency range that excites a flexural resonance of the cantilever. Due to the tip-sample interactions, the contact resonance will be shifted to higher frequencies compared to the free air resonance so that the contact stiffness (proportional to the contact radius) can be obtained during scanning [Killgore et al., 2011]. Here, we present a new continuous tip monitoring method during AM-AFM imaging based on the use of higher harmonics of the oscillating cantilever [Fraxedas et al.,]. The involved nonlinear tip-sample interaction induces an anharmonic cantilever motion that can be expressed in terms of a Fourier series with An amplitude coefficients and frequencies fn multiples of the fundamental frequency (f_0), $f_n = nf_0$, where n is an integer number $(1, 2, \dots)$ [Stark and Heckl, 2000]. The amplitudes A_n of the higher harmonics can be expressed in terms of the tip-sample interaction [Dürig, 2000], which is a function of both tip and sample parameters, such as R, Young's moduli E, cantilever force constant k_c and quality factor Q. Thus, An can be expressed in terms of such parameters: $A_n(R, E, k_c, Q, \dots)$. In absence of a simplified analytical expression for A_n, numerical simulations are required using tip-surface interactions models such as the Hertz, Derjaguin-Muller-Toporov (DMT), Johnson-Kendall-Roberts (JKR) models and additional approximations, involving different degrees of complexity [Israelachvili, 2011]. Due to the involved low A_n amplitudes (clearly below 1 nm) higher harmonics can be more efficiently observed when they are in resonance with flexural eigenmodes of the cantilever [Sahin et al., 2004a].

Material and methods

AFM experiments have been performed with a Bruker ICON instrument hosted in a homemade controlled humidity environment with Multimode control electronics and using commercial rectangular microfabricated silicon cantilevers (OTESPA-R3) with $k_c \approx 45\,\mathrm{N\,m^{-1}}$ and $300 \leqslant f_0 \leqslant 400 kHz$ with ultrasharp tips ($R < 10nm$). The amplitudes of the higher harmonics were registered using an internal lock-in amplifier. Humidity was kept below 30%. The polystyrene (PS) sample was a standard film purchased from Bruker (PSFILM-12M). The block copolymer film was prepared from poly(styrene-n-methyl methacrylate), also called PS-b-PMMA 50 : 50 , (Mn=78.4 $\mathrm{kg\,mol^{-1}}$, PDI=1.09) obtained from ARKEMA. The PS-b-PMMA powder was dissolved in PGMEA resulting in a 1.5% (w/w) solution. The block copolymer solution was then spin-coated onto the brush layer to obtain a film with a uniform thickness. The brush layer was a thin layer of PS-r-PMMA which presents almost neutral affinity to the PS and PMMA blocks, facilitating that block co-polymer will self-assemble in the form of perpendicular lamella [Lorenzoni et al., 2015a]. Afterwards, the sample was annealed for 10 min at 230 °C in nitrogen, in order to achieve the segregation of the PS and PMMA blocks. Finally, the sample was exposed to oxygen plasma in order to remove PMMA. Simulations have been performed using the Virtual Environment for Dynamic AFM (VEDA) open code [Kiracofe et al., 2012].

Results and discussion

AM-AFM approach curves

We first discuss the case of approach curves in AM mode, where the free amplitude is reduced by the intermittent interaction of the surface with the oscillating tip. Figure A.1 shows both experimental (a-c) and simulated (d-f) AM-AFM approach curves using the VEDA code for $k_c \approx 45\,\mathrm{N\,m^{-1}}$ cantilevers on PS surfaces. From the experimental part we clearly observe that the higher harmonics become excited in the repulsive region, where the phase values lie above the value corresponding to the free oscillation (5° in figure A.1b). Note that in the simulations (see figure A.1e) the repulsive region corresponds to values of the phase below 90°. From figure A.1c it becomes clear that A_6 dominates over the neighbouring harmonics A_5 and A_7, because of its resonance with the second flexural mode. Just remind that for an ideal tipless rectangular cantilever the frequency of the second flexural eigenmode is 6.27 times the fundamental frequency f_0 (also termed as first fundamental eigenmode), which is close to the sixth harmonic with a frequency 6 times f_0. Note the small value of the maximum of A_6, which is around 0.1 nm, approximately an order of magnitude larger than A_5 and A_7. The higher harmonics exhibit a characteristic inverted U-shape, with an initial rapid increase when the repulsive region is reached up to a maximum and then decreasing for decreasing values of the cantilever-sample gap. The simulations (figures A.1d, e and f) closely reproduce the overall shape of the three curves, as well as the resonance. The calculations have been performed using the DMT model with a free oscillation amplitude $A_0 = 35\,\mathrm{nm}$ (as experimentally determined and shown in figure A.1a), the corresponding k_c and f_0 values and with $R = 10\,\mathrm{nm}$ and $E = 3\,\mathrm{GPa}$ for PS. When the maximum of the simulated higher harmonic curves (see figure A.1f) is represented as a function of the tip radius R, we observe that A_6 follows quite closely a power law function, $A_6(R) \approx aR^b$, as depicted from Figure A.2. The simulations have been performed using the following parameters: $A_0 = 44\,\mathrm{nm}$, $k_c = 44\,\mathrm{N\,m^{-1}}$, $Q = 614$, $f_0 = 293\,\mathrm{kHz}$ and $E = 3\,\mathrm{GPa}$. In this case $a = 0.0427\,\mathrm{nm}$ and $b = 0.0774$. Both a and b values depend on the parameters of both the cantilever and of the sample surface. We thus observe that the sixth harmonic follows the same function as the critical amplitude A_c [Santos et al., 2012]. The advantage of using higher harmonics will become evident below since they can be registered continuously. From figure A.2 we can conclude that (i) A_6 increases monotonically with R and (ii) the steeper increase corresponds to the lower values of R. Thus, the sixth harmonic is more sensitive to the initial increase of the tip radius that usually occurs during the acquisition of the fist images.

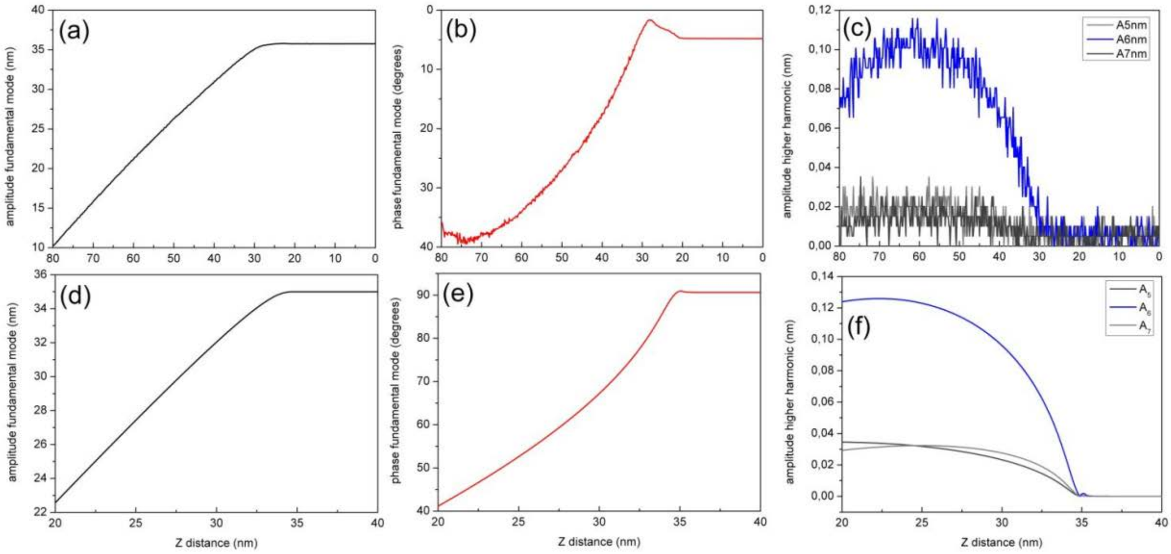

Figure A.1: Experimental (a-c) and simulated (d-f) approach curves performed on a polystyrene surface. Experiments have been performed with a k_c =45 N m^{-1} rectangular AFM cantilever with resonance frequency f_0 =350 kHz and simulations using the VEDA code. Curves (a), (b) and (c) have been obtained simultaneously by approaching the tip towards the surface: (a) and (b) amplitude and phase of the fundamental mode and (c) amplitude of the 5th, 6th and 7th harmonics. Curves (d-f) have been obtained using the DMT model with R =10 nm and E =3 GPa for polystyrene.

AM-AFM imaging

Once we have proven that A_6 increases for increasing values of R, we proceed with the discussion on how can be A_6 determined in a continuous way. For this matter we have explored the evolution of the topography, phase and amplitude images of the 6^{th} harmonic (figure A.3a) of a PS surface as a function of time while keeping both A_0 and amplitude set-point constant. The time evolution of the mean value of A_6 is expressed in terms of the distance travelled by the tip and it is shown in figure A.3b. Since the selected scan width was 1 µm with 256 lines per frame (forward and backward scan directions), each image accounts for 512 µm of tip travelling distance. Each value of the amplitude of the 6^{th} harmonic is obtained from the average of the amplitude values acquired at each point of the image. As it can be observed in figure A.3a, the 6^{th} harmonic amplitude image presents a very uniform aspect. In other experiments, instabilities of the tip apex are directly reflected in the 6^{th} harmonic amplitude image as sudden changes of the registered amplitude value, which can be also used as a method to check tip durability. We observe that after scanning over an accumulated distance of about 10 nm the uncalibrated amplitude of the 6^{th} harmonic monotonically increases from 0.18 mV to 0.37 mV, thus doubling its initial value. This smooth and continuous increase of A_6 can be ascribed to the increase of the tip radius R, following the arguments discussed in figure A.2. Further work is on-going to quantitatively determine the variation of

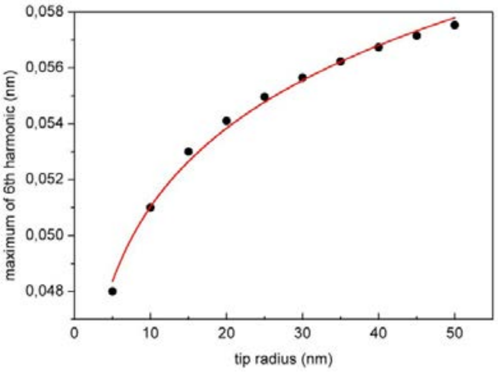

Figure A.2: Simulated evolution of A_6 as a function of R using the VEDA code with the following parameters: A_0 =44 nm, k_c =44 N m^{-1}, f_0 =293 kHz, $Q = 614$ and E =3 GPa for polystyrene and using the DMT tip-surface interaction model. The red curve corresponds to a fit to the aR^b power function with the resulting values: $a = 0.0427$ nm and $b = 0.0774$.

the tip radius from the change in A_6. Such argument is further confirmed by additional experiments performed with nanostructured PS surfaces, obtained from PS-PMMA block-copolymers samples where PMMA has been removed [Fernandez-Regulez et al., 2014, Lorenzoni et al., 2015a]. Block copolymers are of high interest as a method to obtain nanometer scale patterns with 10 nm resolution and below over large areas, surpassing some of the limitations that present lithography techniques are facing [Hinsberg et al., 2010]. Self-assembled layers of thin films of block co-polymers can form perpendicular lamellas, causing a fingerprint-like morphology of the resulting surfaces, as it is shown in figures A.4a and b. These surfaces provide a lateral dimension reference arising from the stripes that help tracking the evolution of R. In this case, the distance between adjacent stripes is about 41 nm. From figure A.4c we again observe that the mean value of A_6, as determined from the amplitude images, increases as a function of the accumulated distance travelled by the tip. In parallel, the contrast of the topography images becomes lower for successive acquired images, as the tip cannot follow the narrow depression corresponding to the area where the PMMA block has been removed. This is better quantified with the help of figure A.4d. In the figure the cross sections for both the first and last acquired topography images are represented. The blue curve, corresponding to the first image, exhibits larger peak-to-valley values as compared to the red curve, which stands for the last measured image. The reduction in contrast is a clear indication that the tip apex deteriorates (enlarges) with time.

Conclusions

In summary, we have observed both experimentally and by means of simulations that the amplitude of the 6^{th} harmonic (A_6) increases for increasing R values following a power law function and that this increase becomes more patent for smaller

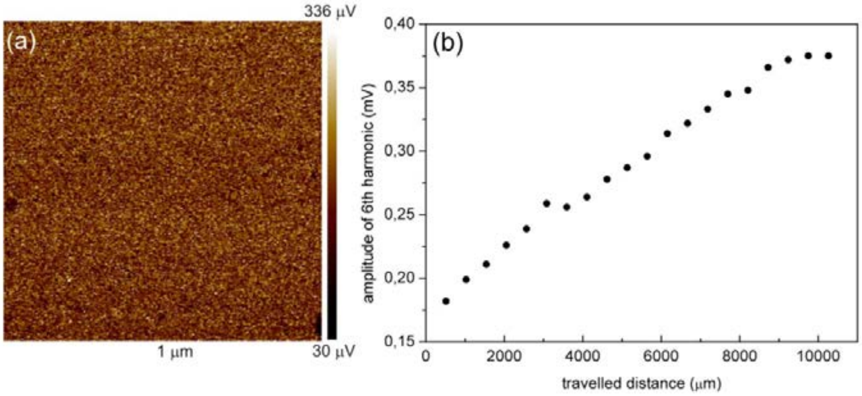

Figure A.3: (a) Amplitude image of the 6^{th} harmonic simultaneously acquired with both the topography and phase images (not show). (b) Evolution of the mean value of the amplitude of the 6^{th} harmonic extracted from the amplitude image (a). Experiments have been performed with a $kc \approx 45N/m$ rectangular AFM cantilever on a polystyrene surface under ambient conditions. The time evolution is expressed in terms of the distance travelled by the tip. The free oscillation amplitude and amplitude setpoint have been kept constant during the experiments.

tip radii (below 20 nm). This allows the simultaneous acquisition of topographic and higher harmonic images thus continuously controlling the state of the tip.

Acknowledgements

This project is supported by the EC through a grant with contract Nr. 309558 within the 7th Framework Program NMP Call 2012.1.4-3 on Nanoscale mechanical metrology for industrial processes and products. ICN2 acknowledges support of the Spanish MINECO through the Severo Ochoa Centers of Excellence Program under Grant SEV-2013-0295. IMBCNM, CSIC acknowledges the grant CSD2010-00024. Thanks are due to Laura Evangelio for the fabrication of the block co-polymer samples.

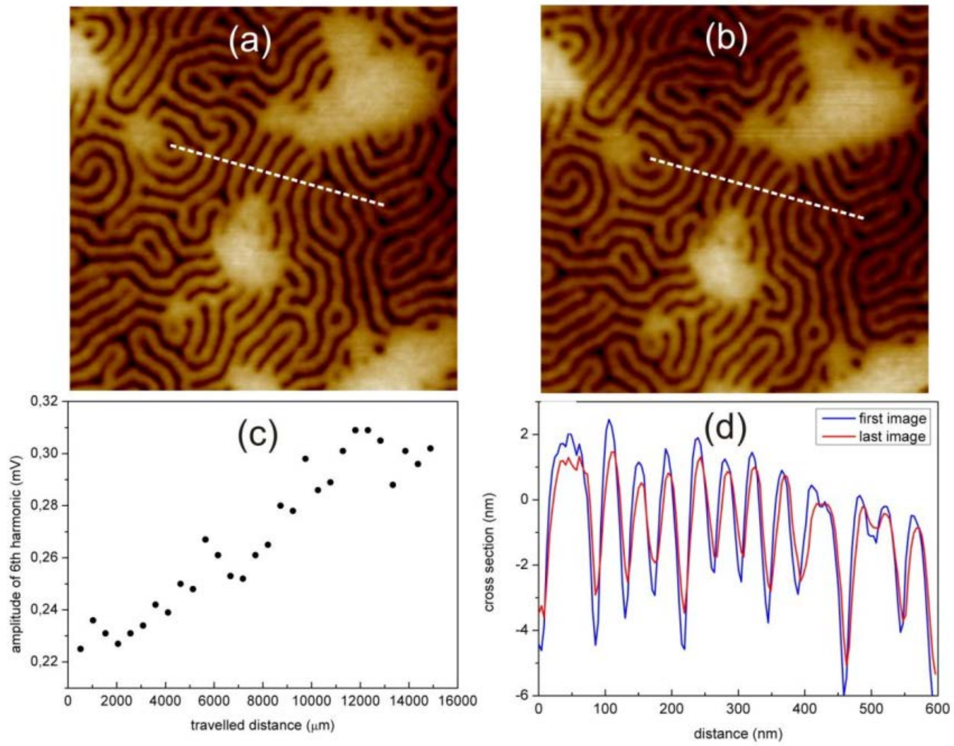

Figure A.4: Topography images of PS-PMMA block copolymer surfaces after removal of PMMA. Scan width is 1 μm. Images were taken at the beginning of the experiment (a) and after 29 images (b). (c) Evolution of the mean value of the amplitude of the 6^{th} harmonic as a function of the distance travelled by the tip. (d) Cross section corresponding to images (a), in blue color, and (b), in red color. The selected line is shown both in (a) and (b) as a discontinuous line.

Appendix B

List of publications

List of publications relevant for this Thesis:

- Fraxedas J, Pérez-Murano F, Gramazio F, Lorenzoni M, Rull Trinidad E, Staufer U. Continuous monitoring of tip radius during atomic force microscopy imaging. Scanning Microscopies. 2015. p. 96360O–1. doi=10.1117/12.2196951
- Gramazio F, Lorenzoni M, Pérez-Murano F, Rull Trinidad E, Staufer U, Fraxedas J. Functional dependence of resonant harmonics on nanomechanical parameters in dynamic mode atomic force microscopy. Beilstein J Nanotechnol. 2017;8:883–91. (Open Access)
- Gramazio F, Lorenzoni M, Pérez-Murano F, Evangelio L, Fraxedas J. Quantification of nanomechanical properties of surfaces by higher harmonic monitoring in amplitude modulated AFM imaging. Ultramicroscopy. Elsevier B.V.; 2018;187:20–5.

Additional publications:

- Lorenzoni M, Llobet J, Gramazio F, Sansa M, Fraxedas J, Perez-murano F. Evaluating the compressive stress generated during fabrication of Si doubly clamped nanobeams with AFM. J Vac Sci Technol B. 2016;34(6):1–6.
- Evangelio L, Gramazio F, Lorenzoni M, Gorgoi M, Espinosa FM, García R, et al. Identifying the nature of surface chemical modification for directed self-assembly of block copolymers. Beilstein J Nanotechnol. 2017;8:1972–81. (Open Access)